University of Alberta

Modeling, Control and Fault Detection of Solid Oxide Fuel Cell System

by

AKM Monjur Murshed 

A thesis submitted to the Faculty of Graduate Studies and Research in partial fulfillment of the requirements for the degree of **Doctor of Philosophy**

in

Process Control

Department of Chemical and Materials Engineering

Edmonton, Alberta
Fall 2007

Your file Votre référence
ISBN: 978-0-494-33034-0
Our file Notre référence
ISBN: 978-0-494-33034-0

...to my family

Abstract

System modeling, controller design and process monitoring are three integral parts of the advanced process control strategies, which are intricately dependent on each other. From the view point of process control, the models should be easy to use for designing controller and yet be detailed enough for giving a true account of the system dynamics.

In this work, two types of models, named lumped and detailed, have been developed for a planar solid oxide fuel cell. The models take electrochemical and thermal aspects into account and provide a set of first-order nonlinear ordinary differential equations. In the lumped model, a uniform temperature throughout fuel cell is assumed whereas in the detailed model uniform temperature distribution is assumed only within each components of the fuel cell. Zero-dimensional thermal models of fuel cell system component such as heat exchangers, reformer and burner are also provided for fuel cell system simulation. The advantage of using capacitor in parallel to the fuel cell is discussed along with the necessary formulation of the equations.

With the advent of cheap computational power, a surge of application of previously non-implementable complex controllers such as nonlinear model predictive controller (NMPC) has been seen in the industries. In this work, NMPC has been applied on the fuel cell system to compare its performance with various linear and nonlinear controllers.

There are numerous fault detection and isolation techniques in the academics works. Of them, principal component analysis (PCA) is widely used for fault detection of linear, steady-state systems. The disadvantage of PCA is that it can not incorporate

process knowledge. Thus, an algorithm for hybrid PCA is provided which can take constraints into consideration by presenting PCA as a linear matrix inequality.

Acknowledgements

I would like to express my gratitude to all those whose help made this thesis possible.

First, I would like to thank my supervisors Dr. Kumar Nandakumar and Dr. Biao Huang. Dr. Nandakumar's ability to pass enthusiasm and encouragement have been of great value to me. His guidance, logical way of thinking, and effort to explain complex things clearly have made it possible to finish this thesis. I could not have thought of having a better supervisor and mentor than him.

I would like to extend my gratitude to Dr. Biao Huang for his supervision, sound advice and innovative ideas. His perceptiveness, patience and constructive comments have been the most valuable asset to me. I would have been lost without him.

I am indebted to my many student colleagues for extending their helpful hands during my course and research work. I am especially grateful to Dr. M.A.A. Shoukat Chowdhury, Dr. Salim Ahmed, Dr. Syed Imtiaz Ahmed, Dr. Liqian Zhang, Rumana Sharmin, Prodip Kumar Das, Fangwei Xu, Yotong Qi, Dr. Vinay Kariwala and Doyadeep Monder Misha. A special thanks belongs to computer support group in the Department of Chemical Engineering, especially to Bob Barton.

Finally, I would like to give my thanks to my wife Sharmeen Akhter whose patient love and encouragement enabled me to complete this work. I also wish to thank my sisters and my parents Md. Enamul Haque and Mrs. Asma Haque for their inspiration and motivation throughout my life. And last but not least to Moumita, for bringing immense joy during the course of writing this thesis.

Contents

List of Tables

List of Figures

List of Symbols

Roman Symbols

A_c	Electrochemical surface area [m^2]
A_r	Reformer reaction area [m^2]
A_{hx}, A_{cx}	Hot and cold flow cross-sectional area [m^2]
C_{cap}	Capacitance [Farad]
C_p	Specific heat [J/Kg.K]
C_{ph}, C_{pc}	Specific heat of hot and cold fluid [J/Kg.K]
$\bar{C}_P$	Average specific heat [J/Kg.K]
d	Diameter of convective loop reactor tube [m]
D_0	Outer diameter [m]
ΔE	Electrode potential difference [volt]
ΔE_0	Standard electrode potential [volt]
f_w	Friction factor at the wall
F	Faraday's constant [96485.34 s.A/mol]
g	Acceleration due to gravity [m^2/s]
h	Heat transfer coefficient [J/m^2]
h_w, h_{w0}	Heat transfer coefficient at the wall and its reference value
$\mathcal{H}_0$, $\mathcal{H}_1$	Fault-free and faulty hypothesis
$\Delta\hat{H}_r^\circ$	Heat of reaction at STP [J/mol]
$\mathbf{I}$	Identity matrix
I	Current [amp]
I_d	Demand current [amp]
I_{fc}, I_{uc}	Current through fuel cell and capacitor [amp]
I_L	Limiting current [amp]
J	Objective function
K_{H_2}, K_{O_2}, K_{H_2O}	Valve molar constant of hydrogen, oxygen and steam
K_S	Equilibrium constant of water-gas shift reaction
l	Length of convective loop reactor [m]
m	mass [kg]
M	Control horizon
$\dot{n}$	Molar flow rate [mol/s]
N	Prediction horizon
N_0	Total number of cell in a stack
$\mathcal{N}$	Normality

p_{H_2}, p_{O_2}, p_{H_2O}	Partial pressures of hydrogen, oxygen and steam [atm]
P	Pressure [atm]
P_{xx}	Covariance of the variable, x
P_{xy}	Covariance of x and y
q_{H_2}, q_{O_2}, q_{H_2O}	Flow rates of hydrogen, oxygen and steam [mol/s]
Q	Heat transfer rate [J/s]
Q_{SPE}	Squared prediction error, or Q-statistics
Q_α	Limit of SPE
r	Resistance [Ohm]
R	Universal gas constant [1 atm/kmol.K]
T	Temperature [K]
T_h, T_c	Temperature of hot and cold fluid [K]
U	Velocity [m/s]
U_0	Overall heat transfer coefficient [J/m^2]
U_f	Fuel utilization
v_h, v_c	Velocity of hot and cold fluid [m/s]
V	Volume [m^3]
$V(x)$	Energy function in terms of the variable x
V_S	Stack voltage [volt]
$\dot{W}$	Shaft work [volt.amp]
W_i	Weight of sigma points, $mathcalX_i$
Δw	Thickness [m]
$\bar{x}$	Mean of variable, x
$\hat{x}$	Predicted value of, x
x^a	Augmented vector (or, matrix) of x
$\mathcal{X}_i$	Sigma points
$\mathcal{Y}_i$	Transformed sigma points
$\mathcal{Z}$	Measurement
Δz	Length of each node [m]

Greek Symbols

α	Parameter of convective loop reactor; Equivalent to Prandtl number
β	Paremeter of convective loop reactor; Equivalent to heating rate
χ^2_p	Chi-square distribution of p degrees of freedom
$\underline{\epsilon}$	Residual
ϵ_a, ϵ_c, ϵ_i	Emissivity constants of anode, cathode and interconnector materials
η_{ohm}, η_{act}, η_{con}	Ohmic, activation and concentration polarization [volt]
γ	Coefficient of thermal expansion
κ	Tuning parameter of UKF

λ	Heat conductivity [J/m.s]
ρ	Density [kg/m^3]
ρ_0	Reference density [kg/m^3]
ρ_h, ρ_c	Density of hot and cold fluid [kg/m^3]
σ	Boltzman constant [5.6704×10^{-8} W/m^2.K^4
Σ_e	Covariance matrix of e
ξ	Extent of reaction [mol/s]

Subscripts

an	Anode
A	Air
B	Burner
d	Diffusion
e	Electrode
F	Fuel
h	Convection
i	Interconnector
r	Radiation
R	Reformer
s	Stack

Superscripts

r	Reactive
in	Inlet condition
out	Outlet condition

Abbreviations

BOP	Balance OF Plant
CFD	Computational Fluid Dynamics
DAE	Differential Algebraic Equation
EKF	Extended Kalman Filter
FDI	Fault Detection and Identification
HPCA	Hybrid PCA
LMPC	Linear Model Predictive Control
LMI	Linear Matrix Inequality
MPC	Model Predictive Control

NMPC	Nonlinear Model Predictive Control
NOx	Oxides of Nitrogen
ODE	Ordinary Differential Equation
OPC	OLE for Process Control
PCA	Principal Component Analysis
PCU	Power Conditioning Unit
PDE	Partial Differential Equation
PID	Proportional Integral Derivative (control)
SOFC	Solid Oxide Fuel Cell
SPE	Squared Prediction Error
SOx	Oxides of Sulphur
UKF	Unscented Kalman Filter
YSZ	Yittria (Y_2O_3) Stabilized Zirconium (ZrO_2)

Chapter 1

Introduction

Fuel cells are electrochemical devices that directly convert chemical energy to electrical energy. Since it does not involve any rotary or, heat engine, it is not associated with any system loss nor is it limited by Carnot cycle efficiency. Moreover, the unreacted fuel from the cell can be used to generate more power. heat can also be recovered from the exhaust gas which increases the overall efficiency of the fuel cell.

Today's energy hungry civilization is in search of an alternative source to replace the currently available but continuously depleting energy sources. Stringent environmental regulations restricting emission of green house gases, SOx, and NOx have narrowed down the search for a clean source of energy to a few options. It has generated a lot of attention towards the fuel cell as an alternative source of clean energy.

However, there are a number of obstacles in the commercialization of fuel cell as a main source of energy. The main obstacle comes from the high manufacturing cost of the fuel cell. A vast amount of research is going on the economic design and operation of fuel cell for reducing the cost and for making it a viable option as an energy source. Selection of materials, which include choice of electrolyte and catalysts as well as electrodes, also contribute to the cost of the fuel cell. A number of researchers have focused on this area. It is often required to simulate the fuel cell system under different operating conditions to account for all the pitfalls associated with the design and material selections. Depending on the perspective, the modeling and simulation can range from micro- to system level. This work focuses on solid

oxide fuel cell system from the perspective of process control for the safe operation of the fuel cell system as a power source. It includes control relevant modeling, controller design and development of fault detection technique.

1.1 Overview of Fuel Cell Technology

Construction of a unit fuel cell mainly consists of three main parts - electrolyte, cathode and anode. Fuel is continuously fed into the anode of the fuel cell, and a suitable oxidant, usually air, is fed into the cathode. The main purpose of the electrolyte is to prevent direct contact of fuel and oxidant such that no combustion takes place. Rather it allows passing oxidant or, reductant to the other side to take part in the electrochemical reaction.

1.1.1 Types of Fuel Cells

Major classifications of types of fuel cells are made based on the choice of electrolyte and fuel:

- **Solid Oxide Fuel Cell (SOFC):** Sold oxide fuel cell uses a solid ceramic type oxide, and thus receives the name. Y_2O_3 stabilized ZO_2 (YSZ) is a common electrolyte used in SOFC. The operating temperature of the fuel cell is usually high (600-1000° C). Due to the solid nature of the electrolyte and electrodes, the SOFC can be designed in the most versatile ways including planar and tubular design.
- **Molten Carbonate Fuel Cell (MCFC):** Molten carbonate fuel cell uses different combinations of alkali carbonates as an electrolyte. These carbonates are usually contained in a ceramic matrix. The operating temperature of MCFC is also high, usually between 600-700° C.
- **Polymer Electrolyte Fuel Cell (PEMFC):** In this type of fuel cell, an polymeric ion exchange membrane is used as an electrolyte. The operating temperature of this fuel cell is usually low (40-80°).

- **Phosphoric Acid Fuel Cell (PAFC):** The electrolyte in the PAFC is 100% phosphoric acid, which is held in a silicon carbide structure. The operating temperature of the fuel cell is about 150 to 220° C, which is one of the attractive features of PAFC. This operating temperature makes it flexible to design the fuel cell and BOP.

In addition, there are Alkaline Fuel Cell (AFC), Direct Methanol Fuel Cell (DMFC), regenerative fuel cell (RFC) and metal air fuel cell (MAFC). Table 1-1 of Fuel Cell Handbook, Edition 7 [134] provides a summary of major differences of different types of fuel cells.

Unit fuel cells are usually stack together to produce the desired output. Depending on the construction of the stack, fuel cells are further classified into planar, tubular and, radial fuel cells. In the planar fuel cell arrangement, unit fuel cells are stacked together connected by interconnectors. The cells are usually connected in series. Several such stacks can also be connected in parallel to make a series-parallel configuration. Depending on the arrangement of the fuel flow, the planar fuel cell structure can further be classified into co-current, counter-current or, cross-flow.

For a hydrogen operated fuel cell, the hydrogen can be produced from natural gas by reforming reaction. For low temperature fuel cells, the reforming reaction is performed external to the fuel cell. For a high temperature fuel cell such as solid oxide fuel cell, the reforming reaction can be performed internal to the fuel cell. Based on the type of heat transfer associated with the reforming reaction, the fuel cell can further be classified into direct-reforming or indirect-reforming fuel cells.

1.1.2 Fuel Cell Systems

In an ideal fuel cell, hydrogen is used as a fuel along with air as an oxidant. Such a fuel cell can work as the cleanest possible source of energy - the byproduct of the reaction being water. But, in reality, even for an ideal fuel cell, there is always some unreacted fuel that needs to be processed. For practical case, hydrogen rich fuels are used to produce hydrogen either internal or external to the fuel cell itself. Thus a

fuel cell plant usually involves components for pre- and post-processing the reactants and products. The components, which are also called balance of plant (BOP), may include compressors, turbine, heat exchanger, reformer, DC-AC converter or, inverter to connect the fuel cell to existing power grid.

Compressors or blowers are required to build necessary pressure to pass reactants and products through different components. On the other hand, the unreacted fuel from the fuel cell itself can be combusted in a gas turbine followed by a steam turbine for generating more power. The compressor-turbine duo thus provides a net power in addition to the direct power by fuel cell itself. In home application, the hot effluent gas can be used as a source for hot water and heating houses.

Fuel cell directly converts chemical energy to electric energy. The output being a DC voltage is appropriate to operate small equipment. For a fuel cell power plant, the DC power however needs to convert to AC power and connect power supply grid. Thus the balance of plant may also include power conditioning unit (PCU).

1.1.3 Advantages and Disadvantages of Fuel Cells

Fuel cell has various advantages over conventional power sources such as batteries, and turbines. As with any technology, fuel cell comes with some disadvantages too including high cost. Some of these are described below.

Advantages:

- It does not have any moving components like turbine, and thus does not have any system loss associated with it. It also provides a quiet operation and less maintenance.
- Unlike heat engine, a fuel cell converts chemical energy directly into electrical energy. Thus, it is not limited by Carnot cycle efficiency.
- The exhaust (unreacted fuel) gas from the fuel cell can be utilized to generate even more power, increasing the efficiency even higher.

- The efficiency of fuel cell is not limited by size. Thus, a small fuel cell powering a laptop or, a personal electronic gadget can generate power at the same efficiency as a 10 MW fuel cell power plant.
- A wide range of fuels can be used for fuel cell.
- Since the reaction inside a fuel cell occurs between specific ions only, it limits release of NOx and SOx to the environment.

Disadvantages:

- Fuel cells are expensive compared to other energy sources.
- Most fuel cells use hydrogen as fuel, which works as a bottleneck due to the associated cost and inconvenience associated with the production, storage and transportation of hydrogen.
- Lower power densities and lifetime.

1.2 Motivation

Identification of process models, design of controller and monitoring of the processes for possible faulty situations are part of the advanced process control strategies. They are intricately dependent on each other. For example, identification of model whether it be first-principle model or data-based, linear or nonlinear, 0-D or 3-D model affects the design of the controller and, fault detection and isolation techniques. Thus, modeling of process should always be based on the objective. A simple control relevant model may perform better than a complex 3-D model, which on the other hand, may be suitable for design and performance analysis of the process. In simple words, the modeling objective can be state as:

Find a model that is suitable for controller design

Similarly, controller design and fault detection techniques should be object oriented. A process expressed by a very complex model can be stable enough to be controlled

by regular PID controller. On the other hand, a simple process may have a lot of environmental and economic constraints requiring multivariate controller to maintain the optimal performance of the system. Same is true for fault detection and isolation techniques.

A solid oxide fuel cell system which exhibits highly nonlinear characteristics, needs to be simulated for different operating conditions. This thesis thus covers all these three inter-related aspects *i.e.*, modeling, control and fault detection of advanced process control applied on the fuel cell system

1.3 Methodology

Recent advances and growing interest in fuel cells have led to a lot of activities on the modeling of fuel cell and its components. Most of these models range from zero dimensional to complex three-dimensional models and also cover the area of performance evaluation and optimal design of the fuel cell. However little work has been done on control relevant models that sufficiently describe the fuel cell system dynamics. This motivated us for developing lumped models of fuel cell and balance of plant. Since the different components inside the fuel cell have different temperature distributions, another more detailed model of fuel cell has been developed which is still suitable for designing controllers.

In process control world, a wide range of linear and nonlinear control techniques have been developed and implemented in the industries. Especially during the past decade, with the advent of cheap computational power, a trend of shifting from traditional PID controller to previously non-implementable controllers, such as nonlinear model predictive controller (NMPC), is being observed. This motivated us to implement nonlinear model predictive control to solid oxide fuel cell system to compare its performance with linear MPC. In this work, nonlinear MPC has been selected due to the highly nonlinear nature of fuel cell system. NMPC is also advantageous over other linear and nonlinear controllers due to its multivariate nature as well as the ability to handle a wide range of constraints. Application of nonlinear model predictive control

requires discretization of the continuous time model as well as estimation of unmeasured states. In this work, this discretization has been performed by using orthogonal collocation method. On the other hand, unscented Kalman filter has been used to estimate unmeasured states from the input-output data.

Before applying nonlinear MPC on solid oxide fuel cell, its performance has been compared with different linear and nonlinear controllers by applying it on a convective loop reactor. Convective loop reactor shows either stable or chaotic behavior based on the heating rate to the system. Normally the reactor has one equilibrium point at low heating rate. The system stabilizes to this equilibrium point quickly after going through turbulence. However as the heating rate is increased, the vertical and horizontal temperature difference of the reactor as well as the average flow rate of fluid through the reactor starts to oscillate. When the heating rate passes certain critical value, the system possesses two unstable equilibrium points instead of one stable equilibrium point and the system variables frequently jump from one equilibrium point to another without any external excitation. No matter how complex the nature of the convective loop might be, it can easily be controlled with controllers, as simple as, on-off controller to stabilize the system to either of the equilibrium points. In this work, model-based nonlinear controllers such as controllers based on Lyaponov stability criterion and back stepping method have been developed. The performances of these controllers are then compared with linear and nonlinear MPC to mitigate the chaotic behavior of the reactor. In all cases, nonlinear MPC outperforms other controllers.

The fuel cell directly converts chemical energy into electrical energy and thus shows size independent high efficiency and noise free operation. However, the unreacted fuel can be utilized to generate more energy, increasing the overall fuel cell system efficiency even higher. The production of this indirect energy comes with some inherent disadvantages of typical power generation system. Thus it is more useful and lucrative to operate the fuel cell system such that direct energy is maximized. In other words, the energy content of the exhaust that is utilized for further power generation should be minimal. A steady-state optimization technique is thus devised for the fuel cell system such that the energy carried over by the exhaust is minimal.

The respective optimal fuel flow rates then used as a reference input in the nonlinear model predictive control to stabilize the system.

During the period of study, one objective has been to develop a fault detection application that can be used to detect fault in processes in real time. The main objective of the application is to predict possible clogging situations in the pipelines carrying slurry such that necessary corrective measures can be taken to avoid the faulty situation. The development of the application includes building the interface using Visual Basic, MATLAB and OPC based on traditional PCA algorithm. Like any other statistical fault detection techniques, traditional PCA can not incorporate constraints based on valuable process information. This led us to develop a hybrid-PCA formulation that can incorporate constraints to the traditional PCA. In this formulation, PCA is represented as a linear matrix inequality. This hybrid-PCA is also applied to the monitoring of fuel cells.

1.4 Thesis Outline

The thesis is organized as follows:

Chapter 2 gives a brief review of published papers on fuel cell modeling and control. Review of different linear and nonlinear controllers, state estimation and fault detection techniques are provided in this chapter.

In chapter 3, two types of control relevant models of a planar solid oxide fuel cell are developed along with the balance of plant. Advantages of using capacitor in parallel with the fuel cell, along with necessary formulation, are also discussed in this chapter. The models are validated by both steady state and dynamic simulations. This work has been published in (Murshed et al. [100]).

Chapter 4 provides a brief review of linear and nonlinear model predictive control. The necessary steps such as discretizing continuous models to a set of discrete algebraic equations by using the orthogonal collocation method and unmeasured state estimation by using unscented Kalman filter are also described in sufficient details in

this chapter. This chapter gives a framework for designing nonlinear model predictive control which is compared with other controllers in chapter 5 and finally applied on solid oxide fuel cell system in chapter 6.

In chapter 5, the performance of nonlinear model predictive control is compared with other linear and nonlinear controllers by applying them on a convective loop reactor. The linear controllers include traditional PID and linear MPC, whereas nonlinear controllers include nonlinear model-based controller based on Lyaponov stability criterion and back stepping method. This work has been published in (Murshed et al. [99]).

Chapter 6 focuses mainly on controlling SOFC and SOFC system by using linear and nonlinear MPC. Necessary formulation for running the SOFC system to produce minimal indirect energy at steady state is also discussed in this chapter. The effect of capacitor on control actions is shown.

A novel formulation of hybrid-PCA is presented in chapter 7. The proposed framework is compared with the traditional PCA for monitoring faulty situations in solid oxide fuel cell system.

Chapter 2

Literature Review

The early history of fuel cell can be traced back to Sir William Robert Grove (1811-1896) who concluded that opposite of electrolysis reaction should be capable of producing electricity. Based on this idea, he constructed a gas cell in 1839 that produces electricity from hydrogen and oxygen. This was the first fuel cell. In 1959, Francis Bacon constructed a working alkaline fuel cell. From that point, research on different kinds of fuel cell has taken a tremendous leap. The following sections are intended to provide a brief review of fuel cell research from the perspective of process control. A brief review on nonlinear model predictive control and principle component analysis has also been provided here.

2.1 Modeling of Solid Oxide Fuel Cell

A large amount of work has been conducted on the modeling of solid oxide fuel cell from the viewpoint of fuel cell design, operability and performance, material selection, and controller design (Damm and Fedorov [31], Hernandez-Pacheco et al. [58], Leah et al. [79], P. et al. [107], Selimovic et al. [123], Stiller et al. [130]). Several authors have investigated performance of solid oxide fuel cell under different operating conditions and design parameters (Hagen et al. [50], Mandin et al. [93]). For example, Koch et al. [74] studied the performance and degradation of a solid oxide fuel cell under severe operating conditions. Stambouli and Traversa [128] discussed the existing and emerging fuel cells technologies in terms of design and operation of SOFC.

The restrictions based on materials requirement and fuel specifications due to high operating temperature along with advantages over other fuel cell technologies have also been addressed in this paper.

Based on the objective, the models can be developed to simulate steady state or dynamic behavior and can range from zero to 3-dimensional (Bove et al. [15, 16]). For example, Padulles et al. [108] developed a simple model of a fuel cell-based power plant which included species dynamics but no temperature dynamics whereas, Hall and Colclaser [51] developed a more detailed model for simulating the transient operation of a tubular solid oxide fuel cell that included electrochemical, thermal and mass flow elements. The latter paper mainly focused on the effect of load change on the terminal voltage. These simple models can be useful for designing controllers and fault detection monitors.

Hanke et al. [52] developed a more complex hierarchical modeling technique that can be used for design and simulation of fuel cell system. Using network theory for chemical engineers, the authors provided a modular model for proton exchange membrane fuel cell system operated with hydrogen and oxygen.

Recently a number of articles have been published in CFD modeling of fuel cell. In CFD modeling techniques, a set of partial differential equations that describe fluid flow, heat transfer, mass transfer, chemical and electro-chemical reactions in fuel cell, are solved numerically by using commercially available packages such as FLUENT, FIDAP, CFX and FEMLAB. The works presented in (Achenbach [4], Besset et al. [12], Bove et al. [16], Braun [19], Iora et al. [62], Leah et al. [79]) investigated transient behavior of a planer SOFC due to load change using multi-dimensional, time dependent models, which are useful for simulating fuel cell behavior. Campanari and Iora [22] provided a finite volume model of a planar solid oxide fuel cell. The authors considered both isothermal and temperature dynamics with refined nodes, as well as different flow geometries (co-, counter- and cross-flow). A comparison of both coarse and refined models has been provided at the end of the work. The models are expressed by a set of PDEs, which are solved numerically to evaluate the performance of the fuel cell based on different design parameters. These models, since expressed as

PDEs, are however not convenient for designing controllers. A brief review of different CFD models can be found in (Ma et al. [90]).

Sedghisigarchi and Feliachi [122] considered chemical and thermal aspects of chemical reactions and ohmic, activation and concentration losses in the fuel cell stack. The authors however only considered lumped thermal models, which is a drawback particularly for a hybrid fuel cell system in conjugation with combustor, turbine and heat exchangers for generating electricity where different flow streams have different temperature distributions. Several authors also developed model of fuel cell system for analyzing fuel cell performance (Chan and Ding [24], Chan et al. [25], Jahn and Schroer [66], Magistri et al. [92]). Table 2.1 of (Braun [19]) summarizes the chronological progression of planar SOFC modeling in terms of the underlying objectives.

Review of mathematical models and design of polymeric membrane electrolyte fuel cells direct methanol fuel cells can be found in (Deluca and Elabd [33], Liu et al. [87], Nguyen and Chan [101], Yao et al. [146]). A review on the design of PEMFC, material selection and mathematical models can be found on (Bıyıkoğlu [14], Cheddie and Munroe [26], Hermann et al. [57], Mehta and Cooper [96], Smitha et al. [127], Tawfik et al. [131]).

2.2 Control of Solid Oxide Fuel Cell

A large amount of work has been conducted on the modeling of solid oxide fuel cell. A few studies on the control of fuel cell systems have also been published. Most of these papers deal with load following performance of different types of fuel cells including PEMFC, MCFC and SOFC by employing localized or, multi-loop controller. Even fewer papers considered controlling the entire fuel cell system by utilizing the constraints handling power of model predictive control.

For example, El-Sarkh et al. [40] designed neural networks-based controller for PEM fuel cell whereas Li et al. [85] developed multi-loop control strategies for maintaining fuel utilization and voltage. Some papers discussed controlling the electrical power of fuel cell connected in the power grid rather than considering the fuel cell system as

a separate process. Zhu and Tomsovic [148] have studied the load following performance of fuel cell and micro-turbine connected in power grid. Ro and Rahman [119] presented methodology for dampening power oscillation of fuel cell devices connected in the electrical distribution network.

Golbert and Lewin [47] used model predictive controller for the regulation of a PEM fuel cell described by a model which accounted for spatial dependencies of voltage, current, temperature and materials flow. The objective for this control strategy was to meet power demand robustly. The authors however reduced the spatial model to a simplified one to implement NMPC. The difference between the work by Golbert and Lewin [47] and ours lies in the objective of the modeling. Instead of developing a distributed model and then converting it to a manageable one for designing controller, control relevant models of solid oxide fuel cell have been developed in our works and then NMPC has been applied to control the system.

The control objective of (Inui et al. [61]) was to keep cell temperature distribution constant to ensure durability of ceramic material used as electrolyte. This was done by optimizing the operating parameters of air utilization and the inlet gas temperature of the planar SOFC by minimizing the cell temperature shift from its nominal value. Controller design for a SOFC/GT hybrid system is also discussed in (Rao and Rawlings [116]). The authors however used a multiloop feedback-feedforward control scheme to control the generated power of the system.

Majority of the published works consider controlling fuel cell systems connected in power network whereas this work views the fuel cell system as a stand-alone power generation plant for home or, a small community.

2.3 Model Predictive Control

Model predictive control (MPC) has presented itself as the most advanced control technology in the recent years. Its ability to handle multivariate problem and to incorporate physical limitations of process have stirred interest both in the academic world and in industry. A detailed review of MPC from an academic point of view

can be found in (Clarke and Scattolini [29], Garcia et al. [45], Morari and Lee [98]). Rawlings [117] provides a good introductory tutorial on theory and application of model predictive control.

Recently there has been a steady increase of interest in nonlinear model predictive control. The interest is driven by the fact that today's process needs to operate closer to the constraints for more benefit and tighter environmental and safety regulations. These demands can be satisfied more strictly, if the inherent process nonlinearities are considered instead of approximating linear models. Nonlinear model predictive control, which is a generalized extension of popular model predictive control, is well suited for this case. A more detailed discussion on nonlinear model predictive control and moving horizon state estimation can be found in (Allgower and Findeisen [5], Allgower et al. [6, 7], Henson and Seborg [55], Maune [95], Rao and Rawlings [116], Trierweiler and Secchi [132]).

One of the main drawbacks of MPC is its inability to incorporate model uncertainties which has produced interest in the research of robust MPC (Cuzzola et al. [30], Kouvaritakis et al. [75], Lu and Arkun [89]). Several schemes that guarantee stability in the state feedback nonlinear model predictive control has also been published (Chen and Ballance [27], Nicolao et al. [102]). Much fewer results are available in the case when not all states are directly measured. To overcome this problem, often a state observer together with a stabilizing state feedback NMPC can be used (Findeisen et al. [42]). Similar approach has been used in this work.

Linear MPC has been applied quite successfully to different industrial problems in the past few years particularly in the chemical and hydrocarbon industry. The applications range from boiler-turbine co-ordination (Havlena and Findejs [53]), nitrogen purification column (Bian and Henson [13]), steam temperature control, distillation column control, combustion control and optimization. For an overview of applications of advanced control in power generation and industrial energy, see the survey papers (Donne et al. [36], Oluwande [104]).

On the other hand, the nonlinear counterpart of MPC has not been so successful

due to its inherent complexity. One of the major drawbacks in applying nonlinear MPC is its large online computational load. Several researchers have put their effort in developing efficient and robust nonlinear model predictive control particularly for industrial applications. Several review articles from industrial perspective can be found in (Camacho and Bordons [21], Clarke [28], Diehl et al. [34], Qin and Badgwell [112], Zheng [147]) and more recently by (Qin and Badgwell [114]).

Cannon et al. [23] combined linear techniques with Linear Difference Inclusion in order to apply MPC to a rolling mill problem. The model of the rolling mill is described by a set of algebraic and differential/integral nonlinear equations, discretized to give a suitable time-varying uncertain linear model. Through successive optimization of an approximate cost derived by linearization about predicted trajectories, an MPC law was obtained which required less computational load.

Tuning of model predictive control parameters, namely, prediction and control horizon, sampling interval and weights have been addressed by several authors. Tuning rules have been developed based on stability, robustness and performance (Clarke and Scattolini [29], Lee and Yu [82], Oshima et al. [105], Shridhar and Cooper [124, 125]). A detailed review of recent tuning guidelines can be found in (Shridhar and Cooper [125]).

2.4 State Estimation

The system model is often expressed as set of nonlinear ODEs for nonlinear model predictive control. For a system where all the states are measurable, the application of MPC is straightforward. In practical cases, most states are not measurable. To overcome this problem, a state observer together with a nonlinear state feedback MPC can be employed.

Estimation of states of linear systems can be done by least square estimation technique, recursive estimation, Luenberger and moving horizon state estimator, or Kalman filter (Henson and Seborg [56], Jazwinski [67], Lewis [83]). States of nonlinear systems can be estimated by using extended Kalman filter, extended Luenberger observer and

moving horizon estimator, and recently by unscented Kalman filter (UKF) and different variants of particle filter. Of them EKF is the mostly widely used nonlinear state estimator which utilizes the state estimating power of Kalman filter by linearizing the nonlinear functions around the predicted values (Anderson and Moore [8]).

The UKF, originally proposed by Julier et al. [71], uses a deterministic sampling approach to capture the mean and covariance using a minimal set of carefully chosen sample points. UKF can capture the posterior mean and covariance of any nonlinear system accurately upto second order whereas EKF can capture these properties upto first order only. A detailed description of UKF can be found in (Haykin [54], Julier [70], Julier et al. [71], Lee [80], Rui and Chen [120], Wan and Merwe [141, 142]).

In addition to parametric state estimation techniques, there has been a recent development of non-parametric methods. Instead of using any functional form, these techniques use a set of random samples, also called particles, to estimate the posteriors. This technique is thus known as particle filters. Detailed overview of particle filter (PF) and its different variants can be found in (Gordon et al. [48], Liu and Chen [88], Rui and Chen [120]). Rawlings and Bakshi [118] and Table 1 of Daum [32] provide a detailed comparison of the currently available nonlinear observers - extended Kalman filter, unscented Kalman filter, particle filter, and moving horizon state estimation.

2.5 Convective Loop Reactor

Natural convection loops showing chaotic behavior are used in solar energy heating and cooling systems, reactor, turbine, engine cooling systems, greenhouses, geothermal power production and in process industries. Chaos in such convective loop systems in general can be beneficial or detrimental depending on the process and the objective. Since it is associated with vigorous change in states, it is beneficial for processes where mixing, heat transport and chemical reactions are important. However due to the oscillation, chaos may lead to vibrations and fatigue failure to the physical equipment, irregular and oscillation of process operating conditions and increased

drag of fluid flow systems.

Ehrhard and Müller [39] in their paper investigated natural convection in a closed loop. They first developed a first principal model of the loop based on heat transfer law. They also accounted for the nonsymmetrical arrangement of heat sources and sinks. Finally, the model is reduced to a set of nonlinear ordinary differential equations. Then through experimental and analytical data, it is shown that this loop is characterized by nonlinear effects and can show stable, unstable or, chaotic regimes based on the heating rate.

Abed and Fu [1, 2] in their papers have shown ways for local stabilization of nonlinear systems with Hopf and Stationary bifurcation. Sufficient conditions are also obtained for the local stabilization of nonlinear systems whose linearization has a pair of simple, nonzero imaginary eigenvalues. The greatest contribution in this area lies perhaps in Ott et al. [106] who have shown that small time dependent perturbations can be effectively used to convert a chaotic attractor to any of a large number of possible attracting time periodic motions. The method utilizes delay coordinate embedding and can be used on experimental situations where knowledge of the system dynamics is not available.

Like Ott et al. [106], Singer et al. [126] in their paper through experimental and simulation results have also shown how a simple low energy feedback controller like an on-off controller can stabilize a chaotic system. The developed control action is based on the deviation of the vertical temperature difference from the equilibrium point, which stabilizes the states to their equilibrium points.

Wang and Abed [143] have also suggested a feedback control synthesis technique for relocating and ensuring stability of bifurcated limit cycles to a convective loop problem. The authors showed that stability could be ensured in several different ways, one of which is replacing the chaotic behavior by its equilibrium or, replacing the limit cycle with a relatively small amplitude limit cycle. For this purpose, they have used a small washout filter to delay and to extinguish chaos in the model and developed linear and nonlinear feedback control law.

Recently Bošković and Krstić [17] have investigated a thermal convective loop and developed a nonlinear feedback control law to achieve global stability using boundary control of velocity and temperature. The nonlinear control law is developed based on the discretized model of nonlinear PDE in space using the finite difference method and resultant high order system of coupled nonlinear ODE's.

2.6 Fault Detection and Identification

Fault Detection and Isolation (FDI) is an important part of any automation process. Early detection of fault and isolation of the root cause can help avoid abnormal situation and reduce production loss. Due to the broad scope of the nature of the processes and faults, a number of widely different approaches have been developed over the years for fault detection and isolation. They include a number of techniques such as, the fault trees and diagraphs, analytical approaches, and knowledge-based FDI systems.

From modeling point of view, there are methods that require fairly accurate model, semi-quantitative model, or qualitative model. Contrarily, there are methods that do not rely on any explicit model at all. Rather they use process history to detect and isolate faults.

Based on the nature of the underlying models, FDI techniques can be classified into three main categories: quantitative model-based, qualitative model-based and process history-based methods. Good reviews of different FDI techniques can be found in survey papers by (Basseville [10], Frank [44], Gertler [46], Isermann [63], Patton et al. [109], Willsky [144]), and recently by (Venkatasubramanian et al. [137, 138, 139]).

The first principle models are obtained based on the physical understanding of the process (Himmelblau [59]). In chemical processes, mass, energy and momentum balances as well as hard constraint of the processes are used in the development of the model equations. Even though the insight of the process can make the fault detection technique more reliable, due to the nonlinear nature of most processes, the inherent nonlinear first principles models are seldom used in the quantitative model-based FDI

techniques.

In contrast to quantitative model-based approaches, process history-based methods only require process historical data. The process data are then analyzed and used as *a priori* knowledge for diagnosis. Based on the techniques of information extraction, process history-based method can be classified into qualitative and quantitative methods.

Quantitative methods can further be classified into statistical and non-statistical methods. Principal component analysis (PCA), first proposed by Pearson [110] and later developed by Hotelling [60], is a multivariate statistical technique which utilizes first few principal components of the covariance matrix for capturing process variable correlation.

A number of articles illustrating the use of PCA as statistical process analysis and control tool, as well as a fault detection and isolation technique have appeared in the literature (Dunia et al. [38], Jackson [64], Johnson and Wichern [68], Joliffe [69], Kresta et al. [76], MacGregor and Kourti [91], Nomikos and MacGregor [103]). Dong and McAvoy [35] utilized a nonlinear PCA method for detecting faults of a nonlinear batch process.

To handle time varying nature of the real processes, recursive PCA has also been proposed in several papers (Li et al. [84], Qin [113], Wold [145]). Dunia and Qin [37] presented a methodology to analyze faulty subspace for process and sensor fault detection. Bakshi [9] presented multiscale PCA which integrates PCA and wavelet analysis for identifying linear relationship and auto-correlated measurements.

While process history-based fault detection methods do not rely on an explicit model, their inability to use any process model is a drawback. An intuitive solution is to integrate these complementary features of quantitative model-based and process history-based FDI techniques to form a hybrid method. There has already been some work on hybrid FDI techniques among which the two-tier approach by Venkatasubramanian and Rich [136], analytic and knowledge-based redundancy approach by Frank [44], and blackboard-based cooperative problem-solving framework by Vedam et al. [135]

are innovative.

Chapter 3

Control Relevant Modeling of Solid Oxide Fuel Cell System

3.1 Introduction

Fuel cells are electrochemical devices that generate electrical energy directly from chemical reactions. Unlike heat engine or gas turbine where there are losses due to Carnot cycle efficiency limitation and mechanical losses, chemical energy is directly converted to electrical energy and thus the fuel cell plant efficiency can be as high as 40-55%. In addition, the heat generation from the electrochemical reactions in a fuel cell can also be used for cogeneration applications increasing the efficiency upto 70% (Fuel Cell Handbook, Edition 7 [134]). Some other potential features of fuel cell include no moving parts, quiet operation, flexibility in fuel types and size of the fuel cell, and most of all rapid load following capability (Fuel Cell Handbook, Edition 7 [134]). Another attractive feature of fuel cell is that it demonstrates same efficiency irrespective of its size, which makes it useful for a versatile range of applications including power generation for home or a commercial building, mobile equipments, and automobile. These advantages have generated enormous interest in the research of fuel cell design, modeling and control.

In this work, two sets of dynamic models of different details are presented by considering electro-chemical and thermal aspects of fuel cell. Both of the models are represented by first order ordinary differential equations and thus are useful for simu-

lating transient behavior of the fuel cell as well as designing model-based controllers. In addition, simplified thermal dynamic models of fuel cell system components are developed and connected to fuel cell to simulate the dynamic behavior of fuel cell system. The fuel cell system dynamic model consists of only nonlinear ordinary differential equation and thus can be utilized to design system wide controller such as nonlinear MPC. The model can also be used to estimate unmeasured states using state estimators. The advantage of using capacitor connected in parallel with the fuel cell along with its formulation has also been described in this chapter.

The work is organized as follows: first, general principle of a fuel cell is described followed by the modeling objective in section 3.3; next, two sets of models, lumped and detail model, are presented in section 3.4 and section 3.5 followed by fuel cell simulation in section 3.8.1. In this section, both dynamic and steady state results are simulated and analyzed. Next the advantage of using capacitor as an auxiliary power source is described along with necessary formulations in section 3.6. In section 3.7 and 3.8.3 the fuel cell system model is developed and simulated to analyze performance of transient system.

3.2 General Principle

A typical fuel cell consists of an electrolyte in contact with anode and cathode on either side. Hydrogen rich fuel and air are continuously fed into the fuel cell for generating electricity. The electrolyte acts as a barrier between anode and cathode allowing only certain types of ions to pass through it. Fuel cells are mainly classified depending on the nature of the electrolytes. Some of the most common fuel cells are molten carbonate fuel cell (MCFC), proton exchange membrane fuel cell (PEMFC), polymer electrolyte fuel cell (PEFC) and solid oxide fuel cell (SOFC) (Fuel Cell Handbook, Edition 7 [134]). Solid oxide fuel cell, as its name suggests, uses a solid metal oxide as electrolyte. The cell operates at high temperature, which makes it particularly useful for internal reforming of natural gases. The high temperature exit gases can be used further to generate electricity by a turbine. SOFC can be designed in different shapes and sizes due to the solid nature of the electrolyte, for example

planer and tubular. The high temperature of the SOFC however imposes a stringent requirement on the material selection due to the thermal expansion mismatch between anode, electrolyte, cathode and connector materials. Thus, it is important to operate SOFC in such a way that the stack temperature remains within the design range.

In a planer SOFC, several cells are stacked and connected in series to complete the circuit. At each cell, hydrogen releases electrons at the anode surface, which travel through the outer circuit and combine with oxygen to produce oxide ions. Electrolyte, which acts as a separator between hydrogen and oxygen, and thus prevents direct combustion, allows only certain types of ions to pass through it. SOFC usually uses Y_2O_3-stabilized ZrO_2 (YSZ) as electrolyte, which allows oxide ion to pass through it to reach the anode surface, where the oxide ion combines with H^+ to form water. The reactions can be summarized as follows:

$$\text{Anode:} \qquad H_2 \rightarrow 2H^+ + 2e \tag{3.1}$$

$$\text{Cathode:} \qquad \frac{1}{2}O_2 + 2e \rightarrow O^= \tag{3.2}$$

$$\text{Overall:} \qquad H_2 + \frac{1}{2}O_2 \rightarrow H_2O + \text{ Heat} \tag{3.3}$$

The electrode potential difference, ΔE that drives the reaction to take place and flow of ions through the circuit can be expressed by Nernst equation:

$$\Delta E = \Delta E_0 + \frac{RT}{2F} \ln \frac{p_{H_2} p_{O_2}^{0.5}}{p_{H_2O}} \tag{3.4}$$

where, ΔE_0[volt] is the standard cell potential; p_{H_2}, p_{O_2} and p_{H_2O} are the partial pressures of hydrogen, oxygen and steam in [atm]; T [K] is the cell electrode temperature at which the reaction is taking place; R [=1 atm/kmol.K] and F [=96485.34 s.A/mol] are the universal gas constant and the Faraday's constant respectively. The Nernst model in eqn. (3.4) can thus be used to predict cell voltage provided standard cell potential, partial pressures and electrode temperature are known which can be derived in terms of species and energy balances.

3.3 Modeling Objective

Knowledge of the transient and steady state response of the solid oxide fuel cell is important for studying fuel cell performance as well as designing the controller. The level of modeling sophistication thus depends on the objective and can vary from simple linear state-space models to complex 3-D models. The models can also specifically be derived to simulate steady state or dynamic behavior.

Since in this work, the modeling objective is driven by the requirement of a control relevant dynamic model that can predict the cell terminal voltage and system component temperatures as well as design controller with relative ease, certain model characteristics have to be identified:

- The model should comprise a set of linear or, nonlinear ODEs to predict transient behavior of the fuel cell. In other words the model should be zero-dimensional to avoid distributed model comprising of a set of PDEs which makes it difficult to design controllers.
- It should be able to predict all the important variables including terminal voltage, pressure and temperature.
- Model should be valid for all operating regions, which is the main driving factor for building a first principle model rather than a data based model.

Based on these modeling objectives, two types of models are presented in the following sections. First, a completely "lumped model" is derived which assumes uniform temperature throughout the cell including both the solid phase and the gas phase. Even though this assumption is fairly valid at lower current load, where the temperatures of electrode, interconnector and unreacted gases do not differ much, at higher current load, this may not be the case. Thus a second model, named, "detail model" is presented which assumes that different components namely electrode, interconnector, fuel and air has different temperature distributions. Note that the term "detail model" used in this work, is relative to the completely lumped model. In addition,

lumped thermal models for the balance of fuel cell system *e.g.*, heat exchangers, reformer and burner are presented and then integrated with lumped and detailed model respectively to simulate dynamic behavior of fuel cell system stack voltage due to load changes and other disturbances.

3.4 Lumped Model

The lumped model of a stand-alone planer solid-oxide fuel cell fed with hydrogen and air is developed based on the following assumptions:

- The gases are ideal.
- Pressure is constant inside the gas channel.
- The ratio of interior and exterior pressures at the reaction interface is large enough to consider that the orifice is choked.
- Uniform temperature distribution for the entire fuel cell stack.
- Ideal mixing of the inlet and outlet gases inside the fuel cell stack. Hence, the exit temperature of the fuel and air are same as the inside temperature of the fuel.
- Heat capacities of the fuel and air are negligible.
- Negligible heat loss to the surroundings.

Based on these assumptions an overall material and energy balance is performed around the fuel cell stack as shown in fig. 3.1(a).

3.4.1 Species Balance

The i-th component material balance for the fuel cell stack can be written as (Felder and Rousseau [41], Sedghisigarchi and Feliachi [122]):

$$\frac{PV}{RT_s}\frac{dx_i}{dt} = \dot{n}_i^{in} - \dot{n}_i^{out} + \dot{n}_i^{r} \tag{3.5}$$

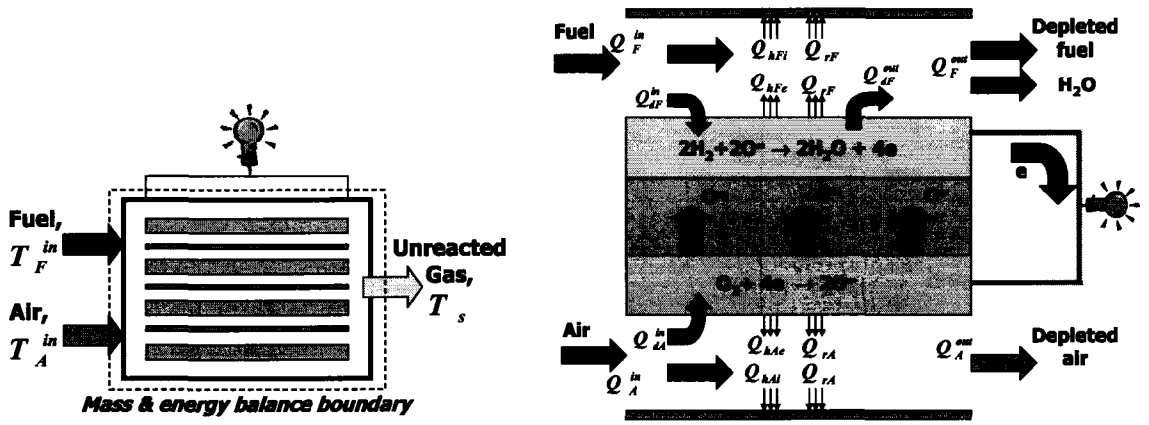

(a) (b)

Figure 3.1: Energy terms in (a) the lumped model and (b) the detail model

where P [atm] and T_s [K] are the stack pressure and temperature; V [m^3] is the compartment volume; x_i is the exit molarity of the i-th component; $\dot{n}_i^{in}$, $\dot{n}_i^{out}$ and $\dot{n}_i^r$ are the inlet, outlet, and reactive molar flow rates of the i-th component in mol/s.

Component balance for hydrogen in terms of its partial pressure p_{H_2} can thus be expressed as:

$$\frac{dp_{H_2}}{dt} = \frac{RT_s}{V_{an}}(\dot{n}_{H_2}^{in} - \dot{n}_{H_2}^{out} - \dot{n}_{H_2}^r) \tag{3.6}$$

where, V_{an} [m^3] is the anode compartment volume; $\dot{n}_{H_2}^{in}$, $\dot{n}_{H_2}^{out}$ and $\dot{n}_{H_2}^r$ are the inlet, outlet, and reactive molar flow rates of H_2 [mol/s]. The reactive and exit flow rates of hydrogen can be expressed by (Padulles et al. [108]):

$$\dot{n}_{H_2}^r = 2K_r I \tag{3.7}$$

$$\dot{n}_{H_2}^{out} = K_{H_2} p_{H_2} \tag{3.8}$$

where, $K_r = \frac{N_0}{4F}$; I [amp] is the stack current; N_0 is the number of cells associated in series in the stack; K_{H_2} is the valve molar constant for hydrogen.

Defining $\tau_{H_2} = \frac{V_{an}}{K_{H_2} RT_s}$, eqn. (3.6) can then be written as:

$$\frac{d}{dt}p_{H_2} = \frac{1}{\tau_{H_2} K_{H_2}}(\dot{n}_{H_2}^{in} - K_{H_2} p_{H_2} - 2K_r I) \tag{3.9}$$

Since K_{H_2} is a constant, τ_{H_2} is a function of cell temperature only and can be expressed

as $\tau_{H_2} = \frac{\tau^*_{H_2} T^*}{T_s}$ where $\tau^*_{H_2} = \tau_{H_2}|_{T_s=T^*}$. Eqn. (3.9) thus can be rewritten as:

$$\frac{dp_{H_2}}{dt} = \frac{T_s}{K_{H_2}\tau^*_{H_2}T^*}(\dot{n}^{in}_{H_2} - K_{H_2}p_{H_2} - 2K_rI) \tag{3.10}$$

Similarly component balances for O_2 and H_2O lead to the following set of equations:

$$\frac{dp_{O_2}}{dt} = \frac{T_s}{K_{O_2}\tau^*_{O_2}T^*}(\dot{n}^{in}_{O_2} - K_{O_2}p_{O_2} - K_rI) \tag{3.11}$$

and,

$$\frac{dp_{H_2O}}{dt} = \frac{T_s}{K_{H_2O}\tau^*_{H_2O}T^*}(\dot{n}^{in}_{H_2O} - K_{H_2O}p_{H_2O} + 2K_rI) \tag{3.12}$$

3.4.2 Energy Balance

In the lumped stack modeling, it is assumed that there is no temperature variation inside the fuel cell, which means that all the components of the fuel cell - electrode, interconnector and gases inside channels, posses the same temperature at any instance. It is further assumed that the heat capacity of the gases inside the channels are negligible compared to the solid components of the fuel cell. Then the dynamic model of the cell temperature, T_s, can be found by performing energy balance around the entire fuel cell stack:

$$m_s\bar{C}_{ps}\frac{dT_s}{dt} = \sum \dot{n}^{in}_i \int_{T_{ref}}^{T_{in}} C_{p,i}(T)dT - \sum \dot{n}^{out}_i \int_{T_{ref}}^{T_s} C_{p,i}(T)dT - \dot{n}^r_{H_2}\Delta\hat{H}^\circ_r - V_sI \tag{3.13}$$

where, m_s and $\bar{C}_{ps}$ are the mass and average specific heat of fuel cell materials excluding gases; $C_{p,i}$ is the specific heat of i-th fuel or air gas entering the system; $\Delta\hat{H}^\circ_r$ is the specific heat of reaction of eqn. (3.3); V_s is the stack voltage.

Considering constant specific heat of the gases for the operating temperature range, the above equation can be simplified to:

$$m_s\bar{C}_{ps}\frac{dT_s}{dt} = \sum \dot{n}^{in}_i \bar{C}^{in}_{p,i}(T_{in} - T_{ref}) - \sum \dot{n}^{out}_i \bar{C}^{out}_{p,i}(T_s - T_{ref}) - \dot{n}^r_{H_2}\Delta\hat{H}^\circ_r - V_sI \tag{3.14}$$

where,

$$\bar{C}_{p,i}^{in} = C_{p,i}|_{(T_{in}+T_{ref})/2}$$
$$\bar{C}_{p,i}^{out} = C_{p,i}|_{(T_s+T_{ref})/2}$$

3.4.3 Stack Voltage

Applying Nernst's equation and considering ohmic, activation and concentration polarization, the stack voltage can be expressed as,

$$V_s = V_0 - \eta_{ohm} - \eta_{act} - \eta_{con} \tag{3.15}$$

where, the open circuit voltage, V_0 is

$$V_0 = N_0 \Delta E = N_0 \Big[\Delta E_0 + \frac{RT_s}{2F} \ln \frac{p_{H_2} p_{O_2}^{0.5}}{p_{H_2O}}\Big] \tag{3.16}$$

Here, standard cell potential ΔE_0 exhibits linear relationship with cell temperature and can be approximated from the experimental data provided in Table 2-3 of (Fuel Cell Handbook, Edition 6 [133]):

$$\Delta E_0(V) = 1.2586 - 0.000252 T_s(K) \tag{3.17}$$

Ohmic polarization occurs because of resistance to the flow of ions through different components of cell materials. The loss can be expressed as:

$$\eta_{ohm} = r(T_s) I \tag{3.18}$$

The cell resistance, $r(T_s)$, however is a function of cell electrode temperature and can be expressed by the second order Steinhart Hart equation:

$$r(T_s) = r_0 \exp\Big[\alpha\Big(\frac{1}{T_s} - \frac{1}{T_0}\Big)\Big] \tag{3.19}$$

where, r_0 [ohm] is the internal resistance at temperature T_0 [K] and α is a constant.

Activation and concentration polarization can be calculated by the following equations (Braun [19], Larminie and Dicks [78], Sedghisigarchi and Feliachi [122]):

$$\eta_{act} = a + b \log I \tag{3.20}$$

and,

$$\eta_{con} = \frac{RT_s}{2F} \ln\left(1 - \frac{I}{I_L}\right) \tag{3.21}$$

where, a and b are the Tafel constant and Tafel slope respectively; I_L is the limiting current.

3.5 Detail Model

As stated earlier, at higher current load the assumption of uniform temperature distribution throughout the fuel cell in lumped model, as described in section 3.4, may not be valid. Thus, in this section a relatively more detail model is developed where it is assumed that different cell components have different temperature distributions and thus the model is "detailed" compared to the "lumped" model. The major assumptions that differentiate it from the lumped model are described below:

- Different temperatures among electrode, interconnector, fuel and air side gases.
- Ideal mixing of gases inside the fuel cell channels so that fuel and air exit temperatures are same as the temperature inside the fuel and air channels respectively.
- No temperature variation in the axial direction.

Based on these assumptions material and energy balances are performed around electrode, interconnector, fuel gas channel and air gas channel of the fuel cell as depicted in fig. 3.1(b). Since in this model only temperature distributions are assumed to be different, species balance around the cell remains same as described in section 3.4.1, and so is the cell voltage calculation in section 3.4.3. The stack temperature T_s in eqns.(3.16,3.17,3.19,3.21) however has to be replaced by electrode temperature, T_e.

3.5.1 Energy Balance Around Electrode

The electrode control volume consists of the anode, electrolyte and the cathode. Even though the electro-chemical reactions take place at the anode and cathode near the

surfaces of the electrolyte, and thus have temperature variations in the direction vertical to the surface area, it can be assumed constant due to very small thickness of the electrode. The temperature variation along the flow direction is also assumed constant, and thus the electrode temperature T_e dynamics can be expressed as a function of diffusive, convective, radiative, and reactive heat transfer terms (fig. 3.1(b)):

$$\rho_e A_c \Delta w_e \bar{C}_{pe} \frac{dT_e}{dt} = (Q_{dF}^{in} - Q_{dF}^{out}) + (Q_{dA}^{in} - Q_{dA}^{out}) - (Q_{hFe} + Q_{rF} + Q_{hAe} + Q_{rA}) - Q^r - \dot{W} \quad (3.22)$$

Here, A_c, Δw_e, ρ_e and $\bar{C}_{pe}$ are the electro-chemical surface area, thickness, density and specific heat of the electrode material respectively. The fuel side diffusion heat terms in eqn. (3.22) can be expressed as:

$$Q_{dF}^{in} = \dot{n}_{H_2}^r \int_{T_{ref}}^{T_F} C_{p,H_2}(T) dT \quad (3.23)$$

$$Q_{dF}^{out} = \dot{n}_{H_2O}^r \int_{T_{ref}}^{T_F} C_{p,H_2O}(T) dT \quad (3.24)$$

where, $\dot{n}_{H_2}^r = \dot{n}_{H_2O}^r = 2K_r I$ and T_F is the exit temperature of the depleted fuel. The air side heat transfer terms in and out of the electrode through diffusion in eqn. (3.22) can be expressed as:

$$Q_{dA}^{in} = \dot{n}_{O_2}^r \int_{T_{ref}}^{T_A} C_{p,O_2}(T) dT \quad (3.25)$$

$$Q_{dA}^{out} = 0 \quad (3.26)$$

where, $\dot{n}_{O_2}^r = K_r I$, and T_A is the exit temperature of depleted air. The convective heat transfers between electrode and fuel/air gases in eqn. (3.22) can be written as:

$$Q_{hFe} = h_{Fe} A_c (T_e - T_F) \quad (3.27)$$

$$Q_{hAe} = h_{Ae} A_c (T_e - T_A) \quad (3.28)$$

Here, The the fuel side and air side heat transfer coefficients h_{Fe} and h_{Ae} are also functions of T_F and T_A respectively and are evaluated at each instance empirically (Lienhard IV and V [86], Perry et al. [111]). The radiative heat transfer terms between electrode and interconnector of fuel side and air side in eqn. (3.22) can be expressed

as:

$$Q_{rF} = \frac{\sigma A_c (T_e^4 - T_i^4)}{1/\epsilon_a + 1/\epsilon_i - 1} \tag{3.29}$$

$$Q_{rA} = \frac{\sigma A_c (T_e^4 - T_i^4)}{1/\epsilon_c + 1/\epsilon_i - 1} \tag{3.30}$$

where, $\sigma = 5.6704 \times 10^{-8}\ W/m^2.K^4$ is the Boltzman constant; T_i[K] is the interconnector temperature; ϵ_a, ϵ_c, and ϵ_i are the emissivity constants of anode, cathode and interconnector materials respectively. The geometric factor of radiation in this case is assumed to be 1. Last, the heat generation and shaft work done by the fuel cell can be expressed as:

$$Q^r = -\dot{n}^r_{H_2} \Delta \hat{H}^\circ_r \qquad \text{and} \qquad \dot{W} = V_s I \tag{3.31}$$

3.5.2 Energy Balance Around Interconnector

The interconnector temperature, T_i dynamics can be expressed by the following equation:

$$\rho_i A_i \Delta w_i \bar{C}_{pi} \frac{dT_i}{dt} = Q_{hFi} + Q_{rF} + Q_{hAi} + Q_{rA} \tag{3.32}$$

where, ρ_i, A_i, Δw_i, $\bar{C}_{pi}$, and T_i are the density, area, thickness, specific heat and temperature of the interconnect materials respectively. Convective heat transfers between interconnect and fuel/air in eqn. (3.32) can be expressed as:

$$Q_{hFi} = h_{Fi} A_i (T_F^{out} - T_i) \tag{3.33}$$

$$Q_{hAi} = h_{Ai} A_i (T_A^{out} - T_i) \tag{3.34}$$

where, h_{Fi} and h_{Ai} are fuel side and air side convective heat transfer coefficients adjacent to the interconnector surface respectively which are estimated empirically at each instance. The radiative heat transfer terms in eqn. (3.32) are expressed in eqn. (3.29) and eqn. (3.30). For planer SOFC the area A_i can be approximated as the electro-chemical surface area, A_c.

3.5.3 Energy Balance Around Fuel Side

The dynamic model of exit fuel temperature, T_F can be expressed as:

$$\sum \frac{p_i V_{channel} C_{pi}^{out}}{RT_F} \frac{dT_F}{dt} = (Q_F^{in} - Q_F^{out}) + (Q_{dF}^{out} - Q_{dF}^{in}) + (Q_{hFe} - Q_{hFi}) \quad (3.35)$$

Here, heat in, Q_F^{in} and heat out, Q_F^{out} of fuel cell by fuel flow can be expressed as:

$$Q_F^{in} = \sum \dot{n}_i^{in} \int_{T_{ref}}^{T_F^{in}} C_{P,i}(T) dT \quad (3.36)$$

$$Q_F^{out} = \sum \dot{n}_i^{out} \int_{T_{ref}}^{T_F} C_{P,i}(T) dT \quad (3.37)$$

where, T_F^{in} is the temperature of fuel entering the SOFC. The diffusive and convective heat transfer terms Q_{dF}^{in}, Q_{dF}^{out}, Q_{hFe}, and Q_{hFi} in eqn. (3.35) are expressed in eqns. (3.23), (3.24), (3.27) and, (3.33) respectively. If the energy stored by fuel gas is assumed to be negligible and the specific heats of fuel gases are assumed to be constant over the operating temperature region, then eqn. (3.35) reduces to an algebraic equation:

$$T_F = N_F / D_F \quad (3.38)$$

where,

$$N_F = -Q_F^{in} + \overbrace{-h_{Fe}A_c T_e - h_{Fi}A_i T_i}^{-h_F A_c (T_e + T_i)} + \left[-\sum \dot{n}_i^{out} \bar{C}_{P,i}^{out} + \dot{n}_{H_2O}^{r} \bar{C}_{p,H_2O}^{out} - \dot{n}_{H_2}^{r} \bar{C}_{p,H_2}^{out} \right] T_{ref}$$

$$D_F = \dot{n}_{H_2O}^{r} \bar{C}_{p,H_2O}^{out} - \dot{n}_{H_2}^{r} \bar{C}_{p,H_2}^{out} - \sum \dot{n}_i^{out} \bar{C}_{P,i}^{out} \underbrace{-h_{Fe}A_c - h_{Fi}A_i}_{-2h_F A_c}$$

Detailed derivation of the above equation is provided below:

$$
\begin{aligned}
&\underbrace{\sum \dot{n}_i^{in}\bar{C}_{P,i}^{in}(T_F^{in}-T_{ref})}_{Q_F^{in}} - \underbrace{\sum \dot{n}_i^{out}\bar{C}_{P,i}^{out}(T_F-T_{ref})}_{Q_F^{out}} \\
&+\underbrace{\dot{n}_{H_2O}^{r}\bar{C}_{p,H_2O}^{out}(T_F-T_{ref})}_{Q_{dF}^{out}} - \underbrace{\dot{n}_{H_2}^{r}\bar{C}_{p,H_2}^{out}(T_F-T_{ref})}_{Q_{dF}^{in}} \\
&+\underbrace{h_{Fe}A_c(T_e-T_F)}_{Q_{hFe}} - \underbrace{h_{Fi}A_i(T_F-T_i)}_{Q_{hFi}} = 0 \\
\Rightarrow &\left[\dot{n}_{H_2O}^{r}\bar{C}_{p,H_2O}^{out} - \dot{n}_{H_2}^{r}\bar{C}_{p,H_2}^{out} - \sum \dot{n}_i^{out}\bar{C}_{P,i}^{out} - h_{Fe}A_c - h_{Fi}A_i\right]T_F \\
&= -Q_F^{in} - h_{Fe}A_cT_e - h_{Fi}A_iT_i \\
&\quad + \Big[-\sum \dot{n}_i^{out}\bar{C}_{P,i}^{out} + \dot{n}_{H_2O}^{r}\bar{C}_{p,H_2O}^{out} - \dot{n}_{H_2}^{r}\bar{C}_{p,H_2}^{out}\Big]T_{ref} \\
&\quad -Q_F^{in} + \overbrace{-h_{Fe}A_cT_e - h_{Fi}A_iT_i}^{-h_FA_c(T_e+T_i)} + \Big[-\textstyle\sum \dot{n}_i^{out}\bar{C}_{P,i}^{out} \\
&\quad \cdots + \dot{n}_{H_2O}^{r}\bar{C}_{p,H_2O}^{out} - \dot{n}_{H_2}^{r}\bar{C}_{p,H_2}^{out}\Big]T_{ref} \\
\Rightarrow &T_F = \frac{\dot{n}_{H_2O}^{r}\bar{C}_{p,H_2O}^{out} - \dot{n}_{H_2}^{r}\bar{C}_{p,H_2}^{out} - \sum \dot{n}_i^{out}\bar{C}_{P,i}^{out}}{\cdots \underbrace{-h_{Fe}A_c - h_{Fi}A_i}_{-2h_FA_c}}
\end{aligned}
\tag{3.39}
$$

Here, specific heat of i-th component $\bar{C}_{p,i}^{in}$ and $\bar{C}_{p,i}^{out}$ are evaluated at $(T_{in}+T_{ref})/2$ and $(T_F+T_{ref})/2$. Hence, eqn. (3.39) takes the nonlinear algebraic form $T_F = f(T_F)$.

3.5.4 Energy Balance Around Air Side

The dynamic model of air exit temperature, T_A can be expressed as:

$$
\begin{aligned}
\sum \frac{p_iV_{channel}C_{pi}^{out}}{RT_A}\frac{dT_A}{dt} &= (Q_A^{in}-Q_A^{out}) \\
&\quad + (Q_{dA}^{out}-Q_{dA}^{in}) + (Q_{hAe}-Q_{hAi})
\end{aligned}
\tag{3.40}
$$

Here, Q_A^{in} and Q_A^{out} are heat in and out of fuel cell through air flow and can be expressed as:

$$
Q_A^{in} = \sum \dot{n}_i^{in}\int_{T_{ref}}^{T_A^{in}} C_{P,i}(T)dT \tag{3.41}
$$

$$
Q_A^{out} = \sum \dot{n}_i^{out}\int_{T_{ref}}^{T_A} C_{P,i}(T)dT \tag{3.42}
$$

The diffusive and convective heat transfer terms Q_{dA}^{in}, Q_{dA}^{out}, Q_{hAe} and Q_{hAi} in eqn. (3.40) are expressed in eqns. (3.25),(3.26),(3.28), and (3.34). Assuming energy stored by the

air is negligible and constant specific heat of air gases for the operating temperature range, the dynamic equation of T_A can also be reduced to an algebraic equation:

$$T_A = N_A / D_A \tag{3.43}$$

where,

$$N_A = -Q_A^{in} - \Big[\sum \dot{n}_i^{out} \bar{C}_{P,i}^{out} - \dot{n}_{O_2}^{r} \bar{C}_{p,O_2}^{out}\Big] T_{ref} \overbrace{-h_{Ae}A_c T_e - h_{Ai}A_i T_i}^{-h_A A_c (T_e + T_i)}$$

$$D_A = -\sum \dot{n}_i^{out} \bar{C}_{P,i}^{out} - \dot{n}_{O_2}^{r} \bar{C}_{p,O_2}^{out} \underbrace{-h_{Ae}A_c - h_{Ai}A_i}_{-2h_A A_c}$$

Detailed derivation of the above equation is provided below:

$$\underbrace{\sum \dot{n}_i^{in} \bar{C}_{P,i}^{in} (T_A^{in} - T_{ref})}_{Q_A^{in}} - \underbrace{\sum \dot{n}_i^{out} \bar{C}_{P,i}^{out} (T_A^{out} - T_{ref})}_{Q_A^{out}}$$

$$- \underbrace{\dot{n}_{O_2}^{r} \bar{C}_{p,O_2}^{out} (T_A^{out} - T_{ref})}_{Q_{dA}^{in}} + \underbrace{h_{Ae}A_c (T_e - T_A^{out})}_{Q_{hAe}} - \underbrace{h_{Ai}A_i (T_A^{out} - T_i)}_{Q_{hAi}} = 0$$

$$\Rightarrow \Big[-\sum \dot{n}_i^{out} \bar{C}_{P,i}^{out} - \dot{n}_{O_2}^{r} \bar{C}_{p,O_2}^{out} - h_A A_c - h_A A_i\Big] T_A^{out}$$

$$= -Q_A^{in} - \Big[\sum \dot{n}_i^{out} \bar{C}_{P,i}^{out} - \dot{n}_{O_2}^{r} \bar{C}_{p,O_2}^{out}\Big] T_{ref} - h_{Ae}A_c T_e - h_{Ai}A_i T_i$$

$$\Rightarrow T_A^{out} = \frac{-Q_A^{in} - \Big[\sum \dot{n}_i^{out} \bar{C}_{P,i}^{out} - \dot{n}_{O_2}^{r} \bar{C}_{p,O_2}^{out}\Big] T_{ref} \overbrace{-h_{Ae}A_c T_e - h_{Ai}A_i T_i}^{-h_A A_c (T_e + T_i)}}{-\sum \dot{n}_i^{out} \bar{C}_{P,i}^{out} - \dot{n}_{O_2}^{r} \bar{C}_{p,O_2}^{out} \underbrace{-h_{Ae}A_c - h_{Ai}A_i}_{-2h_A A_c}} \tag{3.44}$$

3.6 SOFC along with Capacitor

For a stand-alone solid oxide fuel cell, the model equations describing the fuel cell behavior are expressed by the species balance [eqn. (3.10), eqn. (3.11), eqn. (3.12)], energy balance [eqn. (3.13), eqn. (3.22), eqn. (3.32), eqn. (3.35), eqn. (3.40)] and the stack voltage equation [eqn. (3.15)]. These equations can be put in a concise form by:

$$\dot{x} = f(x, \dot{n}_i, I_d, V_s) \tag{3.45}$$

$$V_s = V_0(x) - r(x) I_d \tag{3.46}$$

where, x contains the states describing the partial pressures and temperatures of the SOFC models; $\dot{n}_i$ represents the inlet flow rates of fuel or air; I_d is the demand current

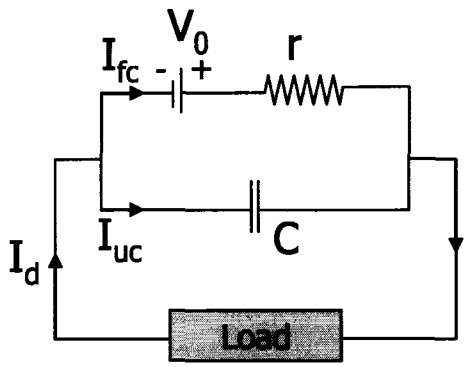

Figure 3.2: SOFC along with capacitor connected in parallel

load which passes through the fuel cell and V_s is the stack voltage produced by the fuel cell. For simplicity, only ohmic loss has been taken into consideration in the above output equation. For a stand alone fuel cell, the fuel cell current I_{fc} equals the demand current I_d. From the output equation, it is evident that a sudden change in the demand current will be associated with an instantaneous change in the stack voltage as shown by the transient responses (fig. 3.6). This instantaneous change in the stack voltage can not be avoided no matter what type of advanced control is used due to the constraints on the manipulated variables that are typically the inlet fuel and air flow rates. To avoid this sudden loss in voltage and possible damage to electrical equipment, an ultra-capacitor of sufficient capacity can be used in parallel with the fuel cell as an auxiliary power source as shown in fig. 3.2.

The advantage of the capacitor can be seen intuitively - when there is a sudden change in the demand current, the capacitor will share the load and provide additional power. Thus instead of sudden drop in the stack voltage, it drops smoothly depending on the capacitance of the ultra-capacitor. This gives an added boost to the controller connected to the SOFC system to keep the voltage at its referenced value. By avoiding sudden drop of the voltage the controller copes with only the slow change of the voltage and can bring the voltage at its reference value by increasing fuel flow rates within its constraints more easily. Mathematically this can be expressed as follows:

Assume that the current through the capacitor and the fuel cell are I_{uc} and I_{fc}

respectively. Then I_{fc} can be expressed in terms of the demand current as,

$$I_{fc} = I_d - I_{uc} \tag{3.47}$$

From the definition of capacitance, the current passing through an ultra-capacitor connected in parallel with a dc voltage source can be expressed as,

$$I_{uc} = -C_{cap}\frac{dV_s}{dt} \tag{3.48}$$

where, C_{cap} is the capacitance in farad and V_s is the terminal voltage across the capacitor and the dc voltage source. Then current through the fuel cell can be rewritten as,

$$I_{fc} = I_d + C_{cap}\frac{dV_s}{dt} \tag{3.49}$$

Stack voltage of the fuel cell as described by the output equation eqn. (3.46) then can be written as,

$$rC_{cap}\frac{dV_s}{dt} = V_0 - rI_d - V_s \tag{3.50}$$

From eqn. (3.50), it is seen that the stack voltage has now taken the form of a first-order ODE instead of a static nonlinear output equation. Thus instead of sudden voltage drop for a step increase in the demand current, the voltage drop slows down depending on the term rC, as shown in section 3.8.2.

3.7 Fuel Cell System

In the previous sections, a stand-alone fuel cell is described and modeled which can be used for simulating open loop transient behavior or designing model-based control. The SOFC under consideration is fed with H_2 as fuel and air as a source of O_2. But in practical situations a fuel cell is often associated with other components so that the SOFC plant can be fed with natural gas or other hydrogen rich fuel instead of pure hydrogen. One such SOFC system is shown in fig. 3.3 which includes a reformer for converting methane (CH_4) into hydrogen, two heat exchangers for preheating fuel and air before feeding them into the reformer and fuel cell stack respectively, one burner for burning unreacted fuel and, a splitter. Often the fuel cell system includes

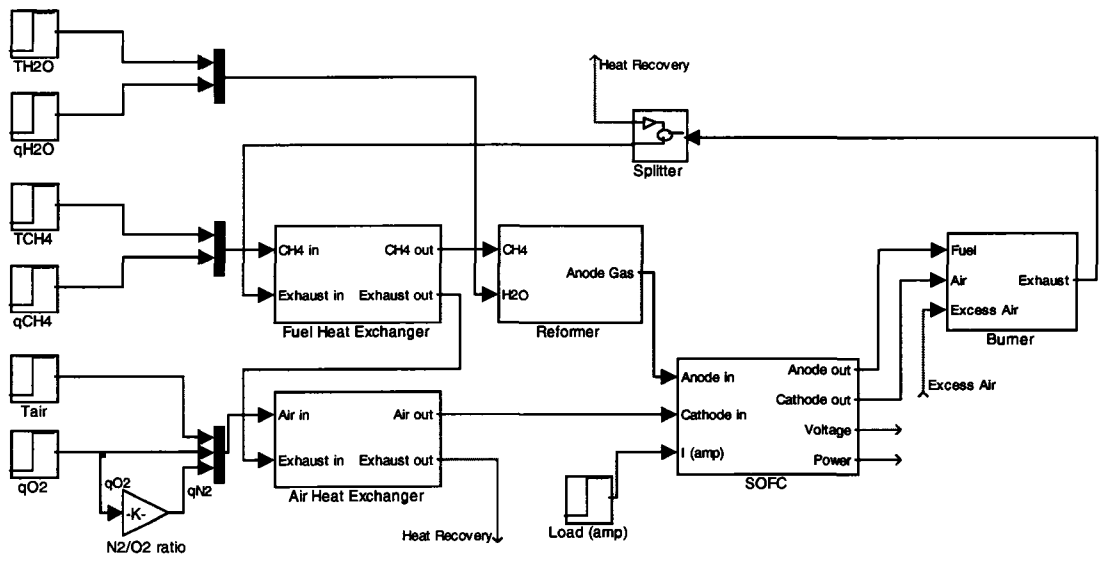

Figure 3.3: SOFC system with heat exchangers, reformer, burner and compressors

a turbine to generate auxiliary power from the exhaust gas, fuel processing unit (*e.g.*, desulphurization) and a power conditioning unit (*e.g.*, a voltage regulator, a DC/DC or, DC/AC converter). These components are an integral part of the fuel cell system and called as *balance of plant* (BOP). Examples of process flow diagrams of SOFC systems are given in fig 1-14 of (Fuel Cell Handbook, Edition 6 [133]) and in fig 3.1, fig 3.2, fig 3.12 and fig 3.14 of (Braun [19]).

In the SOFC system that is simulated in this work [fig. 3.3], methane is pressurized and fed to the fuel heat exchanger for preheating by the exhaust gas from the burner. The preheated methane then enters an external reformer along with steam where methane is being converted to hydrogen through reforming and water-gas shift reaction. The product gas from reformer enters into the anode compartment of the fuel cell stack. Pressurized air is also preheated in another heat exchanger by the hot exit gas from the fuel heat exchanger and sent to the cathode compartment of the fuel cell stack. Hydrogen from the anode compartment and oxygen from the cathode takes part into the electrochemical reactions to produce power at the electrode. The depleted fuel and air from the fuel cell stack is then fed into a burner to produce heat from the unreacted methane, hydrogen and carbon monoxide. The exhaust from the burner is then sent to the fuel and air heat exchanger consecutively as described earlier. The

exhaust gas from the air heat exchanger is then sent for heat recovery in the form of steam and hot water. The following sections provide a brief description and thermal model of different components of the fuel cell system.

Once the system model has been developed, it can be used to design model-based controller. The designing of the controller is dependent on the control objective and thus the key manipulated and controlled variables can also differ. For example, if the control objective is to improve load following performance of the system, then the stack voltage can work as a controlled variable whereas the fuel, steam and air (or, oxygen) flow rate to the fuel cell and the burner acts as manipulated variables for the controller. The flow rates can be controlled by using appropriate compressors, blowers, and valves, which can also be mathematically represented by ODE models. For this particular case, the split ratio of the exhaust gas to the heat recovery unit and heat exchangers can also act as a manipulated variable. The load and flow temperatures act as disturbances for the system. The detailed design of the controllers has been provided in chapters 4, 5 and 6.

3.7.1 Fuel And Air Heat Exchangers

Two heat exchangers have been used for preheating fuel and air in the fuel cell system. Both heat exchangers are assumed to be counter-current double pipe heat exchangers. A portion of hot stream, which is the exhaust gas from burner is fed into the outer pipe and the cold stream is fed into the inner tube counter-currently. Assuming that the heat exchanger operates at constant pressure (a mild assumption), the general thermal model of the heat exchanger can be expressed as follows,

$$\rho C_p A \frac{\partial T}{\partial t} = -\rho C_p v A \frac{\partial T}{\partial z} + \pi D Q \tag{3.51}$$

where, ρ is the gas density, C_p is the heat capacity of the gas at constant pressure, A is the cross-sectional area, Q is the heat transfer rate per unit area based on the heat transfer area πD.

Since the heat exchanger model as expressed in eqn. (3.51) is a partial differential equation, it is not a control relevant model. The model is thus converted into a set of

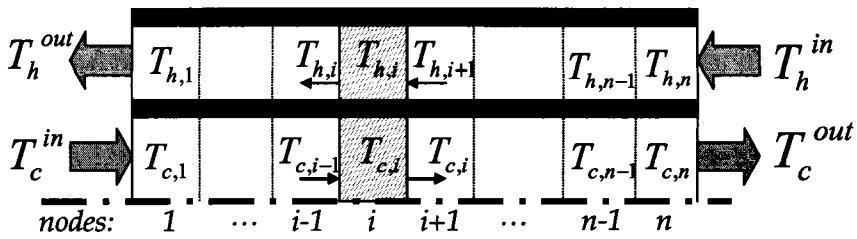

Figure 3.4: Heat exchanger divided into n nodes along the length

ordinary differential equations by dividing the heat exchanger into n nodes along the flow direction as shown in fig. 3.4. It is assumed that each node acts as a continuous stirred tank heater so that the temperature inside each node is same as the exit temperature of the gas of that particular node. Then energy balance of i-th node for the tube (cold gas) and shell (hot gas) can be written as,

Tube:

$$\rho_c C_{pc} A_{cx} \frac{dT_c(i)}{dt} = -\rho_c C_{pc} v_c A_{cx} \frac{T_c(i) - T_c(i-1)}{\Delta z} + \pi D_0 U_0 (T_h(i) - T_c(i)) \tag{3.52}$$

Shell:

$$\rho_h C_{ph} A_{hx} \frac{dT_h(i)}{dt} = -\rho_h C_{ph} v_h A_{hx} \frac{T_h(i+1) - T_h(i)}{\Delta z} - \pi D_0 U_0 (T_h(i) - T_c(i)) \tag{3.53}$$

Here, subscripts 'c' and 'h' stand for the cold side and hot side energy balance; A_{cx} and A_{hx} stand for the cold and hot side flow cross-sectional area; Δz is the length of each node; D_0 is the outer diameter of the tube and U_0[1] is the overall heat transfer coefficient based on D_0. The total number of ordinary differential equations for the lumped heat exchanger model in this case is $2n$.

3.7.2 Reformer

Preheated methane from the fuel heat exchanger and a separate stream of steam are fed into the reformer where endothermic reaction takes place between CH_4 and H_2O.

[1] $U_0 = (\frac{r_0}{r_i h_i} + \frac{r_0 \ln(r_0/r_i)}{k_w} + \frac{1}{h_i})^{-1}$

Reforming reaction:

$$CH_4 + H_2O \rightarrow CO + 3H_2, \qquad \Delta\hat{H}^{\circ}_R = 206.1\ KJ/mol \tag{3.54}$$

If the reforming reaction rate is expressed by $\dot{r}_R$, then material balance for the reactant and product components are,

$$\dot{n}^{out}_{CH_4} = \dot{n}^{in}_{CH_4} - \dot{r}_R \tag{3.55}$$

$$\dot{n}_{H_2O} = \dot{n}^{in}_{H_2O} - \dot{r}_R \tag{3.56}$$

$$\dot{n}_{CO} = \dot{r}_R \tag{3.57}$$

$$\dot{n}_{H_2} = 3\dot{r}_R \tag{3.58}$$

where,

$$\dot{r}_R = k_0 P_{CH4} \exp\big(-\frac{E_A}{RT_R}\big).A_{RX}\ mol/s \tag{3.59}$$

$$k_0 = 4274\ mol/m^2.s.bar \tag{3.60}$$

$$E_A = 82\ KJ/mol \tag{3.61}$$

The mixture of CO and H_2O then take part in the reversible exothermic shift reaction to produce more hydrogen.

Water-gas shift reaction:

$$CO + H_2O \rightleftharpoons CO_2 + H_2, \qquad \Delta\hat{H}^{\circ}_S = -41.15\ KJ/mol \tag{3.62}$$

If the extent of reaction and equilibrium constant for the above reaction are expressed by ξ and K_S respectively, then the material balance for the reactant and product components are,

$$\dot{n}^{out}_{H_2} = \dot{n}_{H_2} + \xi \tag{3.63}$$

$$\dot{n}^{out}_{CO_2} = \xi \tag{3.64}$$

$$\dot{n}^{out}_{CO} = \dot{n}_{CO} - \xi \tag{3.65}$$

$$\dot{n}^{out}_{H_2O} = \dot{n}_{H_2O} - \xi \tag{3.66}$$

and,

$$K_S(T_R) = \frac{\xi(\dot{n}_{H_2} + \xi)}{(\dot{n}_{CO} - \xi)(\dot{n}_{H_2O} - \xi)} \tag{3.67}$$

The equilibrium constant K_S can be expressed as a function of temperature (Bove et al. [16]),

$$K_s(T_R) = \exp\Big(\frac{5693.5}{T_R} + 1.077\ln T_R + 5.44\times 10^{-4}T_R - 1.125\times 10^{-7}T_R^2 - \frac{49170}{T_R^2} - 13.148\Big) \quad (3.68)$$

Now that K_S is known, the extent of reaction can be calculated by solving eqn. (3.67). The energy balance around the reformer can then be written as,

$$\rho V_R C_p \frac{dT_R}{dt} = \dot{n}^{in}_{CH_4}\int_{T_{ref}}^{T^{in}_{CH_4}} C_{p,CH_4}(T)dT + \dot{n}^{in}_{H_2O}\int_{T_{ref}}^{T^{in}_{H_2O}} C_{p,H_2O}(T)dT - \sum \dot{n}^{out}_i \int_{T_{ref}}^{T_R} C_{p,i}(T)dT + r_R\Delta\hat{H}^{\circ}_R + \xi\Delta\hat{H}^{\circ}_S \quad (3.69)$$

where, T_R is the reformer operating temperature.

3.7.3 Burner

The unreacted fuel and air from the fuel cell is then combusted together for heat recovery. In this stage, it is important to supply additional oxygen so that all the unreacted fuel from fuel cell can be consumed. This is done by directly feeding the burner with another air stream. This also gives an additional degree of freedom for the controller to maintain system temperature within operating range. The underlying assumptions for building the burner model is given below:

- Enough O_2 is supplied so that all depleted gas from the fuel cell can be consumed
- Ideal gas mixing inside the burner chamber so that the exit temperature of the burner is same as the inside temperature
- Burner operates at constant pressure

Energy balance around the burner,

$$\rho V_B \bar{C}_p \frac{dT_B}{dt} = \sum \dot{n}_{iF}^{in} \int_{T_{ref}}^{T_F} C_{p,i}(T)dT + \sum \dot{n}_{iA}^{in} \int_{T_{ref}}^{T_A} C_{p,i}(T)dT - \sum \dot{n}_{iB}^{out} \int_{T_{ref}}^{T_B} C_{p,i}(T)dT - \dot{n}_{H_2}^{in} \Delta \hat{H}_{r,H_2}^{\circ} - \dot{n}_{CH_4}^{in} \Delta \hat{H}_{r,CH_4}^{\circ} - \dot{n}_{CO}^{in} \Delta \hat{H}_{r,CO}^{\circ} \quad (3.70)$$

where, T_B is the burner temperature; subscripts 'F', 'A' and 'B' stand for fuel, air, and burner respectively; the specific heat $\bar{C}_p$ and the density ρ are also calculated empirically at each computational instance.

3.8 Simulation Result

The lumped and detailed models deduced in section 3.4 and section 3.5 can be used for simulating fuel cell behavior under different operating conditions. By considering reforming reaction kinetics, it can also be extended to include internal reforming and thus be used to simulate SOFC behavior with natural gas as fuel. Since these models comprise a set of nonlinear ODEs, they can also be used to design model-based controller.

The objective of this work is to synthesize the SOFC cell model with that of BOPs to form a control relevant dynamic model in system level. The synthesis is by no means a simple assembly of the existing models. For example, in order for the system to be controllable, additional component with the associated differential equation is needed to avoid the sudden drop of voltage due to step change of load. In addition, to make the complex system model control relevant, many component models including the cell model have to be re-established. However, the model parameters needed to be populated from experimental and/or literature data for simulation and controller design. Most of these data are extracted from (Braun [19], Padulles et al. [108], Perry et al. [111], Sedghisigarchi and Feliachi [122], Fuel Cell Handbook, Edition 7 [134]). Some model parameters are not available and thus have been estimated empirically within sensible limits. The parameters of the balance of plant components can be estimated based on the capacity of the respective units using engineering

Table 3.1: Model parameters

Parameter	Value	Unit
Number of cells, N_0	384	
Cell area, A_c	100	cm^2
K_{H_2}	8.43×10^{-4}	kmol/atm.s
K_{H_2O}	2.81×10^{-4}	kmol/atm.s
K_{O_2}	2.52×10^{-3}	kmol/atm.s
$\tau^*_{H_2}$	26.1	s
$\tau^*_{H_2O}$	78.3	s
$\tau^*_{O_2}$	2.91	s
T^*	1000	°C
Constant resistance, r_0	0.126	Ω
Resistance slope, α	-2870	
Electrode thickness, h_e	0.25	mm
Interconnector thickness, h_i	1.5	mm
Electrode density, ρ_e	6.6	gm/cm^3
Interconnector density, ρ_i	6.11	gm/cm^3
Specific heat, $\bar{C}_{pe}, \bar{C}_{pi}, \bar{C}_{ps}$	0.4	J/gm.K
Heat of reaction, $\Delta\hat{H}^\circ_r$	-0.2418×10^9	J/kmol
Emissivity, $\epsilon_a, \epsilon_c, \epsilon_i$	0.9	

design practice. In this work, the key parameters are estimated iteratively so that the operating conditions can be met at steady state. Table 3.8 and table 3.2 contain the parameters of a planar SOFC stack made from 384 cells connected in series and the parameters of a SOFC system.

3.8.1 Fuel Cell

The lumped and detailed models are used to generate power-current, voltage-current and temperature-current steady state curves for a fixed 85% fuel utilization[2] and excess oxygen flow ratio of 4 times stoichiometric value. The inlet temperatures of fuel and air were kept constant at 700 $°C$. The simulations were done using MATLAB 7.0 by considering the ohmic loss in order to to compare the results with species only model described in (Padulles et al. [108]). The existing solvers in MATLAB however can not solve differential algebraic equation (DAE) of DAE index greater than 1. Thus the exit temperatures of fuel and air gases in the detail model have been calculated using the ODEs [eqn. (3.35), eqn. (3.40)] instead of the algebraic equations expressed

[2]Fuel utilization, $U_f = \dot{n}^r_{H_2}/\dot{n}^{in}_{H_2}$

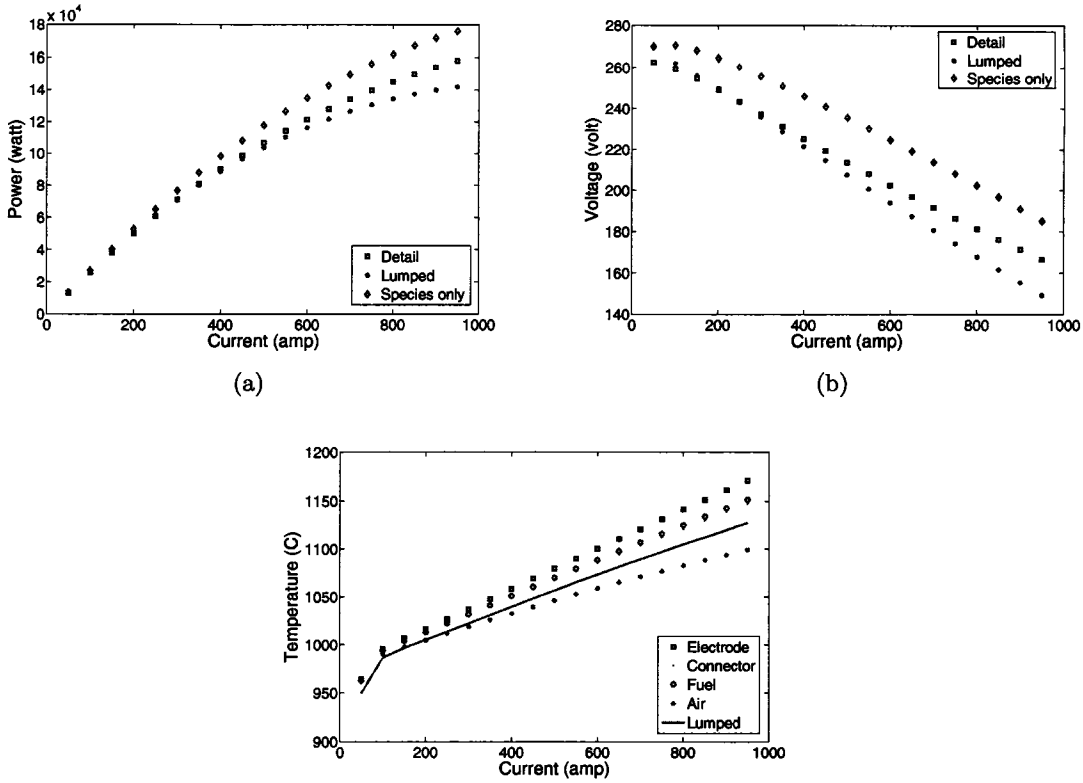

Figure 3.5: (a) Power-current, (b) voltage-current and (c) temperature-current steady state curve for planer SOFC

by eqn. (3.39) and eqn. (3.43) respectively.

Fig. 3.5(a) and fig. 3.5(b) show the steady state power and voltage output from the lumped, detail and species-only dynamic models. Here, the operating temperature of the species-only dynamic model (Padulles et al. [108]) is assumed to be 900 $^{\circ}C$. From the figures, it is evident that the power and voltage predictions from the proposed models are comparable whereas the species-only dynamic model predicts higher cell terminal power and voltage. In fact, the stack voltage and power predicted by the species-only model depends on the cell operating temperature, which is dependent on the fuel and air inlet temperature as well as the demand current. Thus instead of being constant, it varies with operating conditions and thus the assumption of constant fuel cell temperature is not valid.

The stack temperature from the lumped model and the temperatures of electrode,

interconnector, depleted fuel and air gases are shown in fig. 3.5(c). From the figure it is seen that with increase in current load fuel cell operating temperature increases. It is also to be noted that the difference in exit temperatures of fuel and air gases increases with increase in current load, which are different from the uniform cell temperature of the lumped model. Since stack voltage is a function of the fuel cell temperature, the output stack voltage from the fuel cell described by the lumped and detail model also differs at higher demand current as shown in fig. 3.5(b).

Simulations were also conducted to compare the transient responses of the fuel cell described by the lumped and detail models. The transient response of the fuel cell in terms of fuel cell stack voltage and cell temperature has been investigated by changing the current loads, fuel and air flow rates as well as their inlet temperatures (fig. 3.6 to fig. 3.10). The transient response of fuel cell stack voltage and cell temperature expressed by the models due to an increase in current load from 500 *amp* to 600 *amp* is shown in fig. 3.6. Here fuel and O_2 flow rates are kept constant at 5 mol/s and 10 mol/s respectively. The inlet temperatures of fuel and air however are 700 $^{\circ}C$ for fig. 3.6(a) to fig. 3.6(b), 800 $^{\circ}C$ for fig. 3.6(c) to fig. 3.6(d), and 1000 $^{\circ}C$ for fig. 3.6(e) to fig. 3.6(f).

From the simulation results, it is noticed that the dynamic behavior of the fuel cell stack voltage is greatly dependent on the inlet temperatures of fuel and air entering the fuel cell. For all the cases, there is a sudden drop in the voltage associated with the step increase in the load. This sudden voltage drop comes from the ohmic loss term $r(T)I$ in the expression of stack voltage eqn. (3.15). However since the fuel cell stack temperature, T_s, in the lumped model and electrode temperature, T_e, in the detailed model are function of the current load, they also increase with an increase in the load (fig. 3.6(b), fig. 3.6(d), fig. 3.6(f)). The increase in the cell temperature is associated with a decrease of both internal resistance, $r(T)$ in the ohmic loss term and the standard electrode potential, ΔE_0 as shown in eqn. (3.19) and eqn. (3.17) respectively. Thus, there is a net gain or loss in the stack voltage depending on the magnitude of ohmic loss and standard electrode potential. For low fuel and air inlet temperatures (700 $^{\circ}C$), there is a net gain of stack voltage from the initial drop (fig. 3.6(a)). However, as the inlet temperatures of fuel and air are increased, the gain

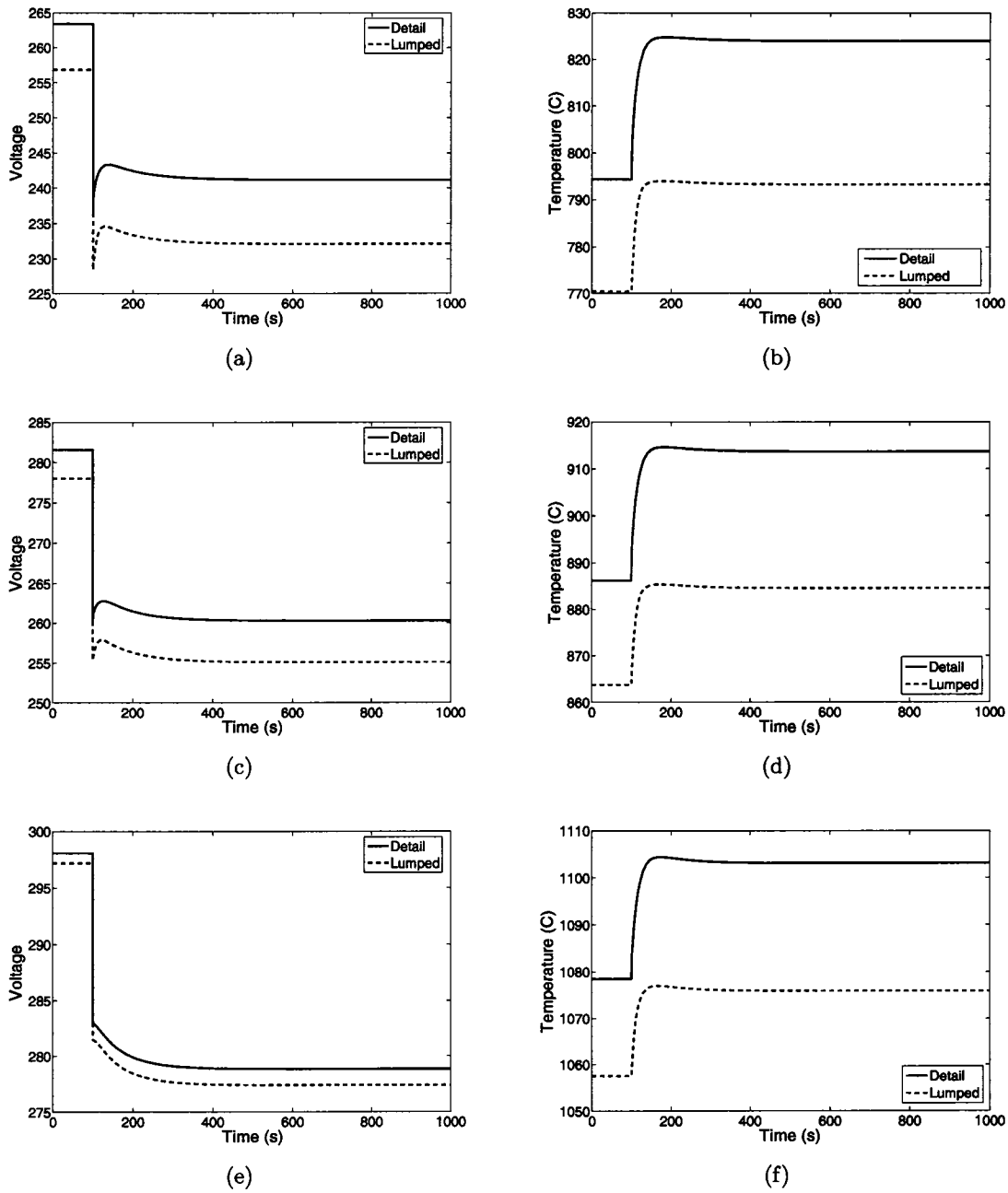

Figure 3.6: Transient responses of voltage, power and temperature due to a load change of 500 *amp* to 600 *amp*; Here, $\dot{n}_{H_2} = 5\ mol/s$, $\dot{n}_{O_2} = 10\ mol/s$; T^{in}_{fuel} and T^{in}_{air} are 700 $^{\circ}C$, 800 $^{\circ}C$ and 1000 $^{\circ}C$ for fig. 3.6(a) to fig. 3.6(b), fig. 3.6(c) to fig. 3.6(d), and fig. 3.6(e) to fig. 3.6(f) respectively

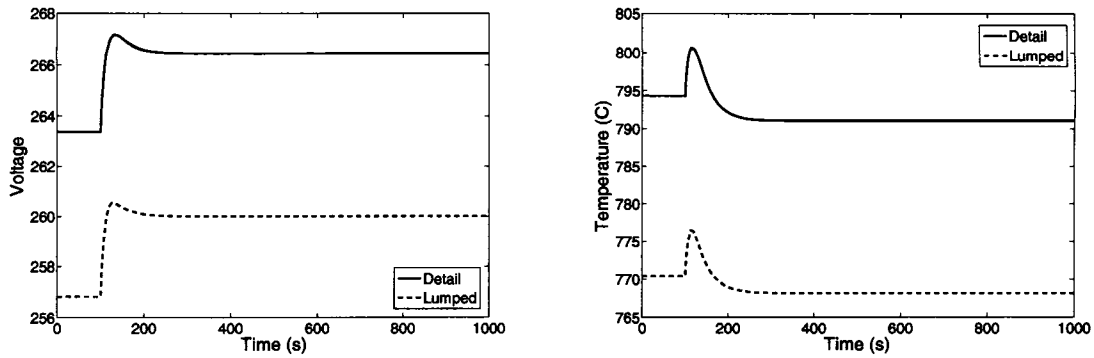

(a) (b)

Figure 3.7: Transient responses of (a) voltage and (b) temperature due to a change in hydrogen flow rate from 5 mol/s to 6 mol/s; Here, $\dot{n}_{O_2} = 10\ mol/s$; T^{in}_{fuel} and T^{in}_{air} are 700 $°C$.

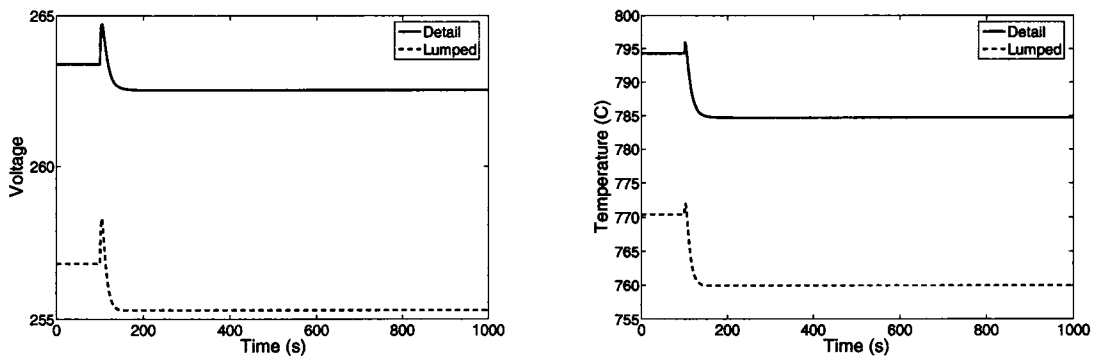

(a) (b)

Figure 3.8: Transient responses of (a) voltage and (b) temperature due to a oxygen flow rate change of 10 mol/s to 12 mol/s; Here, $\dot{n}_{H_2} = 5\ mol/s$; T^{in}_{fuel} and T^{in}_{air} are 700 $°C$.

of voltage from the initial drop by decrease in the ohmic resistance is overshadowed by the decrease in the standard electrode potential. This behavior results in the gradual decreasing of the stack voltage from the initial voltage drop as shown in fig. 3.6(c) and fig. 3.6(e).

The transient behavior of the fuel cell in terms of voltage and cell temperature for a step change in the fuel flow rate, $\dot{n}_{H_2}$, from 5 mol/s to 6 mol/s is shown in fig. 3.7. The current load I, O_2 flow rate $\dot{n}_{O_2}$, and the inlet temperature of fuel and air are kept constant at 500 amp, 10 mol/s, and 700 $°C$ respectively. Fig. 3.8, fig. 3.9 and fig. 3.10 show the transient responses for a step change in O_2 flow rate from 10 mol/s to 12 mol/s, and step changes in the inlet temperature of fuel and air from 700 $°C$

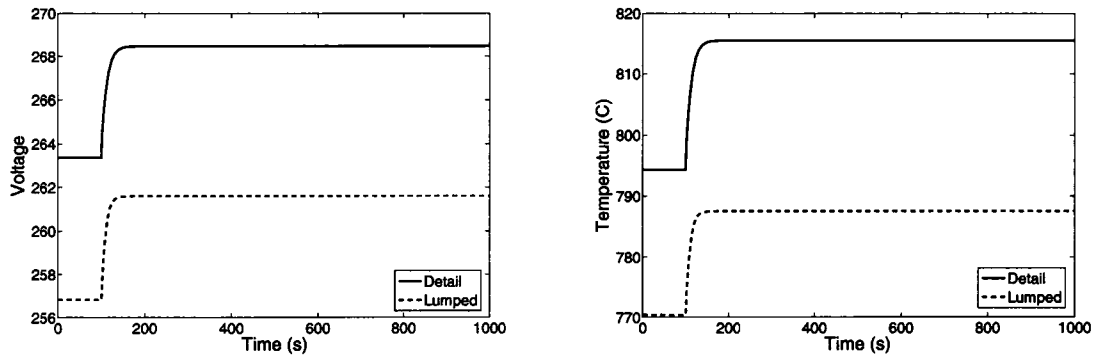

(a) (b)

Figure 3.9: Transient responses of (a) voltage and (b) temperature due to temperature change of fuel from 700 C to 900 C; Here, $\dot{n}_{H_2} = 5\ mol/s$, $\dot{n}_{O_2} = 10\ mol/s$; Current load is 500 amp and T_{air}^{in} is kept constant at 700 $°C$.

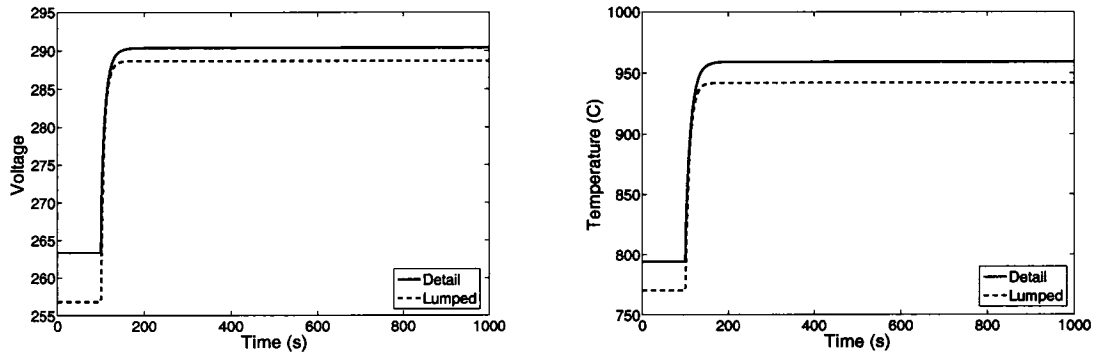

(a) (b)

Figure 3.10: Transient responses of (a) voltage and (b) temperature due to temperature change of air from 700 $°C$ to 900 $°C$; Here, $\dot{n}_{H_2} = 5\ mol/s$, $\dot{n}_{O_2} = 10\ mol/s$; Current load is 500 amp and T_{fuel}^{in} is kept constant at 700 $°C$.

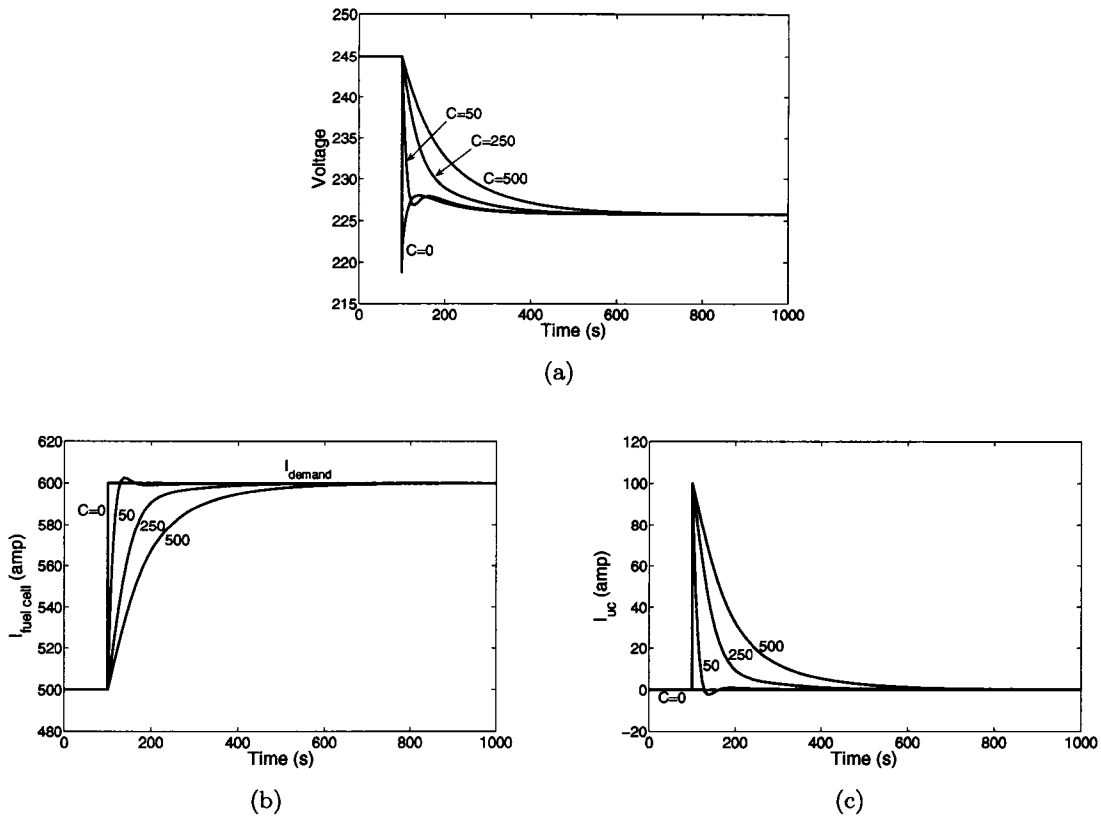

Figure 3.11: (a) Voltage response of SOFC connected in parallel with a capacitor; Demand current sharing by (b) the fuel cell and (c) the capacitor

to 900 $^{\circ}C$ respectively.

3.8.2 Fuel Cell With Capacitor

For a stand-alone SOFC, the voltage drops suddenly when the load was increased from 500 *amp* to 600 *amp* [see fig. 3.7]. On the other hand, when the fuel cell is connected in parallel with a capacitor, the combined system behaves as a first order system. As the capacitance of the capacitor is increased from 0 $farad$ to 500 $farad$ for the combined system, the load sharing capability of the capacitor increases [fig. 3.11(b), fig. 3.11(c)] and the sharp decline in the voltage is smoothed out [fig. 3.11(a)]. In other words, the capacitor works like a filter for the demand current. The final steady-state stack voltages for all the cases are same which is evident from eqn. (3.50). From the simulation, it is evident that a capacitor of 50 $farad$ capacitance is sufficient for our SOFC system.

Table 3.2: Balance of plant parameters

Air Heat Exchanger:
$D_{i,tube} = 0.20\ m$, $D_{o,tube} = 0.205\ m$, $D_{i,shell} = 0.40\ m$, $L = 10\ m$
Fuel Heat Exchanger:
$D_{i,tube} = 0.05\ m$, $D_{o,tube} = 0.055\ m$, $D_{i,shell} = 0.10\ m$, $L = 200\ m$
Reformer:
Reaction area, $A_{RX} = 1000\ m^2$ Reformer Volume, $V_R = 10\ m^3$
Burner:
Burner volume, $V_B = 1\ m^3$

3.8.3 Fuel Cell System

The fuel cell system described in the previous section is simulated for a demand current change of 500 to 600 amp keeping all other input flow rates and disturbances constant. The balance of plant parameters, used in the simulation, are designed so that operating constraints are met and are presented in table 3.2. The dynamic response of the fuel cell system in terms of stack voltage and different component temperatures is shown in fig. 3.12. Since the stack voltage of the fuel cell system is dependent on the input flow rates and temperatures, the prediction of voltage is not straightforward. For example, for this case increase in demand current is associated with increase in the fuel and air inlet temperature of the fuel cell as well as increase in hydrogen production rate and decrease in steam out of the reformer. But since partial pressures are not only a function of the corresponding flow rates, but function of temperatures as well, the partial pressures of H_2 and H_2O decreased and increased respectively resulting in additional loss in the stack voltage.

For an increase in the methane flow rate, the stack voltage from the fuel cell system increases due to increase and decrease in the hydrogen and steam partial pressures respectively as shown in fig. 3.13. Here, the hydrogen production from reformer increases as well as the reformer temperature, fuel cell inlet flow temperatures and burner exhaust temperature. The increase in hydrogen flow rate increases the partial pressure, which finally results in the increase of stack voltage.

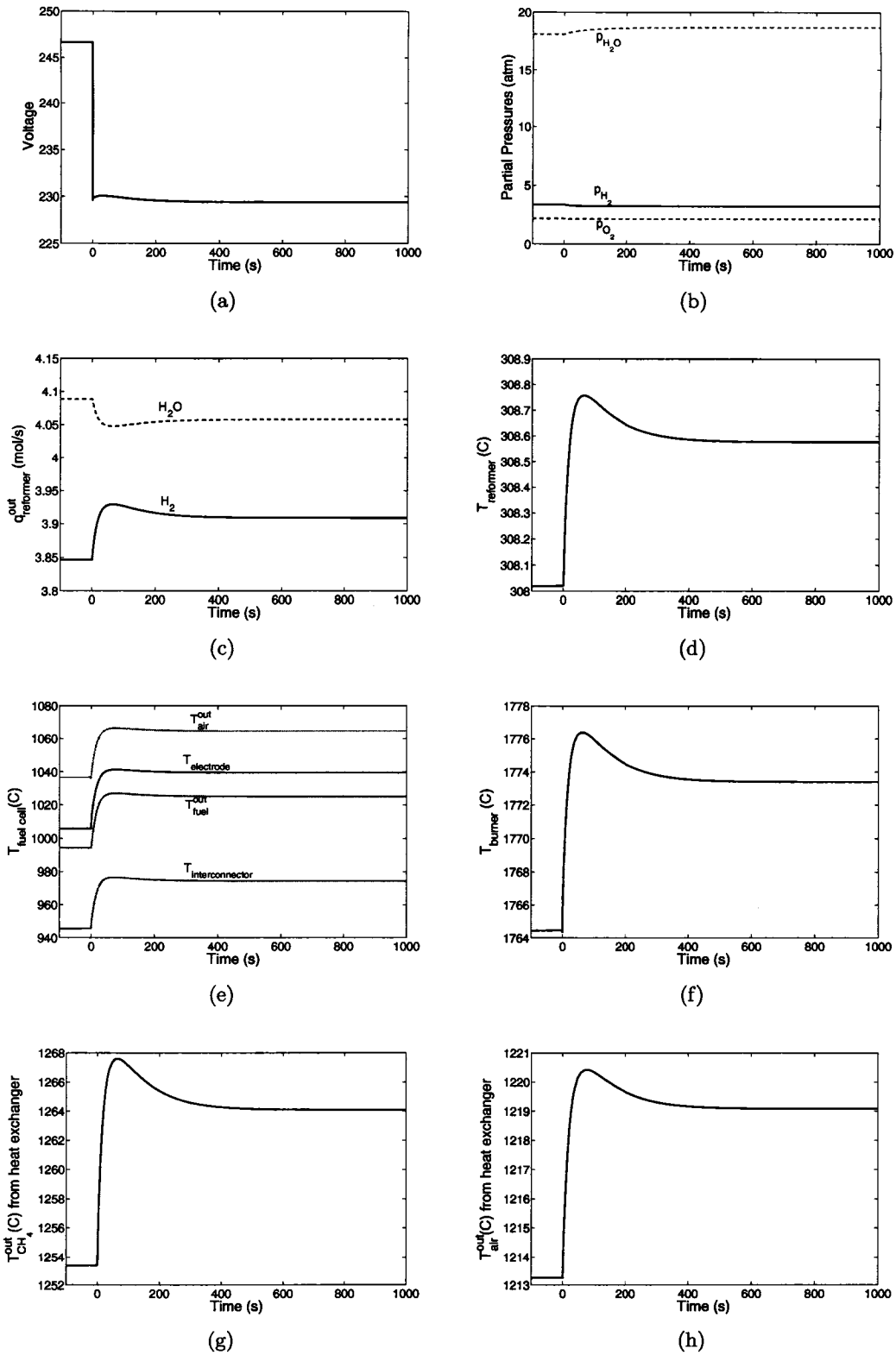

Figure 3.12: Transient responses of fuel cell system due to load change from 500 to 550 amp; Here, $\dot{n}_{CH_4} = 3\ mol/s$, $\dot{n}_{O_2} = 6\ mol/s$, $\dot{n}_{H_2O} = 6\ mol/s$, $\dot{n}_{O_2,burner} = 10\ mol/s$; Inlet temperature of the fuel and airs are 25 $°C$ and $T_{H_2O} = 150\ °C$.

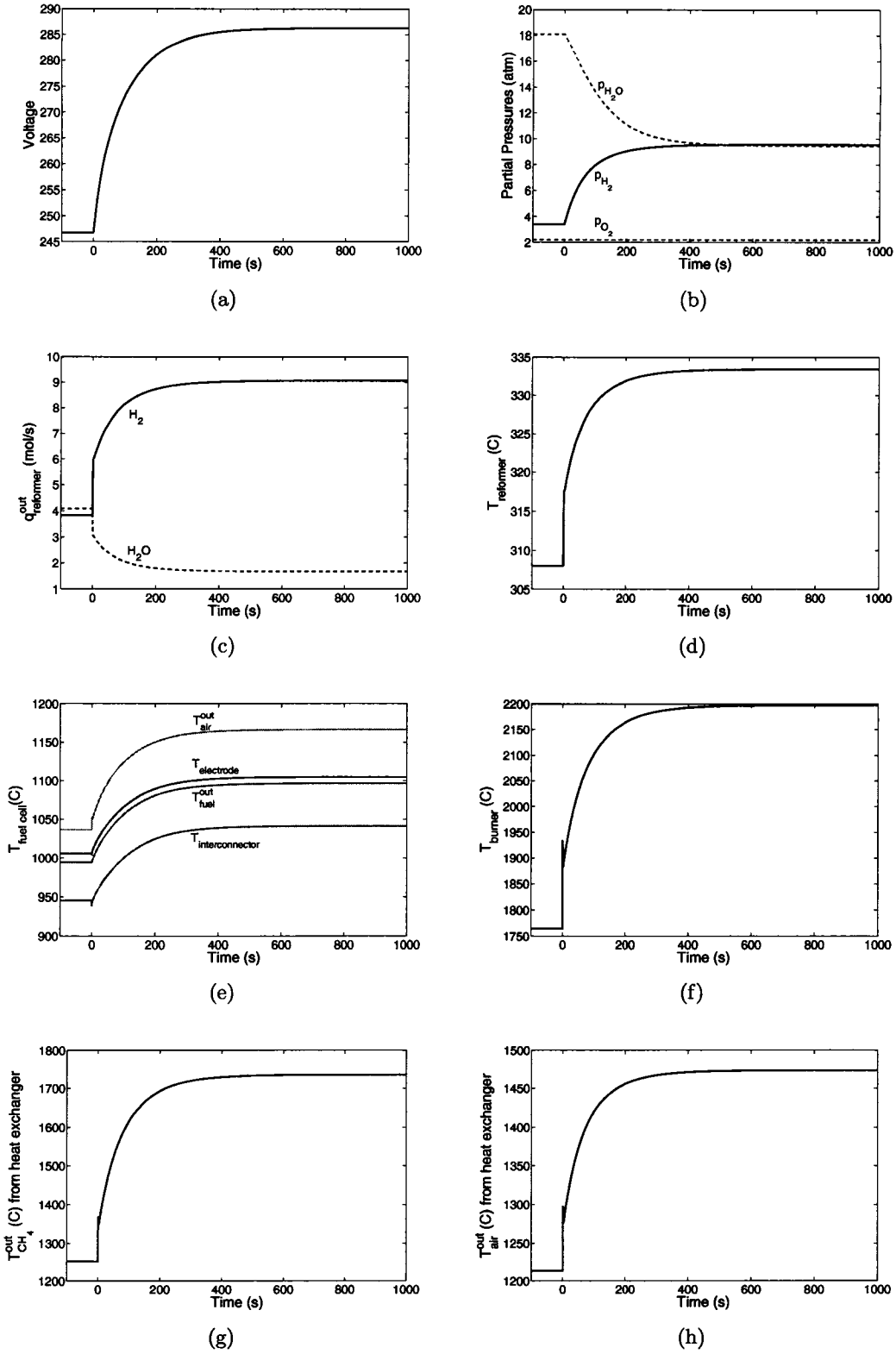

Figure 3.13: Transient responses of fuel cell system due to change in $\dot{n}_{CH_4} = 3mol/s$ from 3 to 4 mol/s; Here, current load $I = 500\ amp$, $\dot{n}_{O_2} = 6\ mol/s$, $\dot{n}_{H_2O} = 6\ mol/s$, $\dot{n}_{O_2,burner} = 10\ mol/s$; Inlet temperature of the fuel and airs are 25 $°C$ and $T_{H_2O} = 150\ °C$.

3.9 Conclusion

The main objective of this work has been to develop control relevant model of the fuel cell system so that it can be used to design model-based controller. For this purpose two sets of comparable models, lumped and detail model both represented by zero-dimensional nonlinear ODEs, have been developed. Simplified thermal models of system components have also been provided. The advantage of using capacitor in parallel with the fuel cell is discussed with appropriate formulation and simulations. Simulations are conducted for both of the models and entire system to compare steady state and dynamic behavior. From the simulations as well as the understanding of the model, the following conclusions can be drawn.

- SOFC temperature is an important variable in predicting stack voltage and thus species-only model, which assumes constant operating temperature, is not valid unless an isothermal operation is enforced by other heating device.
- Stack voltage, current load and cell temperature are internally dependent. Change of one affects all of the others. This is more prominent in the fuel cell system with after-burner and heat exchangers. Change in fuel flow rate or demand current or even inlet temperature leads to a change in hydrogen flow rate in the fuel cell from the reformer. This leads to a change in fuel cell temperature and stack voltage. The unreacted fuel then goes to after-burner and heat exchangers, which again affects the temperatures of the reformer and fuel cell. The effect of flow rates or disturbances thus propagates through the entire fuel cell system.
- Steady state stack voltage, power and temperature of the fuel cell predicted by both of the models are comparable at lower current load. But as the current load is increased they differ in magnitude and thus it is important to choose appropriate model depending on the control objective. For example, for designing a controller where computational power is limited, the lumped model can be used. However, for evaluating performance of the fuel cell, detail model is preferable. In addition, the lumped model considers that the exit temperature of depleted fuel and air are same. In fact, these temperatures differ widely for

higher current load and thus detail model should be used, especially when the fuel cell is connected to an after-burner for recovering energy.

- At lower operating temperature, the stack voltage initially drops suddenly for a step up of the current load and then gains some voltage due to decrease in ohmic loss. But, at higher operating temperature, the gain in stack voltage due to lower ohmic loss is overshadowed by the decrease in standard electrode potential resulting in more decrease in the stack voltage from the initial drop. Thus, fuel cell may show different dynamic characteristics depending on the operating region.

- For the detail model, exit temperatures of fuel and air can be expressed either by ODEs or by DAEs. However solving DAE may require additional computational power and may not be helpful if the model is used to compute future control actions using optimization algorithms such as MPC. Thus in our simulation ODEs have been used to simulation exit temperature of fuel and air out of fuel cell.

- Capacitor can act as an auxiliary power source for the fuel cell system soothing out sudden change in the voltage. It can help in two ways: first, electrical equipments will be less prone to damage due to the sudden fluctuation in the voltage, and second, any controller responsible for maintaining the voltage will be able to bring the voltage to its reference value more easily.

- It is to be noticed that the lumped and detail models are described by non-linear ODEs with 4 and 7 states respectively. Hence, during simulation the performance of lumped and detail models do not differ much in terms of computational time. For example, the cpu time to simulate the transient response for load change described by lumped and detail models are 0.6409 and 0.8012 seconds respectively [fig. 3.6(a) and fig. 3.6(b)]. The computation, in this particular case, is performed using Dell Inspiron 600M with 2.00 GHz Intel Pentium Mobile processor and 1 GB RAM running Microsoft Windows XP Home as an operating system. For control purpose, which is not presented in this chapter, the cpu time for linear controller (e.g., linear MPC) does not differ much. But

for nonlinear controller obviously the computational time is higher based on the sample time to estimate unmeasured states using nonlinear state estimator (e.g., unscented Kalman filter) and the sample time of the controller (e.g., nonlinear MPC). With the advent of cheap computational power and dedicated servers for applying advanced controller, this is not a problem anymore.

Overall, the developed models can predict all the important variables of the fuel cell system. In addition, the models being zero-dimensional in nature can be used for designing model based controller such as linear and nonlinear MPC. Moreover, since usually all the states are not measurable, the same model can be used for estimating states using state estimator such as extended Kalman filter (EKF) or, unscented Kalman filter (UKF).

Chapter 4

Nonlinear Model Predictive Control (NMPC)

4.1 Introduction

In the past few years, linear model predictive control has been well investigated by both the academicians and the industry due to its capability to handle multivariate problems easily. Ease of implementation and ability of handling process constraints have given it a boost over other controllers. However due to a heavy computational load, nonlinear model predictive control has got less attention than its linear counterpart in practice. In addition, the unavailability of the nonlinear models, complexity in the discretization of the nonlinear model, and estimation of states impose certain limitations on the application of the nonlinear model predictive control. Recent advance in cheap computational power however has lifted that constraint and generated a vast interest in the application of NMPC.

Model predictive control (MPC) can be described as a finite-horizon open-loop optimal control problem that accounts for the plant model and constraints. Nonlinear model predictive control, which is a generalized version of the well-established linear model predictive control, can handle process nonlinearities and constraints. Based on measured or, estimated states at current time, it predicts future states and required control actions such that a predefined objective function is minimized over a predefined horizon. It then applies the first of the calculated control actions and proceeds

to the next time step and repeats the entire procedure again.

Since MPC uses current states in the objective function, the solution in fact utilizes feedback data at every time step. Thus, MPC algorithm converges to a closed loop strategy. This moving horizon feature of MPC, which distinguishes itself from the classical controllers, is illustrated in fig. 4.1. The following section gives a brief mathematical overview of model predictive control.

4.1.1 General Principle

Let the model be represented by,

$$x(k+1) = f(x(k), u(k), w(k)) \tag{4.1}$$

$$y(k) = g(x(k), w(k)) \tag{4.2}$$

where, x, u and w are the states, inputs and disturbances respectively. The state and output functions f and g can take both linear and nonlinear form. Then the MPC formulation can be written as finding a set of future control actions $u(k|k), u(k+1|k), ..., u(k+M-1|k)$ by solving the following optimization problem,

$$\min_{u(k|k),u(k+1|k),\cdots,u(k+M-1|k)} J = \sum_{i=1}^{N} [\|\hat{x}(k+i|k) - x_{ref}\|_Q^2 + \|u(k+i|k) - u_{ref}\|_R^2 + \|\Delta u(k+i|k)\|_S^2] \tag{4.3}$$

subject to,

$$\hat{x}(k+1) = f(\hat{x}(k), u(k), w(k)) \tag{4.4}$$

$$y_{min} \leq \hat{y}_i \leq y_{max} \tag{4.5}$$

$$u_{min} \leq u_{k+i|k} \leq u_{max} \tag{4.6}$$

$$\Delta u_{min} \leq \Delta u_{k+i|k} \leq \Delta u_{max} \tag{4.7}$$

where, N is the prediction horizon over which future states are calculated and the objective function is minimized; M is the control horizon over which control actions are optimized. For feasibility $M \leq N$ and after the control horizon M, the control actions are kept constant *i.e.*, $\Delta u(k+i|k) = 0$ for $i \geq M$. In general, the second

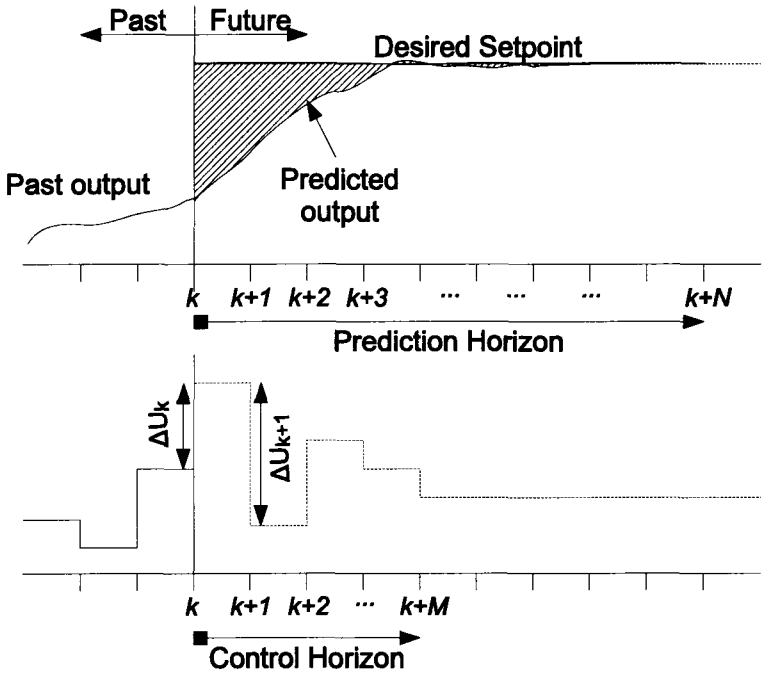

Figure 4.1: Moving horizon concept of general MPC

term in the objective function is dropped for better flexibility in the control action. Now, once the control actions are known, only $u(k|k)$ is implemented and the same procedure is repeated at time $k+1$.

In the above MPC formulation, the objective function is quadratic in nature and therefore, if the state equation [eqn. (4.4)] is linear then it is called linear MPC, otherwise nonlinear MPC. In addition, if the output equation 4.2 is nonlinear, then the objective function in the MPC formulation can be rewritten as:

$$\min_{u(k|k),u(k+1|k),\cdots,u(k+M-1|k)} J = \sum_{i=1}^{N} [\|g(\hat{x}(k+i|k), w(k)) - y_{ref}\|_Q^2 + \|u(k+i|k) - u_{ref}\|_R^2 + \|\Delta u(k+i|k)\|_S^2] \quad (4.8)$$

The developed models of fuel cell system described in chapter 3 are in continuous-time domain and can be expressed in general form as,

$$\dot{x} = f(x, u, w) \quad (4.9)$$

$$y = g(x, w) \quad (4.10)$$

where, x represents the states describing partial pressures and temperatures of fuel

cell and balance of plant; u represents the flow rates of methane, oxygen, steam, excess oxygen in the burner and splitter ratio respectively; w represents the external disturbances including the current demand load on the system and temperatures of the input flow rates; output y is the stack voltage.

Since the developed models are continuous in nature, applying linear and nonlinear MPC to fuel cell system requires additional step. For linear MPC, the models have been converted to discrete linear models around a nominal operating point by using MATLAB so that they take the following form:

$$x(k+1) = Ax(k) + B_u u(k) + B_w w(k) \tag{4.11}$$

$$y(k) = Cx(k) + D_w w(k) \tag{4.12}$$

Linear MPC will be applied to both of the SOFC models by using MATLAB MPC toolbox. The simulation results are given in section 6.5.1.

For nonlinear MPC, the models can be discretized using finite element methods such as the orthogonal collocation method, Galerkin method or, flatness based technique. In this work, the orthogonal collocation method will be employed to convert nonlinear continuous models to a set of nonlinear algebraic equations. The converted model however does not take the explicit discrete nonlinear form as expressed by eqn. (4.4).

A detailed description of the orthogonal collocation method is given in section 4.2. Since not all the states are measurable, they need to be estimated from the input-output data. Several methods exist for estimating states for both linear and nonlinear systems. A brief discussion on different types of state estimators is given in section 4.3. The simulation results of nonlinear MPC are given in section 6.5.2.

4.1.2 General Tuning Guideline of MPC

The choices of prediction horizon, control horizon and weights have a major effect on the performance of MPC. Clever choice of tuning parameters can ensure nominal stability and robustness. A poor choice, on the other hand, may lead to instability, higher computational load, and infeasible solution. For example, unusually high pre-

diction horizon is in favor of stability of the system, but requires higher computational power.

Tuning guidelines for linear MPC are abundant in literature (Clarke and Scattolini [29], Lee and Yu [82], Oshima et al. [105], Shridhar and Cooper [124, 125]). Table 1 of (Shridhar and Cooper [125]) provides a good guideline for tuning DMC which can be easily applied to linear MPC. However, due to broad class of nonlinear systems, there is no hard and bound rule for tuning nonlinear MPC (Henson and Seborg [55]). Based on the guideline of linear MPC, the following rules can be used for tuning of NMPC :

- **Sampling Interval:** The sampling interval should be small enough to adequately capture the dynamics of the system. As a general rule of thumb, the sampling period should lie between 0.05 and 0.1 of the settling time. For multivariate system, the sampling interval should be calculated based on the fast dynamics of all the process variables.
- **Prediction Horizon:** As a general rule of thumb, the prediction horizon should be able to see the steady state point of the process to ensure the stability of the system. A prediction horizon smaller than a critical length may lead to an unstable closed loop system. A longer prediction horizon, on the other hand, may produce faster response, as well as more aggressive control action and overshoot. Implementation of MPC with longer prediction horizon is also restricted by the availability of computation power. For multivariate system, the prediction horizon should be based on the slow dynamics of all the process variables. For complex nonlinear system, such as convective loop reactor showing chaotic behavior, the selection of prediction horizon can be particularly difficult. For such cases, prediction horizon should be chosen based on experience and rigorous simulation of the process.
- **Control Horizon:** In general, small control horizon relative to the prediction horizon results in a control that is less sensitive to disturbances and produces less aggressive response. A control horizon of 3-5 often suffices for most cases.

For multivariate case, the control horizon should reflect the dynamics of the slowest subsystem.

- **Weights:** Weight on controlled variables and penalty on manipulated variables should be chosen based on the order of the magnitudes of the variables and the objective. For example, for equally important process output variables, the weights should be chosen to scale the process variables to a similar magnitude. Once the magnitude has been set to the same scale, more weight can be applied based on the importance of the variables objective.

- **Discretization method:** For a nonlinear continuous time model, one of the important steps is to approximate the model to a discrete one that best serves the purpose. In this work, the orthogonal collocation method has been used for discretization of continuous models. The choice of number of interior collocation points has a profound effect on the approximation of the true system, which again varies from system to system. For our case, three interior collocation points have been sufficient to approximate the system.

- **State Estimator:** Based on the complexity of the system a linear Kalman filter, Extended Kalman filter (EKF), Unscented Kalman filter (UKF) or, different variants of particle filters can be used to estimate unmeasured states. For complex nonlinear system, such as the SOFC system, implementation of EKF may become cumbersome and also may not produce the intended accuracy. In our case, UKF has been applied together with MPC to estimate unmeasured states and control the system.

4.2 Discretization of Models: Orthogonal Collocation Method

In the orthogonal collocation method, any function can be approximated by an interpolating polynomials with nodes located at the roots of a set of orthogonal polynomials (Burns [20], Finlayson [43], Henson and Seborg [55], Lapidus and Seinfeld

[77], Stephens [129], Villadsen and Michelsen [140]) i.e.,

$$y(x) = \sum_{i=1}^{N+2} b_i P_{i-1}(x) \tag{4.13}$$

where

$$P_m(x) = \sum_{j=0}^{m} c_j x^j \tag{4.14}$$

is the m-th polynomial such that

$$\int_a^b W(x) P_k(x) P_m(x) dx = 0 \qquad k = 0, 1, 2, \ldots, m-1$$

Here, the polynomial m has m-roots in the interval $[a, b]$ and thus users do not need

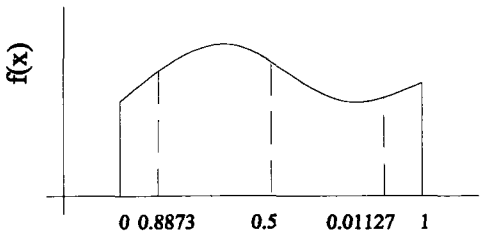

Figure 4.2: Approximation of a function by three point collocation on one step ahead prediction

to pick the collocation points arbitrarily. This has advantage over the conventional collocation method where there is a good chance of poor choice of these nodes by inexperienced users and thus poor approximation of the function. Typically, the integration range is taken as 0 to 1 to generalize the problem. Equation (4.13) and (4.14) can be combined to give

$$y(x_j) = \sum_{i=1}^{N+2} d_i x_j^{i-1} \tag{4.15}$$

Derivatives can also be approximated by orthogonal polynomials and finally we get the following forms

$$\frac{dy}{dx}(x_j) = \sum_{i=1}^{N+2} d_i (i-1) x_j^{i-2} \tag{4.16}$$

$$\frac{d^2y}{dx^2}(x_j) = \sum_{i=1}^{N+2} d_i (i-1)(i-2) x_j^{i-3} \tag{4.17}$$

In matrix notation,

$$y = \mathbf{Qd} \qquad \frac{dy}{dx} = \mathbf{Cd} \qquad \frac{d^2y}{dx^2} = \mathbf{Dd}$$

where

$$\begin{aligned} Q_{ji} &= x_j^{i-1} \\ C_{ji} &= (i-1)x_j^{i-2} \\ D_{ji} &= (i-1)(i-2)x_j^{i-3} \end{aligned} \tag{4.18}$$

Therefore,

$$\frac{dy}{dx} = \mathbf{CQ^{-1}}y \equiv \mathbf{A}y \tag{4.19}$$

$$\frac{d^2y}{dx^2} = \mathbf{DQ^{-1}}y \equiv \mathbf{B}y \tag{4.20}$$

For our case, the three-point collocation method is used. With the choice of the nodes, the continuous model expressed by eqn. (4.9) can be represented by the following nonlinear algebraic equation,

$$A_0 X = F(X, u) \tag{4.21}$$

where,

$$X = \begin{bmatrix} x_{1,1} & x_{1,2} & \cdots & x_{1,n} \\ x_{2,1} & x_{2,2} & \cdots & x_{2,n} \\ x_{3,1} & x_{3,2} & \cdots & x_{3,n} \\ x_{4,1} & x_{4,2} & \cdots & x_{4,n} \\ x_{5,1} & x_{5,2} & \cdots & x_{5,n} \end{bmatrix} \qquad F(X,u) = \begin{bmatrix} x_{init}^T \\ f^T(x_{2,*}^T, u, t_2) \\ f^T(x_{3,*}^T, u, t_3) \\ f^T(x_{4,*}^T, u, t_4) \\ f^T(x_{5,*}^T, u, t_5) \end{bmatrix} \tag{4.22}$$

The collocation points and the A-matrices are given in the table (4.1) and table (4.2). Here, A_0 matrix can be calculated by knowing the location of the nodal points x_j and replacing first row of A by [1 0 0 0 0] to account for the initial conditions.

The matrices given in table (4.2) for different collocation points are for interval $[0, 1]$. To account for sampling interval other than one, the following change is made to convert the dynamic constraint into algebraic constraint:

$$A_0 X = \Delta t' F(X, u) \tag{4.23}$$

Table 4.1: Polynomial roots and the weighting functions

N	x_j	W_j
1	0.50000 00000	0.66666 66667
2	0.21332 48654	0.50000 00000
	0.78867 51346	0.50000 00000
3	0.11270 16654	0.27777 77778
	0.50000 00000	0.44444 44444
	0.88729 83346	0.27777 77778

Table 4.2: Matrices for orthogonal collocation found from eq. (4.18)

N	A
1	$\begin{pmatrix} -3 & 4 & -1 \\ -1 & 0 & 1 \\ 1 & -4 & 3 \end{pmatrix}$
2	$\begin{pmatrix} -7 & 8.196 & -2.196 & 1 \\ -2.732 & 1.732 & 1.732 & -0.7321 \\ 0.7321 & -1.732 & -1.732 & 2.732 \\ -1 & 2.196 & -8.196 & 7 \end{pmatrix}$
3	$\begin{pmatrix} -13 & 14.79 & -2.67 & 1.88 & -1 \\ -5.32 & 3.87 & 2.07 & -1.29 & 0.68 \\ 1.5 & -3.23 & 0 & 3.23 & -1.5 \\ -0.68 & 1.29 & -2.07 & -3.87 & 5.32 \\ 1 & -1.88 & 2.67 & -14.79 & 13 \end{pmatrix}$

The above formulation can be used to convert nonlinear continuous time dynamic equation to a nonlinear algebraic equation and thus can be used in MPC as an equality constraint with prediction horizon 1. For prediction horizon greater than one, the orthogonal collocation approximation is extended by employing the following formulation,

$$\tilde{A}\tilde{X} = \tilde{F}(\tilde{X}, U) \tag{4.24}$$

where,

$$\tilde{X} = \begin{bmatrix} x_{1,1} & x_{1,2} & \cdots & x_{1,n} \\ x_{2,1} & x_{2,2} & \cdots & x_{2,n} \\ \vdots & \vdots & & \vdots \\ x_{4N,1} & x_{4N,2} & \cdots & x_{4N,n} \\ x_{4N+1,1} & x_{4N+1,2} & \cdots & x_{4N+1,n} \end{bmatrix}$$

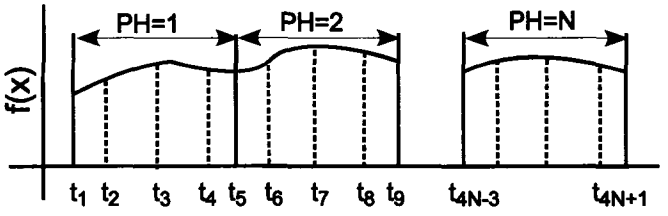

Figure 4.3: Polynomial approximation of a function using three point collocation method with prediction horizon > 1

and,

$$\tilde{F}(\tilde{X},U) = \begin{bmatrix} x_{init}^T \\ f^T(x_{2,*}^T, u, t_2) \\ \vdots \\ f^T(x_{4N,*}^T, u, t_{4N}) \\ f^T(x_{4N+1,*}^T, u, t_{4N+1}) \end{bmatrix}$$

Here, the first subscript denotes the collocation points in the time interval and the second means state. $\tilde{A}$ is defined by combining A and A_0 as follows,

$$\tilde{A} = \begin{bmatrix} A_0 & & & & \\ & A & & & \\ & & A & & \\ & & & \ddots & \\ & & & & A \\ & & & & & A \end{bmatrix} \tag{4.25}$$

Now that the model has been converted from continuous-time nonlinear ODEs to a set of discrete algebraic equations, it can be used in the MPC formulation as an equality constraints in eqn. (4.4):

$$\min_{u(k|k),u(k+1|k),\cdots,u(k+M-1|k)} J = \sum_{i=1}^{N} [\|\hat{x}(k+i|k) - x_{ref}\|_Q^2 + \|u(k+i|k) - u_{ref}\|_R^2 + \|\Delta u(k+i|k)\|_S^2] \tag{4.26}$$

subject to,

$$\tilde{A}\tilde{X} = \tilde{F}(\tilde{X},U) \tag{4.27}$$

$$y_{min} \leq \hat{y}_i \leq y_{max} \tag{4.28}$$

$$u_{min} \leq u_{k+i|k} \leq u_{max} \tag{4.29}$$

$$\Delta u_{min} \leq \Delta u_{k+i|k} \leq \Delta u_{max} \tag{4.30}$$

4.3 State Estimation

The model predictive control algorithm, described in the previous section, requires a continuous or discrete dynamic model equation and a true knowledge of the current states to predict future outputs. However, in most situations not all the states are measurable and thus estimation of the states is required based on the current measurement of the available states and the input-output data.

Estimation of states of linear systems can be done by least square estimation technique, recursive estimation, Luenberger and moving horizon state estimator, or Kalman filter. States of nonlinear systems can be estimated by using extended Kalman filter, extended Luenberger observer and moving horizon estimator, or by emerging unscented Kalman filter (UKF) and different variants of particle filter. Of them EKF is the mostly widely used nonlinear state estimator, which utilizes the state estimating power of Kalman filter by linearizing the nonlinear functions around the predicted values (Anderson and Moore [8]). EKF has certain disadvantages though. First, it can estimate the states accurately upto first order only and second, it requires Jacobean of the nonlinear model. Since finding Jacobian of complex models like the one developed for the SOFC can be time consuming, implementation of EKF can be a problem. Thus UKF has been used here as a derivative free and more accurate alternative to EKF (Haykin [54], Julier [70], Julier et al. [71], Lee [80], Rui and Chen [120], Wan and Merwe [141, 142]). A brief overview of UKF is described in section 4.3.1.

4.3.1 Unscented Kalman Filter (UKF)

The UKF, originally proposed by Julier et al. [71], uses a deterministic sampling approach to capture the mean and covariance using a minimal set of carefully chosen sample points. UKF can capture the posterior mean and covariance of any nonlinear system accurately upto second order whereas EKF can capture these properties upto first order only. The detailed algorithm of UKF can be found in (Julier [70], Julier et al. [71]).

UKF utilizes the power of unscented transformation (UT), which can be used for calculating statistics of a random variable undergoing a nonlinear transformation. The following section describes UT:

Let us consider propagating a random variable x of dimension n, mean $\bar{x}$ and covariance P_{xx} through a nonlinear function $y = f(x)$. Calculation of mean and covariance by linearized EKF, with linearized model $y = Ax$, will produce:

$$\bar{y} = f(\bar{x}) \tag{4.31}$$

$$P_{yy} = A^T P_{xx} A \tag{4.32}$$

which does not give the true nonlinear propagation of the statistics. Thus instead of directly propagating the mean and covariance through the nonlinear function, a set of points, named sigma points, are chosen such that their sample mean and sample covariance are $\bar{x}$ and P_{xx}. The nonlinear mapping is then applied to the sigma points to yield a cloud of mapped nonlinear points. Weighted mean and covariance of these mapped sigma points will then give a true resemblance of the actual statistics.

The sigma points, χ_i of dimension $2n+1$ and their weights W_i are formed according to the following:

$$\chi_0 = \bar{x} \qquad W_0 = \kappa/(n+\kappa) \tag{4.33}$$

$$\chi_i = \bar{x} + (\sqrt{(n+\kappa)P_{xx}})_{i=1:n} \qquad W_i = 1/2(n+\kappa) \tag{4.34}$$

$$\chi_{i+n} = \bar{x} - (\sqrt{(n+\kappa)P_{xx}})_{i=1:n} \qquad W_{i+n} = 1/2(n+\kappa) \tag{4.35}$$

where κ is a tuning parameter, $(\sqrt{(n+\kappa)P_{xx}})_i$ is the i-th row or column of the matrix square root of $(n+\kappa)P_{xx}$ and W_i is the weight.

These sigma points are then propagated through the nonlinear function to yield the set of transformed sigma points:

$$\mathcal{Y}_i = f(\chi_i) \tag{4.36}$$

The mean and covariance can then be approximated as the weighted sample mean

and covariance:

$$\bar{y} \approx \sum_{i=0}^{2n} W_i \mathcal{Y}_i \tag{4.37}$$

$$P_{yy} \approx \sum_{i=0}^{2n} W_i (\mathcal{Y}_i - \bar{y})(\mathcal{Y}_i - \bar{y})^T \tag{4.38}$$

The unscented Kalman filter is a straightforward application of UT for recursive estimation of states. The state estimation steps of UKF are described below [see Julier [70] for a detailed description]:

1. Initialize:

   Create augmented state vector of dimension $n^a = n+q$ by including the process and noise terms:

   $$x^a(k) = [x(k), v(k)]^T \tag{4.39}$$

   The process model can then be written in terms of the augmented state vector x^a as $x(k+1) = f(x^a(k), u(k), k)$. The mean and covariance of the augmented state vector can be expressed as:

   $$\hat{x}^a(k|k) = \begin{bmatrix} \hat{x}(k|k) \\ 0_{q\times 1} \end{bmatrix}$$

   and,

   $$P^a(k|k) = \begin{bmatrix} P(k|k) & P_{xv}(k|k) \\ P_{xv}(k|k) & Q(k) \end{bmatrix} \tag{4.40}$$

2. Calculate sigma points:

   $$\chi_i^a(k|k) = [\hat{x}_i^a(k|k) \quad \hat{x}_i^a(k|k) \pm (\sqrt{(n^a+\kappa)P^a(k|k)})_i] \tag{4.41}$$

3. Transform the sigma points:

   $$\chi_i(k+1|k) = f(\chi_i^a(k|k), u(k), k) \tag{4.42}$$

4. Compute predicted mean and covariance:

$$\hat{x}(k+1|k) = \sum_{i=0}^{2n^a} W_i \chi_i^a(k+1|k) \tag{4.43}$$

$$P_{xx}(k+1|k) = \sum_{i=0}^{2n^a} W_i(\chi_i(k+1|k) - \hat{x}(k+1|k)) .(\chi_i(k+1|k) - \hat{x}(k+1|k))^T \tag{4.44}$$

5. Predict the measurement:

$$\mathcal{Z}_i(k+1|k) = g(\chi_i(k+1|k), u(k), k) \tag{4.45}$$

$$\hat{z}(k+1|k) = \sum_{i=0}^{2n^a} W_i \mathcal{Z}_i(k+1|k) \tag{4.46}$$

6. Update the measurement:

$$P_{zz} = \sum_{i=0}^{2n^a} W_i(\mathcal{Z}_i(k+1|k) - \hat{z}(k+1|k)) .(\mathcal{Z}_i(k+1|k) - \hat{z}(k+1|k))^T \tag{4.47}$$

$$P_{xz} = \sum_{i=0}^{2n^a} W_i(\chi_i(k+1|k) - \hat{x}(k+1|k)) .(\mathcal{Z}_i(k+1|k) - \hat{z}(k+1|k))^T \tag{4.48}$$

$$\mathcal{K} = P_{xz} P_{zz}^{-1} \tag{4.49}$$

$$\hat{x}(k+1) = \hat{x}(k+1|k) + \mathcal{K}(z(k+1) - \hat{z}(k+1|k)) \tag{4.50}$$

$$P(k+1|k) = p(k+1|k) - \mathcal{K} P_{zz} \mathcal{K}^T \tag{4.51}$$

UKF[1] has been implemented to validate its state estimation capability, first on convective loop reactor in chapter 5 and then on solid oxide fuel cell system in chapter 6.

4.3.2 Discretization of UKF model

Implementation of UKF however requires discrete model, which can be done by the following methods:

[1]Used source code of Dr. Tim Bailey (`http://www.acfr.usyd.edu.au/people/academic/tbailey/`) as a start point.

- **Backward Approximation** can be used to discretize the model. For complex nonlinear models, it may require very small time step to estimate the states which makes it infeasible to implement.

- **Orthogonal Collocation Method** can be used to express the continuous model as a set of nonlinear algebraic equations [eqn. (4.21)]. The nonlinear equation can then be solved for $\hat{x}(k+1|k)$ by using nonlinear least square regression. This method gives higher accuracy but computational load is also relatively high.

- **MATLAB ODE solver** can simply be used to predict $\hat{x}(t+T_s|t)$.

4.3.3 Tuning of UKF

It is noticed that even though it is fairly easy to implement UKF and the estimated states quickly converge to the true states, it has to be implemented discreetly for successful estimation of the states. Wrong choice of initial state-covariance matrix or discretization method may lead to poor estimation of states. Following are some guidelines that have been used during the implementation of UKF in our simulations:

- The model has to be discrete which can easily be derived by using backward approximation for simple systems. For complex nonlinear models, backward approximation may not be suitable for predicting future value. In that case, continuous models can be used to generate future data by using appropriate ODE solvers with variable time steps. This is in fact discretizing the continuous model numerically to predict future data points. Alternatively, the orthogonal collocation method can be used to express nonlinear ODEs as a set of nonlinear algebraic equations. In this case, the future states can be predicted by solving eqn. (4.21) using nonlinear least square regression. In our simulations, nonlinear ODE solvers have been used to predict future values of the states.

- The choice of initial state-covariance matrix affects the performance of UKF as well. Even though a state-covariance matrix of small magnitude should suffice as an initial condition, it is found from our simulations that sometimes this choice

leads to positive semi-definite state-covariance matrix. To avoid this behavior, a moderately large magnitude state-covariance matrix has been used as an initial condition for our simulations.

- The choice of state transformation parameter κ can lead to positive semi-definite state covariance matrix especially if κ is negative. For our simulations, negative κ has been used to maintain positive denominator in the weighting which leads to this problem. To avoid this problem, state covariance has been estimated around transformed mean $\chi_0(k+1|k)$ instead of the weighted mean $\bar{x}(k+1|k)$, as suggested in Julier et al. [71].

Chapter 5

Application of NMPC: Thermal Convective Loop Reactor

5.1 Introduction

In the previous chapter, theory of nonlinear model predictive control has been discussed. A review of orthogonal collocation technique as a discretization method, and unscented Kalman filter as an estimator has also been done. The objective is to find a suitable controller that can be applied to solid oxide fuel cell system. Before applying these methods, its performance needs to be compared with alternative controllers. For this purpose, a nonlinear process is sought which exhibits complex nonlinear behavior, yet can be represented by fairly simple nonlinear model. Different controllers, including simple to complex linear and nonlinear controllers, can then be tested against nonlinear model predictive controller. Based on the comparison, a suitable controller can be designed for solid oxide fuel cell system.

Thermal convective loop reactor, which is not uncommon in chemical process industries, can be represented by a relatively simple nonlinear dynamic model. Depending on the heating rate, it can show stable, perpetual oscillation, or chaotic behavior. The complex dynamic nature (chaotic behavior) of convective loop reactor has made it a suitable candidate to test different control schemes.

The presence of chaos is very common in physical systems. It is desirable to reduce the

chaos so that system performance can be improved. This can be done in two ways (Ott et al. [106]). First, make some large costly alteration to the system, which completely changes its dynamics to the desired dynamic behavior. Second, improve performance by making small time dependant perturbations in an accessible parameter. In this case, chaotic system holds advantage over other systems in that it can be made stable to any existing orbit without much effort or, alteration to the system.

In this work, we will apply linear and nonlinear control laws and investigate their performance among each other. For this case, it is found that the proportional state feedback control law with setpoint tracking ($u = -k(x_3 - x_{3e})$) exhibits a sufficiently good performance. The proportional constant can be found by stability analysis of linearized model or LQR.

A nonlinear control law similar to the previous structure ($u = (x_1 + x_2)(x_3 - x_{3e})$) gives better result in terms of quick stabilization of the states to the desired setpoints (here, the desired setpoints are the equilibrium points). This controller is equivalent to taking $-k(x) = x_1 + x_2$ and depends a lot on the initial values of the states at the time when the control law is applied. Nonlinear control law based on the backstepping method is also developed here which stabilizes the system but can not bring the states to the desired equilibrium points.

Finally, both linear and nonlinear MPCs are applied to stabilize the system. Nonlinear MPC stabilizes the system very efficiently compared to other linear and nonlinear controller including linear MPC. Results from these simulations are also included for comparison. The organization of this chapter is as follows: first, description of convective loop reactor and its first principle model are provided in section 5.2 and section 5.3 respectively. Stability analysis of the reactor model along with open loop response is then provided in section 5.4. A detail discussion on conventional control, nonlinear control and NMPC, including simulation results are given in 5.6, section 5.7 and section 5.8 respectively - and finally conclusion in section 5.9 to represent findings.

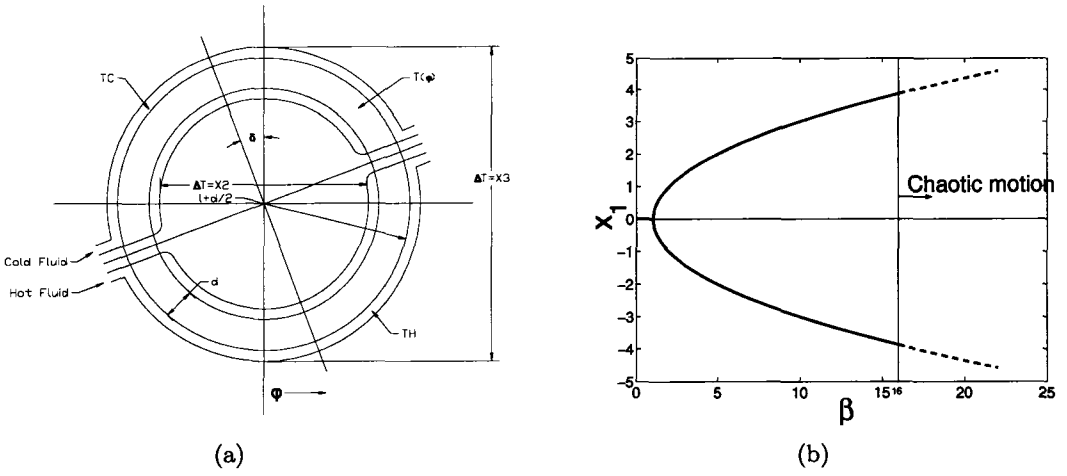

Figure 5.1: a) Schematic description of natural convection loop, b) Bifurcation diagram of the state x_2 vs. β

5.2 Description

Natural convection in a closed loop system consists of a heat source and several sinks positioned above the source. The source and sink are connected by pipe forming at least one closed loop system. The heat is transported from the source to the sink by circulating fluid inside the loop. Unlike the forced convection (as in refrigerator), the heat is transported by natural convection only. Solar heating system and nuclear reactors are example of such system. For a detailed review of closed loop natural convection system, see (Ehrhard and Müller [39], Greif [49], Metrol and Greif [97], Zvirin [149]).

Fig. 5.1(a) shows a schematic diagram of the system. The sink and the source are connected by a circular loop filled with an incompressible fluid, which works as a transporting media of heat from source to sink. The cross section, A of this loop is circular and constant. The lower semicircle of the loop is heated by a hot fluid at a temperature T_H and the upper semicircle is cooled by a coolant at a temperature T_C. The cooling and heating zones are tilted by an angle δ from the symmetric position. If the temperature difference $\Delta T = T_H - T_C$ is increased, the fluid is at first at no motion state. During this stage, heat is transported by conduction only. As the heating rate is increased, steady state convection arises either in clockwise

or counter-clockwise direction. If heating rate is further increased, the steady state convection becomes unstable and shows oscillatory and chaotic motion.

5.3 First Principle Model

Assuming $d << l$, material and energy balance leads to the following equations (Ehrhard and Müller [39]),

$$\begin{aligned}
&\frac{\partial U}{l\partial\varphi} = 0 \\
&\rho_0 \frac{\partial U}{\partial t} = -\frac{\partial p}{l\partial\varphi} - \rho(T) g \sin(\varphi) - f_w \\
&\rho_0 C_p \left\{ \frac{\partial T}{\partial t} + U \frac{\partial T}{l\partial\varphi} \right\} - \lambda \frac{\partial^2 T}{l^2 \partial\varphi^2} \\
&\qquad = h_w [T_w(\varphi(T) - T] + q_w(\varphi)
\end{aligned} \tag{5.1}$$

where

$$f_w = \frac{1}{2}\rho_0 f_{w0} U \tag{5.2a}$$

$$T(\varphi, t) = T_0(t) + \sum_{n=1}^{\infty} \{S_n(t)\sin(n\varphi) + C_n(t)\cos(n\varphi)\} \tag{5.2b}$$

$$Q(\varphi) = Q_0 + \sum_{n=1}^{\infty} \{Q_n \sin(n\varphi) + R_n \cos(n\varphi)\} \tag{5.2c}$$

$$= \frac{1}{\rho_0 C_p} l \{h_w T_w(\varphi) + q_w(\varphi)\} \tag{5.2d}$$

Introducing the dimensionless variables as follows,

$$Time, t' = \frac{h_{w0}}{\rho_0 C_p} t \tag{5.3a}$$

$$x_1 = \frac{\rho_0 C_p}{l h_{w0}} U \tag{5.3b}$$

$$x_2 = \frac{\rho_0 C_p}{h_{w0}} \frac{\gamma g}{f_{w0} l} S_1 \tag{5.3c}$$

$$x_3 = \frac{\rho_0 C_p}{h_{w0}} \frac{\gamma g}{f_{w0} l} \left\{ \frac{\rho_0 C_p}{h_{w0}} R_1 - C1 \right\} \tag{5.3d}$$

where

$$\begin{aligned}
\gamma &= \text{coefficient of thermal expansion} \\
C_p &= \text{specific heat} \\
\rho_0 &= \text{reference density} \\
\lambda &= \text{heat conductivity} \\
g &= \text{acceleration due to gravity} \\
h_w &= \text{heat transfer coefficient} = h_{w0}\left\{1 + K|x_1|^{1/3}\right\}
\end{aligned} \tag{5.4}$$

Neglecting higher order terms in eqn. (5.2),

$$\begin{aligned}
T(\varphi, t) &= T_0(t) + S_1(t)\sin(\varphi) + C_1(t)\cos(\varphi) \\
Q(\varphi) &= Q_0 + Q_1\sin(\varphi) + R_1\cos(\varphi) \\
&= \frac{1}{\rho_0 c_p} l\left\{h_w T_w(\varphi) + q_w(\varphi)\right\}
\end{aligned}$$

and assuming that the heat transfer coefficient h_w is constant *i.e.*, $K = 0$, the parameters S_1, C_1, R_1 are found to be

$$C_1(t) = \frac{T(0°, t) - T(180°, t)}{2} \tag{5.5a}$$

$$S_1(t) = \frac{T(90°, t) - T(270°, t)}{2} \tag{5.5b}$$

$$R_1 = \frac{h_{w0}}{\rho_0 c_p}\frac{T_H - T_C}{2} \tag{5.5c}$$

where T_H and T_C are the temperature of the heating and cooling zone respectively.

Further assuming that there is no tilting between the heating and cooling zone *i.e.*, $\delta = 0$ and there is negligible heat transfer in the direction of the tube axis, the system can be described by the following set of ordinary differential equations:

$$\begin{aligned}
\dot{x}_1 &= \alpha(-x_1 + x_2) \\
\dot{x}_2 &= -x_2 - x_1 x_3 \\
\dot{x}_3 &= x_1 x_2 - x_3 - \beta
\end{aligned} \tag{5.6}$$

where,

$$\alpha = \frac{\rho_0 C_p}{h_{w0}} \frac{f_{w0}}{2} \tag{5.7}$$

$$\beta = \frac{\gamma g}{f_{w0} l} \left(\frac{\rho_0 C_p}{h_{w0}} \right)^2 R_1$$

$$= \frac{\gamma g}{f_{w0} l} \frac{\rho_0 C_p}{h_{w0}} \frac{T_H - T_C}{2} \tag{5.8}$$

Here, α is comparable to the Prandtl number and β is the heating rate which is directly proportional to the temperature difference ΔT and is equivalent to the Rayleigh number. The states x_1, x_2 and x_3 are proportional to the average cross sectional velocity inside the loop, temperature difference along the horizontal direction and temperature difference along the vertical direction. All of the states are measurable and hence available for computation.

5.4 Open Loop Response

In the eqn. (5.6), α stands for Prandtl number and can be assumed constant. The other parameter β stands for Rayleigh number which is proportional to the heating rate. At equilibrium, $\dot{x}_i$'s are zero. Putting these values in eqn. (5.6) and solving them the following two cases arise:

Case a: $\beta \leq 1$ $x_{1e} = x_{2e} = 0$ and $x_{3e} = -\beta$

In this case, the states are globally stable and converge to the equilibrium points irrespective of the initial conditions. The state x_1 i.e., average cross-sectional velocity of the fluid is zero at equilibrium which means that the fluid is at no motion state in this case and heat is transported from the source to the sink by conduction only.

Case b: $\beta > 1$ $x_{1e} = x_{2e} = \pm\sqrt{\beta - 1}$ and $x_{3e} = -1$

In this case, the states have two equilibrium points. The fluid average velocity may be clockwise or counter-clockwise. Heat is transported at this stage by convection. Depending on the value of the parameter β the system may show stable or unstable and chaotic behavior. This is because as heating rate is

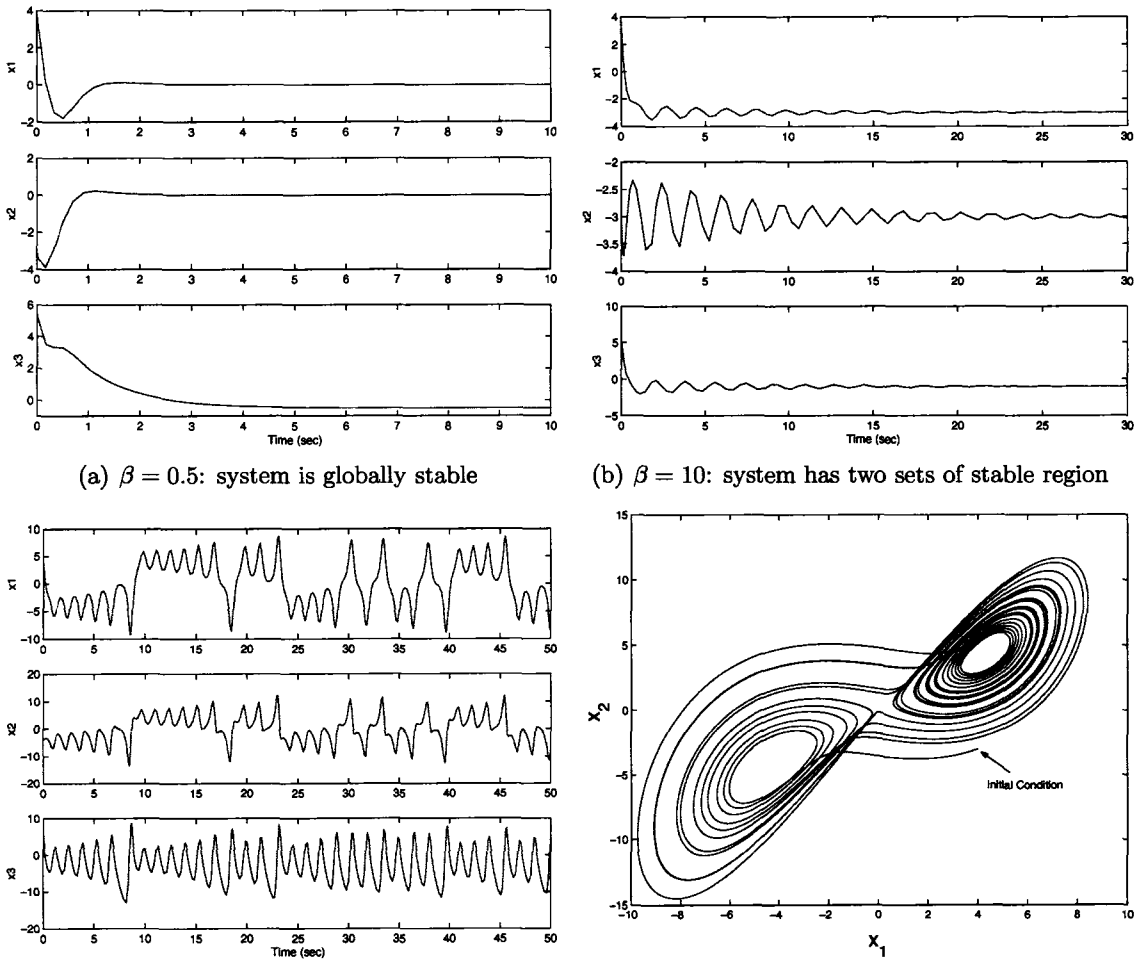

(a) $\beta = 0.5$: system is globally stable

(b) $\beta = 10$: system has two sets of stable region

(c) $\beta = 20$: System is chaotic

(d) x_2 vs. x_1 for $\beta = 20$

Figure 5.2: Open loop response of the system for different β's; Initial conditions of the state variables are $x_{10} = 4.0$, $x_{20} = -3.0$ and $x_{30} = 5.5$, taken arbitrarily

increased fluid velocity is also increased and at higher value of β it becomes locally unstable and jumps from one equilibrium point to another from time to time making the system chaotic.

The different cases are depicted in fig. 5.1(b). The open loop response for different β are given in fig. 5.2(a), fig. 5.2(b), and fig. 5.2(c). These figures show how the system responses to the same initial condition with different β. From fig. 5.2(d), it is obvious that at chaos the system has two different orbits. Solution of x_1 and x_2 remains in this orbit but never becomes stable to any single equilibrium point [see, fig. 5.2(c)]. From the bifurcation diagram, it is obvious that at some critical value of β the system starts showing chaotic behavior. To find out this critical value we need to do stability

analysis of the open loop system:

5.4.1 Stability Analysis

If there is a nonlinear equation

$$\dot{\mathbf{x}} = \mathbf{f}(\mathbf{x})$$

then linearization of the above equation around the equilibrium point leads to the following equation

$$\dot{\mathbf{x}} = \mathbf{A}\mathbf{x}$$

where

$$\mathbf{A} = \begin{bmatrix} \frac{\partial f_1}{\partial x_1} & \cdots & \frac{\partial f_1}{\partial x_n} \\ \vdots & \ddots & \vdots \\ \frac{\partial f_n}{\partial x_1} & \cdots & \frac{\partial f_n}{\partial x_n} \end{bmatrix}$$

is evaluated at equilibrium points. For the system to be stable all the eigenvalues of the matrix $\mathbf{A}$ must have negative real parts. For the convective loop described by eqn. (5.6), the linearized equation becomes

$$\dot{x} = Ax$$

where

$$\begin{aligned} A &= \begin{bmatrix} -\alpha & \alpha & 0 \\ -x_3 & -1 & -x_1 \\ x_2 & x_1 & -1 \end{bmatrix}_{evaluated\ at\ equlibrium} \\ &= \begin{bmatrix} -\alpha & \alpha & 0 \\ 1 & -1 & -\sqrt{\beta-1} \\ \sqrt{\beta-1} & \sqrt{\beta-1} & -1 \end{bmatrix} \end{aligned}$$

Here, the positive equilibrium values of x_1 and x_2 are taken for analysis with $\beta > 1$. Making the real parts of the eigenvalues of the A matrix equal to zero leads to the following relation[1]:

$$\beta_{crit} = \frac{\alpha(\alpha+4)}{\alpha-2}$$

Therefore, if β is greater than this critical value then the system will show chaotic behavior. For example for $\alpha = 4$, the critical value of β is 16 over which the system

[1] All the eigenvalue analysis is done by using Maple V

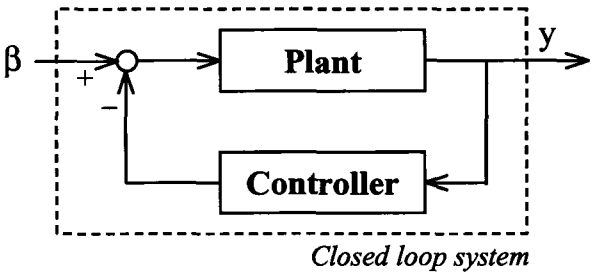

Figure 5.3: Schematic diagram of closed loop system

is chaotic. Notice that the critical value is found by linearization of the nonlinear system. In practice, the transition from stable to chaotic behavior will not happen exactly at this critical value of β. In fact, there is a transition region where the system actually is semi-chaotic meaning that it shows chaotic response initially and after some period the oscillation decays resulting into settling down of the response to one of its stable equilibrium points.

5.5 Controlling Chaos

Unlike linear systems, control of nonlinear and chaotic system is difficult due to the heavy computational duty, which makes nonlinear control infeasible. In addition, when the main target is to keep the operating point steady, it often suffices to linearize the nonlinear system around the operating point and apply linear control law.

In the following sections several methods for controlling chaos in the convective loop is discussed. For a review of different control strategy of chaotic system and bifurcation control see (Abed and Fu [1, 2], Bau and Singer [11], Kim and Abed [73], Lee and Abed [81], Ott et al. [106], Singer et al. [126], Wang and Abed [143]). There are several works on linear feedback control of chaotic system (Wang and Abed [143]). For different well established nonlinear controller design technique see (Khalil [72], Marquez [94], Sastry [121]). The main theme is to set the control action to be a function of some observable state so that it can be calculated and implemented. In case of convective loop, the parameter β (heating rate) is proportional to the temperature difference in the vertical direction which is the state x_3. So the control action , u in the convective loop system

is taken as the deviation of heating rate from its nominal value.

$$\begin{aligned} \dot{x}_1 &= \alpha(-x_1 + x_2) \\ \dot{x}_2 &= -x_2 - x_1 x_3 \\ \dot{x}_3 &= x_1 x_2 - x_3 \underbrace{-\beta + u}_{\text{Total heating rate},U} \end{aligned} \tag{5.9}$$

5.6 PID Control

5.6.1 Proportional Control

For the convective loop system the control action, u in eqn. (5.9) is taken as proportional to the state, x_3 i.e.,

$$u = -kx_3$$

Stability analysis of the closed loop system leads to the following relationship for the linear system

$$\beta = \frac{\alpha(4 + \alpha + 5k + \alpha k + k^2)}{\alpha - k - 2}$$

This means that if the system were linear for $\alpha = 4$, $k = 2$ would be sufficient for stabilizing the system for any value of β. Since the system is highly nonlinear, feedback gain $k = 2$ may not suffice for higher values of β. However for small β, small negative feedback gain suffices to make the system steady [see, fig. 5.4]. However, in this case the system equilibrium points are not the same as that of the open loop system. The equilibrium point of the average cross-sectional velocity is determined by $\pm\sqrt{\beta - k - 1}$ and the final fluid velocity stabilizes at this new equilibrium point instead of open loop equilibrium point $x_{2e} = \pm\sqrt{\beta - 1}$. The heating rate does not remain the same as β, instead it becomes $\beta - u$ where u is a constant value at steady state. This actually changes the heating rate to some extent.

5.6.2 Setpoint Tracking

This is same as the proportional controller but the control law is defined by

$$u = -k(x_3 - x_{3e}) \tag{5.10}$$

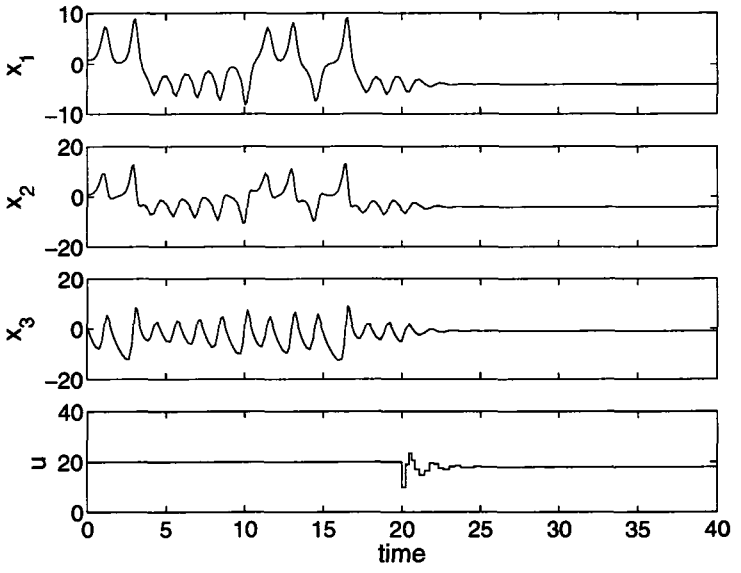

Figure 5.4: Closed loop response with proportional controller for $k = 2$ for system with $\beta = 20$. The control is applied at time, $t = 20$

where x_{3e} is the open loop equilibrium point of the state, x_3. The closed loop equilibrium point is same as the open loop equilibrium and the steady state value of the control action, u is zero. This is given in the fig. 5.5.

5.7 Nonlinear Control

5.7.1 Lyaponov Stability Criterion

The main difficulties with designing a controller based on Lyaponov stability criterion is in choosing the energy function. For this case the best candidate for the energy function should be of the form:

$$V(x) = mx_3^2 + nx_1^2, \qquad m, n > 0 \tag{5.11}$$

because of the fact that heating rate is proportional to x_3 (vertical temperature difference) and energy loss due to friction is proportional to x_1^2. Here, m and n are two proportional constants, which depend on the parameters used during conversion from PDE to ODE of the system model. But this energy function is positive semi-definite. Nevertheless using this "wrong" energy function, and Taylor series approximation to approximate $\sqrt{\beta - u + 1} = f(u) \approx a + bu$ where a and b are linearization constants

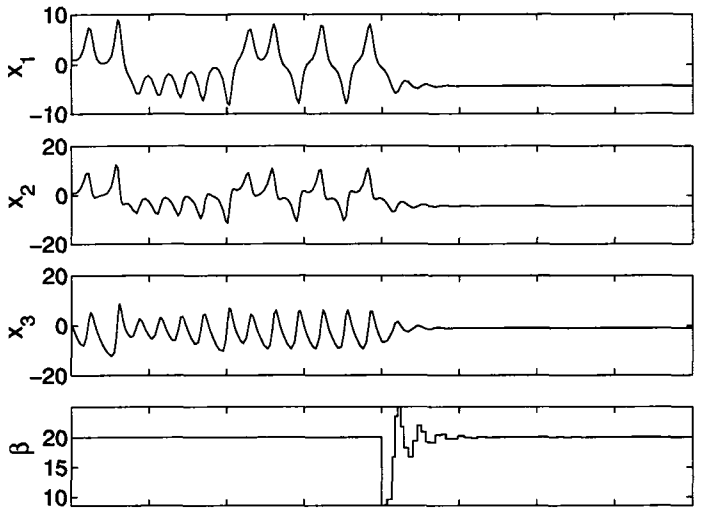

Figure 5.5: Feed back control with reference point tracking; here, $k = 2$ for system with $\beta = 20$

and truncating constant terms in the final control law which accounts for lowering the heating rate (similar things are discussed in section 5.7.2), we can finally come up with the following control law:

$$u = (x_1 + x_2)(x_3 + 1) \tag{5.12}$$

Surprisingly this control gives better stabilizing effect than that developed by back-stepping method as will be discussed next. But it depends greatly on the initial condition. Simulation result is given in fig. 5.6. As we said earlier that this control law is based on the "wrong" energy function $V(x)$. So why does it work then? The answer is that with so many assumption during the development of the control law, the control law u is not associated with the positive semi-definite energy function any more. Rather it belongs to some other unknown energy function. If we take an energy function of the form $V(z) = \frac{1}{2}(z_1^2 + z_2^2 + z_3^2)$ where z_i's are the transformed states for $\dot{z} = f(z)$ with equilibrium points at the origin, it can be shown that $\dot{V}$ is negative provided that the open loop system is bounded (which is true for this case without any external excitation even in unstable chaotic region).

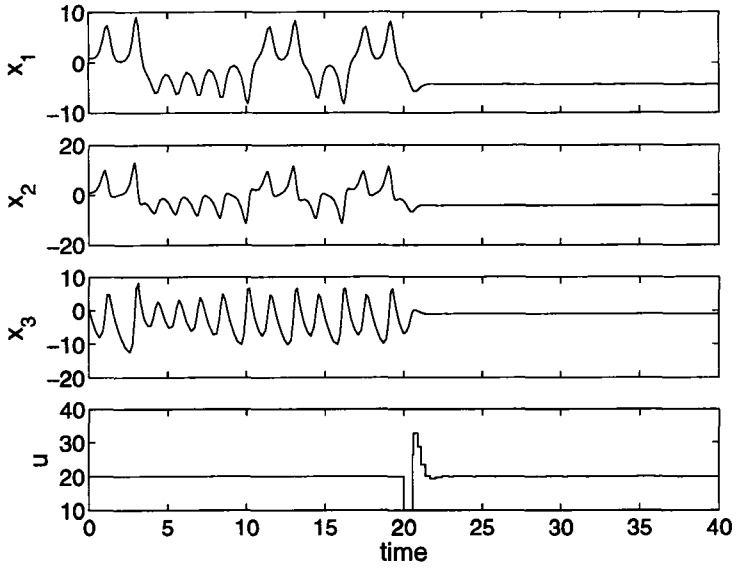

Figure 5.6: Feed back control for system with $\beta = 20$: Lyaponov Stability Criterion

5.7.2 Back Stepping Method

The system

$$\dot{x}_1 = \alpha(-x_1 + x_2) \tag{5.13}$$

$$\dot{x}_2 = -x_2 - x_1 x_3 \tag{5.14}$$

$$\dot{x}_3 = x_1 x_2 - x_3 - \beta + u \tag{5.15}$$

can be written in the following strict feedback system form:

$$\dot{x}_1 = f(x_1) + g(x_1)\xi_1 \tag{5.16}$$

$$\dot{\xi}_1 = f_1(x_1, \xi_1) + g_1(x_1, \xi_1)\xi_2 \tag{5.17}$$

$$\dot{\xi}_2 = f_2(x_1, \xi_1, \xi_2) + g_2(x_1, \xi_1, \xi_2)u \tag{5.18}$$

where

$$f(x_1) = -\alpha x_1 \qquad g(x_1) = \alpha \qquad \xi_1 = x_2$$

$$f_1(x_1, \xi_1) = -x_2 \qquad g_1(x_1, \xi_1) = -x_1 \qquad \xi_2 = x_3$$

$$f_2(x_1, \xi_1, \xi_2) = x_1 x_2 - x_3 - \beta \qquad g_2(x_1, \xi_1, \xi_2) = 1$$

The first target is to stabilize the x_1 sub-system defined by eqn. (5.16). Let the Lyaponov function be $V_1 = \frac{1}{2}x_1^2$. Then

$$\begin{aligned}\dot{v}_1 &= \frac{\partial V_1}{\partial x_1}\dot{x}_1 \\ &= x_1(-\alpha x_1 + \alpha x_2) \\ &= -\alpha x_1^2 + \alpha x_1 x_2\end{aligned}$$

Let us take the control law to be

$$x_2 = \phi(x_1) = -ax_1 \qquad a \in \Re^+ \tag{5.19}$$

We have included an unknown parameter a in the control law $\phi(x_1)$ which we will see in the later section increases degree of freedom and will help removing singularity in the final control law. For better flexibility and more degree of freedom we could also take the following control law instead:

$$x_2 = \phi(x_1) = -ax_1^{2b+1} \qquad a > 0, b \geq 0 \tag{5.20}$$

But the addition of parameter b increases complexity in the final control law and so we assumed $b = 0$ for now. If necessary we can always come back and assume it to be nonzero.

With this control law [eqn. (5.19)] the sub-system eqn. (5.16) becomes:

$$\dot{x}_1 = -(a+1)\alpha x_1 \tag{5.21}$$

and the derivative of the energy function V becomes:

$$\dot{V} = -(a+1)\alpha x_1^2, \qquad a, \alpha > 0 \tag{5.22}$$

which is negative definite. Hence the sub-system is globally asymptotically stable. The energy function for the next sub-system eqn. (5.17) can be written as:

$$\begin{aligned}V_2 &= V_1 + \frac{1}{2}[\xi_1 - \phi]^2 \\ &= \frac{1}{2}x_1^2 + \frac{1}{2}[x_2 + ax_1]^2\end{aligned} \tag{5.23}$$

Then the control law that makes the derivative of V_2 negative definite can be expressed as

$$\begin{aligned} x_3 = \phi_1 &= \frac{1}{g_1}\left[\frac{\partial \phi}{\partial x_1}(f + g\xi_1) - \frac{\partial V_1}{\partial x_1}g - k_1(\xi_1 - \phi) - f_1\right] \\ &= -\frac{1}{x_1}\left[-a(-\alpha x_1 + \alpha x_2) - x_1.\alpha - k_1(x_2 + a x_1) + x_2\right] \\ &= -(a\alpha - \alpha - k_1 a) + (a\alpha + k_1 - 1)\frac{x_2}{x_1}, \quad k_1 > 0 \end{aligned} \tag{5.24}$$

Similarly the final control law can be written as:

$$\begin{aligned} u &= \frac{1}{g_2}\left[\frac{\partial \phi_1}{\partial x_1}(f + g\xi_1) + \frac{\partial \phi_1}{\partial \xi_1}(f_1 + g_1\xi_2) - \frac{\partial V_2}{\partial \xi_1}g_1 - k_2(\xi_2 - \phi_1) - f_2\right] \\ &= -(a\alpha + k_1 - 1)\frac{x_2}{x_1^2}.(-\alpha x_1 + \alpha x_2) + \frac{a\alpha + k_1 - 1}{x_1}(-x_2 - x_1 x_3) \\ &\quad - (x_2 + a x_1)(-x_1) - k_2\Big(x_3 + (a\alpha - \alpha - k_1 a) \\ &\quad - (a\alpha + k_1 - 1)\frac{x_2}{x_1}\Big) - (x_1 x_2 - x_3 - \beta) \\ &= \underbrace{(a\alpha + k_1 - 1)\left(\alpha + k_2 - 1 - \alpha\frac{x_2}{x_1}\right)\frac{x_2}{x_1}}_{\text{Singularity}} \\ &\quad + \left(a x_1^2 - (k_2 - 1)x_3 - k_2(a\alpha - \alpha - k_1) + \beta\right) \end{aligned} \tag{5.25}$$

The above control law is not feasible in terms of implementation due to the first term which has x_1 in the denominator. So, whenever x_1 goes near zero the control action becomes very large. For example, with $\alpha = 4$, $a = 1$, $k_1 = 1$ and $k_2 = 2$, the control action rises to infinity making the system unstable. To evade this problem we have two options in hand:

1. Switching to an alternative control law [e.g., $u = -k(x_3 + 1)$] that can stabilize the system to the desired setpoint whenever control action calculated from the control law [eqn. (5.25)] exceeds a predefined boundary.

2. Choose the parameters a and k_1 in such a way so that the term containing singularity vanishes.

Of the two options, the first option will always work as long as the alternative control law works. For the second case, we need to set the parameter values a and k_1 so that

the terms containing x_1 in the denominator vanishes away. For this purpose set

$$a\alpha - k_1 + 1 = 0$$
$$\Rightarrow k_1 = 1 - a\alpha \tag{5.26}$$

Since by assumption k_1 should be a positive number, choose

$$a = \frac{1}{n\alpha}, \qquad n > 1 \tag{5.27}$$

which gives the final control law to be:

$$u = ax_1^2 - (k_2 - 1)x_3 - k_2(a\alpha - \alpha - k_1) + \beta$$
$$\Rightarrow u = \underbrace{\frac{1}{n\alpha}x_1^2}_{\text{Nonlinear Part}} \underbrace{-(k_2 - 1)x_3}_{\text{Linear Part}} \underbrace{-k_2\left(\frac{2}{n} - \alpha - 1\right) + \beta}_{\text{Constant Part}} \tag{5.28}$$

The final control law defined by eqn. (5.28) has three parts: Nonlinear, Linear and Constant terms. If we take $k_2 = 1$, the linear term vanishes away. From the simulation result it is found that presence of this linear term enhances quick stability of the system to the desired equilibrium points. So, it is better to choose

$$k_2 > 1 \tag{5.29}$$

The constant term however stabilizes the system in a slightly different manner. What it does is that it reduces the heating rate β to the region, where the overall open loop system is stable. Since we want to keep the system in the region where the open loop system is unstable and want to diminish the chaos, the constant term in the control law does not serve our purpose. So, removing the constant part we have the following control law which is actually perturbation around the nominal heating rate:

$$u = \frac{1}{n\alpha}x_1^2 - (k_2 - 1)x_3 \qquad n, k_2 > 1 \tag{5.30}$$

Notice that heating rate is proportional to x_3. Also x_1 denotes fluid velocity inside the convective loop and hence energy loss due to the fluid flow is proportional to x_1^2 [$h_L = f\frac{LV^2}{2gD}$]. So, the control law is actually an energy term which makes it physically understandable. But with this truncated control law the question that immediately comes into the mind is that "Does this truncated control law still makes the system stable?". To answer this question we have to analyze the stability of the closed loop

system with the truncated control law defined by eqn. (5.30). The energy function for the closed loop system with the full control law [eqn. (5.28)] is given by:

$$
\begin{aligned}
V_3 &= V_2 + \frac{1}{2}\left[\xi_2 - \phi_1\right]^2 \\
&= \frac{1}{2}x_1^2 + \frac{1}{2}\left[x_2 + ax_1\right]^2 + \frac{1}{2}\left[x_3 + a\alpha - \alpha - k_1 a\right]^2 \\
\Rightarrow \dot{V}_3 &= \left[\begin{array}{ccc} (1+a^2)x_1 + ax_2 & ax_1 + x_2 & x_3 + a\alpha - \alpha - k_1 a \end{array}\right] \\
&\qquad \times \left[\begin{array}{c} -\alpha x_1 + \alpha x_2 \\ -x_2 - x_1 x_3 \\ x_1 x_2 - x_3 - \beta + u \end{array}\right] \\
&= \underbrace{-(\alpha + a\alpha + k_1 a^2)x_1^2 - k_1 x_2^2 - k_2 x_3^2}_{\text{negative}} \\
&\qquad + \underbrace{(k_1 k_2 + k_2\alpha + k_1 k_2 a - k_2 - \beta)x_3 - 2k_1 a x_1 x_2}_{\text{depends on the sign of } x_1 \text{ and } x_2} \\
&\qquad + \underbrace{(1 - k_1 - \alpha + k_1 a)}_{\text{negative}}\beta
\end{aligned}
\tag{5.31}
$$

Here $\dot{V}_3$ has three terms as shown in eqn. (5.31): a negative quadratic term consisting of x_1^2, x_2^2 and x_3^2, a term containing $x_1 x_2$ and x_3 which depends on the sign of the variable and a constant term. In the constant term $1 - k_1 = \frac{1}{n} \in (0, 1)$ and $k_1 a = (1 - \frac{1}{n})\frac{1}{n\alpha} \in (0, 1)$. Usually the parameter α has value 4, which makes the term $(1 - k_1 - \alpha + k_1 a)$ negative. Nothing can be said about the other two terms containing $x_1 x_2$ and x_3. But if we take a look at the simulation result it is found that except near zero x_1 and x_2 have the same sign making $-2k_1 a x_1 x_2$ negative and even in the extreme conditions when x_3 is negative making $(k_1 k_2 + k_2\alpha + k_1 k_2 a - k_2 - \beta)x_3$ positive but smaller than the other negative terms. This is due to the fact that though the system shows chaotic behavior the states are always confined in a boundary. Hence, the equilibrium points of the system are locally stable with this control action defined by eqn. (5.30). For $\alpha = 4$, $k_2 = 3$ and $n = 2$ $[k_1 = 1 - 1/n = 0.5,\ a = 1/n\alpha = 1/8]$, the control law becomes:

$$u = \frac{1}{8}x_1^2 - 2x_3 \tag{5.32}$$

With the same initial condition as before the response of the controlled system is given in fig. 5.7.

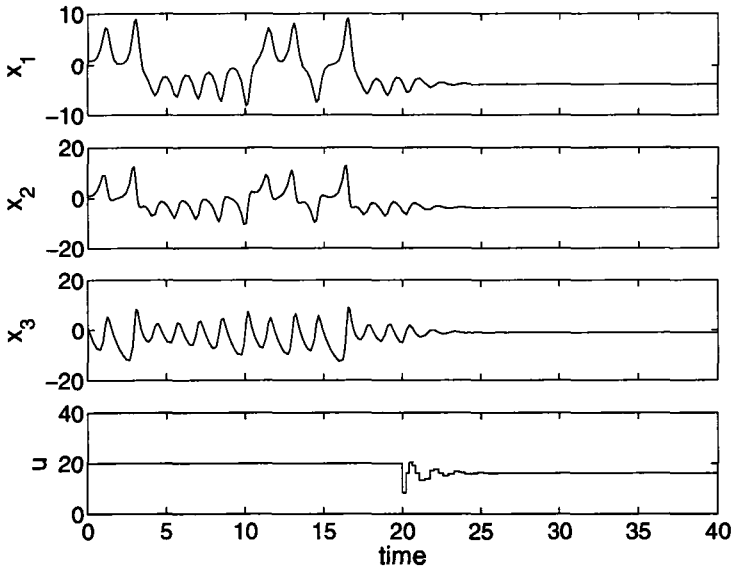

Figure 5.7: Controlled system for $\beta = 20$: Back Stepping method

5.8 Nonlinear Model Predictive Control (NMPC)

In model predictive control, a set of future control actions including the current control action are calculated based on the model of the system. The model of the convective loop reactor is represented by a set of nonlinear ordinary differential equations [eqn. (5.6)]. The model being continuous in nature needs to be discretized before it can be fit as a system model into the model predictive control.

As described earlier in section 4.2, orthogonal collocation method has been employed for discretization of the continuous model. In this case, three interior nodal points have been used to represent the nonlinear function. It has been found that increase in the number of interior nodal points increases the accuracy of the approximation as well as the computational load. Thus choice in the number of interior collocation points is balanced by both the accuracy and the computational load. For our case, three collocation points have been found to be sufficient to approximate nonlinear model of convective loop reactor and, later on, of solid oxide fuel cell system.

In this work, the investigation of the performance of UKF as a state estimator has also been carried out. The result is given in section 5.8.1. The linear and nonlinear MPC have been applied on the reactor to stabilize the system responses to its equilibrium

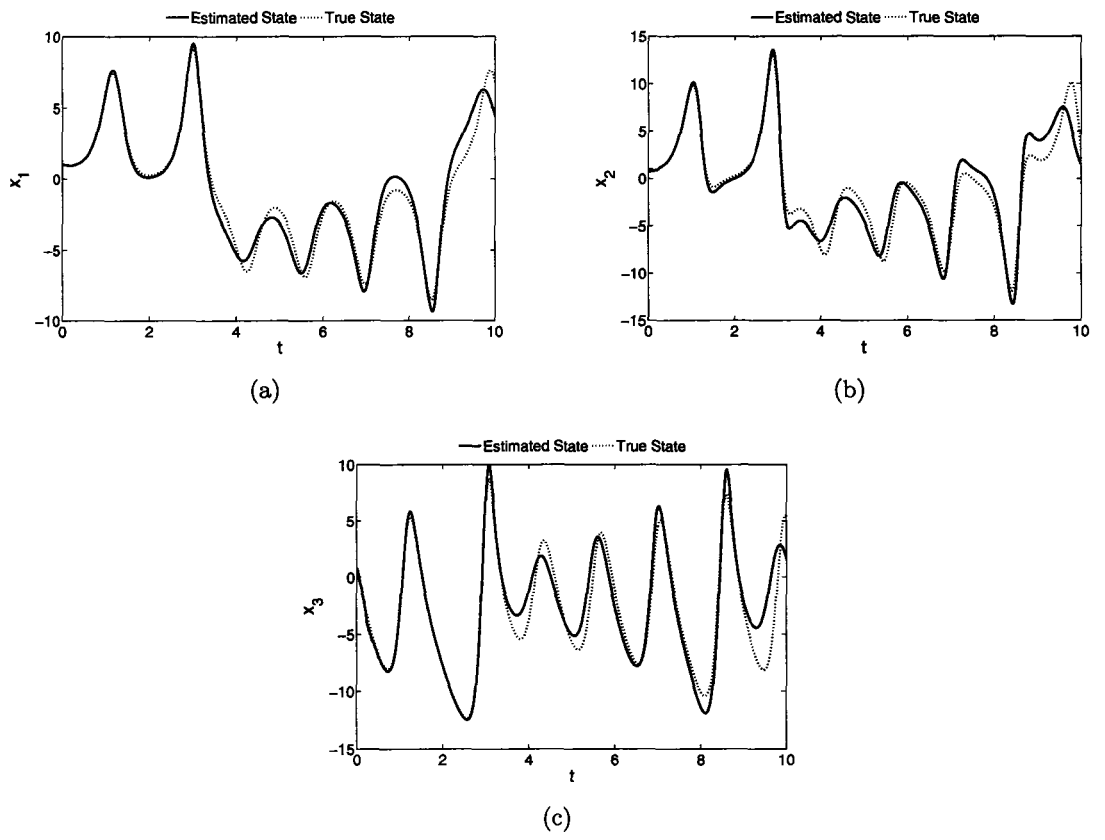

Figure 5.8: State estimation of chaotic reactor by unscented Kalman filter; Discretization has been done by backward approximation of $\Delta T = 0.01$

points. The results are shown in section 5.8.2.

5.8.1 State estimation

The model of a thermal convective loop reactor as expressed by eqn. (5.6) has two parameters - α and β ($\beta = u$, since β is the manipulated variable in our control scheme). These parameters define extent of chaotic behavior by the reactor. For $\alpha = 4$ and heating rate of $u = 20$, the reactor exhibits chaotic behavior.

Implementation of UKF requires a discrete model. The accuracy of UKF thus depends on how close the discretized model is to the continuous model. Both backward approximation and MATLAB ODE solver have been used to discretize the model.

Assuming that only state x_1 is measurable, UKF has been used to estimate the

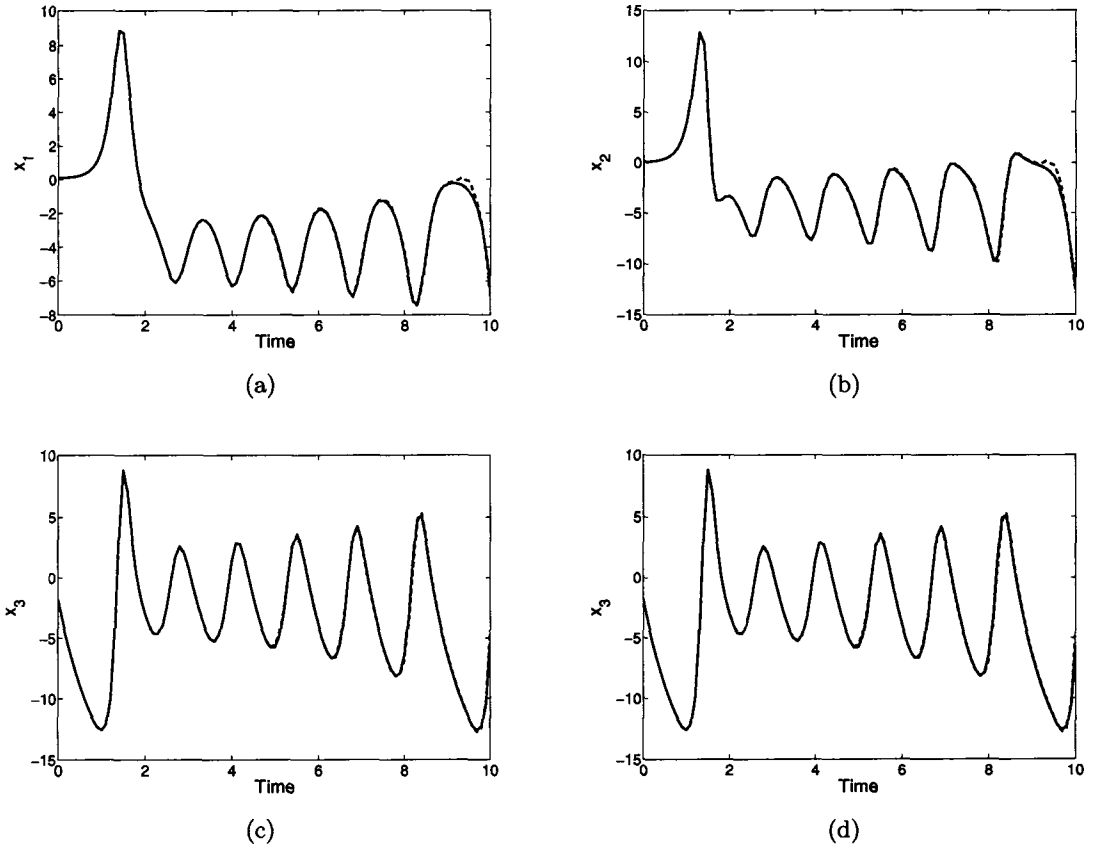

Figure 5.9: State estimation of chaotic reactor by unscented Kalman filter; Discretization has been done by MATLAB ODE solver

unmeasured states with a sampling interval $\Delta T = 0.01$[2]. The results are shown in fig. 5.8. Here the 'true states' are the outputs from the continuous model and 'estimated states' are the outputs from UKF using discretized model by backward approximation. The estimation of unmeasured states depends on the sampling interval. In this case, less sampling interval gives more accurate estimation but with a heavier computational load, which makes it impractical. On the other hand, sampling interval of 0.1 or higher results in poor estimation of the states. Even though sampling interval of 0.01 works out to be a feasible one, for a complex system like SOFC, this might not be good solution.

The other two alternative options - orthogonal collocation method and MATLAB ODE solver, as described in section 4.3.2, turns out to be equally applicable. The result of UKF state estimation by employing MATLAB ODE solver is shown in

[2]The states, control and time unit in this example are normalized

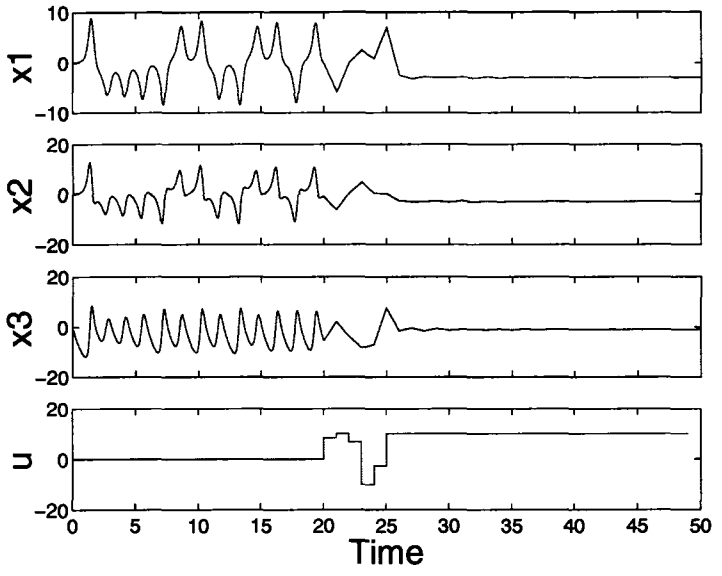

Figure 5.10: Linear MPC; Prediction Horizon = 1, Control Horizon = 1, $\Delta T = 1$, $Q = R = 1$, $S = 0$

fig. 5.9. The accuracy of state estimation is better than that of backward approximation. This better result is evident even without performing any simulation - since MATLAB ODE solver utilizes better discretization scheme than a simple backward approximation. For this particular case, an 50% error in the noise covariance matrix has also been introduced to simulate worst case scenario.

5.8.2 Result

In addition to controllers described in the previous sections, linear and nonlinear MPC have been applied on the convective loop reactor to stabilize its chaotic behavior. The performance of the controllers depends on the sampling time, ΔT, and the penalty of the state and input variables in the objective function, Q, R, and S. The simulation has first been run without any addition of noise and assuming that all the states are measurable (figs. 5.10-5.13). Then NMPC has been applied on the reactor model assuming that only noisy measurement of horizontal temperature difference is available (fig. 5.14). The results are presented below.

The fast dynamic system with highly nonlinear behavior makes it difficult to laminarize (or, stabilize) the system using linear model predictive controller. Surprisingly

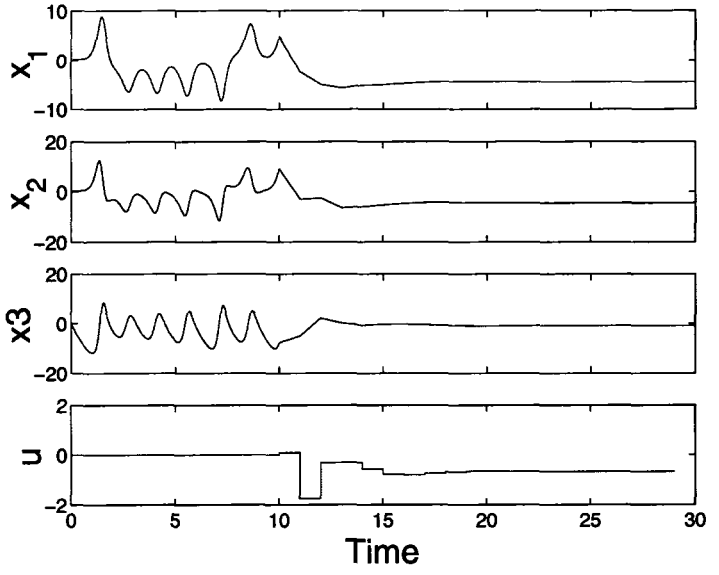

Figure 5.11: Linear MPC; Prediction Horizon = 5, Control Horizon = 2, $\Delta T = 1$, $Q = 1$, $R = S = 0$

linear MPC with prediction horizon one gives better control than with prediction horizon greater than one for the same sampling time. It is evident from the fact that for this fast chaotic dynamic system a linear model with a smaller prediction horizon (fig. 5.10) can track the system better than that of a linear model with a large prediction horizon (fig. 5.11). In every case, the output of linear MPC however never comes to zero. The output from the linear MPC hits the upper constraint of control action and stays there which in fact is equivalent to moving the system from the chaotic region to nonchaotic one and thus making the system stable.

Nonlinear MPC, on the other hand, can stabilize the chaotic system very well. The control action decays rapidly to zero (see fig. 5.12, 5.13). The time for stabilization depends greatly on the penalty functions on the states and input in the objective function of the optimization problem as well as the sampling rate[3]. The input limit and its change depend on the constraint used in the minimization problem. Thus in fig. 5.12 due to the input rate constraint limited to 5 control moves does not change instantly as in fig. 5.13 but it takes more time to stabilize the system. So, less stabilization time comes at the cost of larger control energy. From the figures it is also evident that low sampling rate leads to better control.

[3]The time interval for implementing control action is also equal to the sampling rate

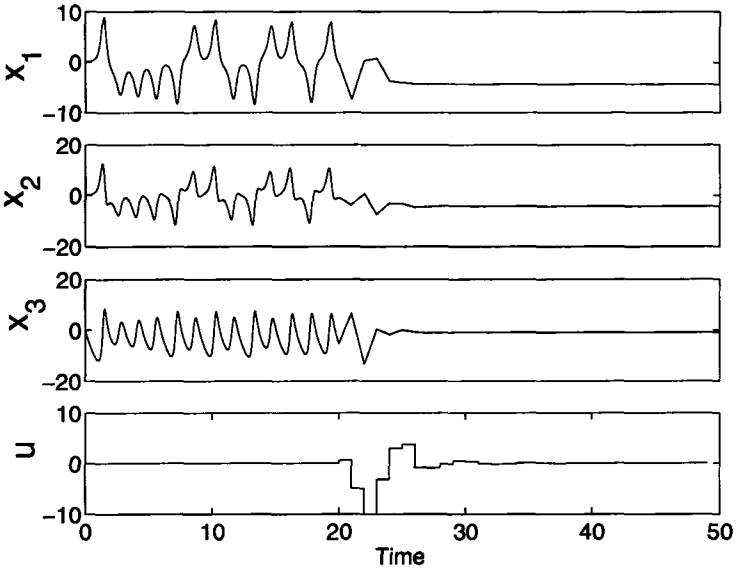

Figure 5.12: Nonlinear MPC; Prediction Horizon = 5, Control Horizon = 2, $\Delta T = 1$, $Q = R = 1$, $S = 0$

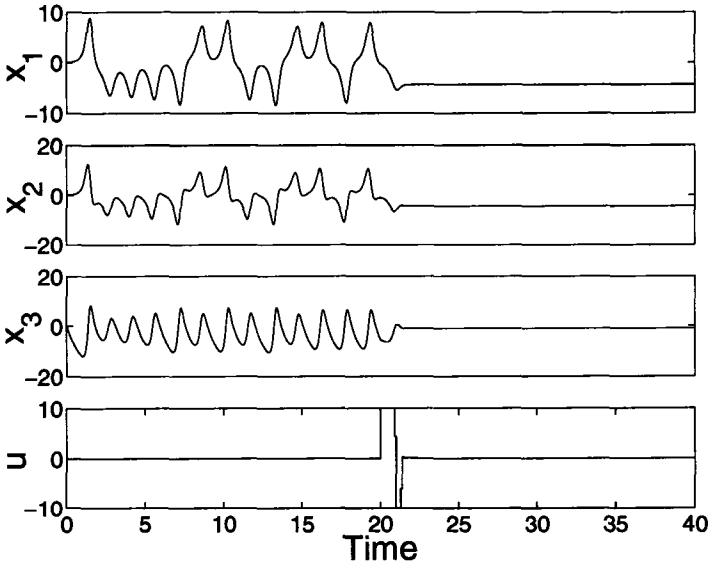

Figure 5.13: Nonlinear MPC; Prediction Horizon = 5, Control Horizon = 2, $\Delta T = 0.1$, $Q = 1, R = S = 0$

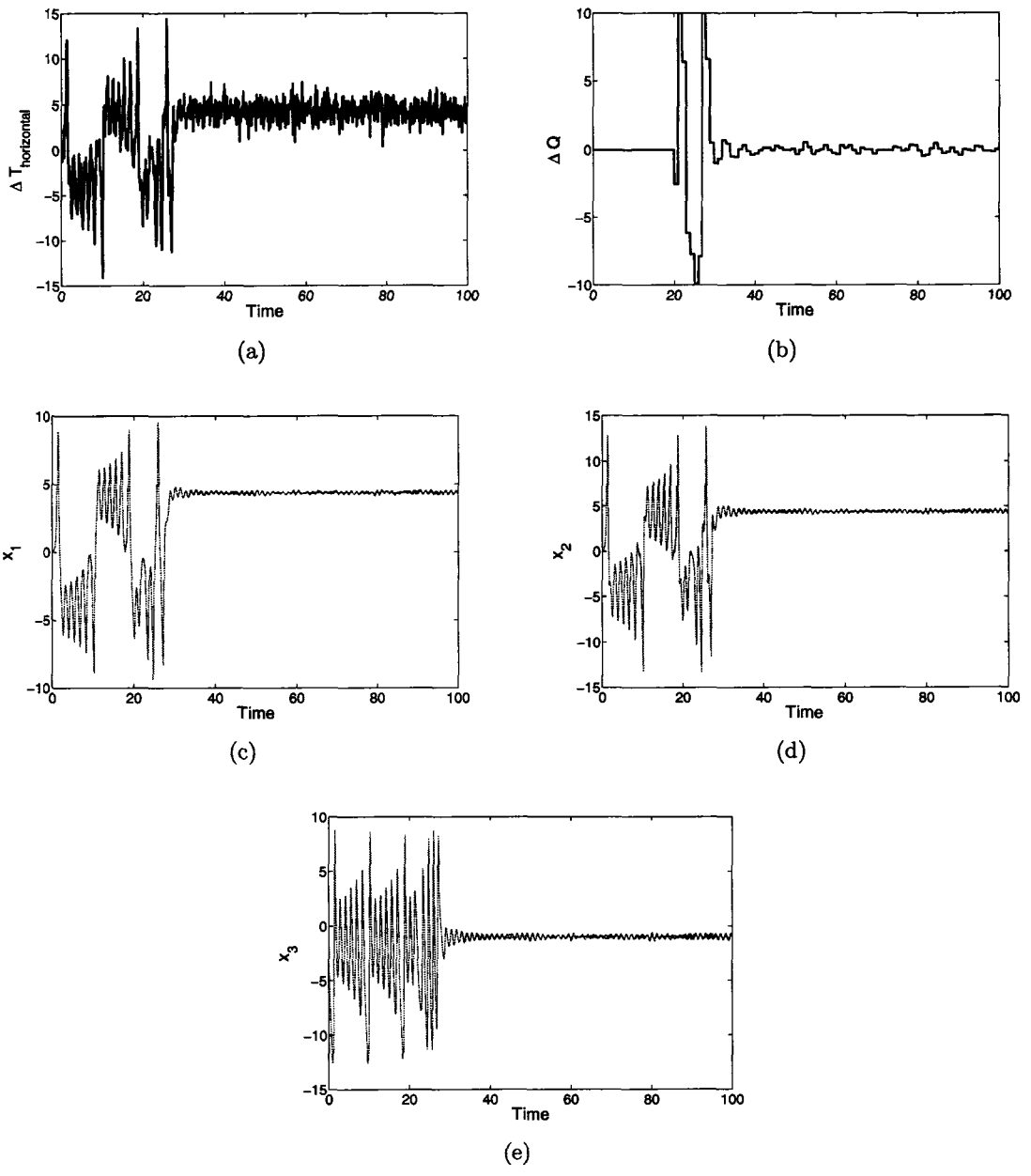

Figure 5.14: Control of convective loop reactor by NMPC along with UKF as state estimator. (a) horizontal temperature difference (measured output); (b) control action (deviation from the nominal heating rate) taken by NMPC; (c),(d),(e) present the true and estimated states. Here, states are estimated with sampling interval $\Delta T = 0.1$ but NMPC is calculated and applied with $\Delta T = 1$.

Nonlinear MPC has also been applied on the convective loop showing chaotic behavior along with UKF as state estimator. Here only the horizontal temperature difference of the convective loop is measured and the other two states (vertical temperature difference and flow rate inside the tube) are estimated using UKF. However instead of discretizing the model using backward approximation, continuous model is used to predict future data points. Measurement noise is also added in the horizontal temperature difference which is filtered by UKF. The filtered output is then used to calculate future control moves by NMPC. The results are shown in fig. 5.14.

5.9 Conclusion

For this system, Nonlinear Model Predictive Control (NMPC) outperforms other controller in terms of stabilizing time and control action. One of its main disadvantages is high computational time. With the advent of high performance computer however this is not a major problem anymore. Another disadvantage of NMPC is that tuning of the parameters in the objective functions has to be tried through a number of simulations. In addition, the model parameters (α and β) need to be correctly identified for the implementation of the controller.

Although computational time for Linear MPC is much smaller than Nonlinear MPC, it cannot regulate the system to its desired setpoint unless the sampling time is very small.

Among others, linear state feedback controller with setpoint tracking [eqn. (5.10)] and nonlinear controller based on Lyaponov Stability Criterion [eqn. (5.12)] also give better result in comparison to others in terms of stabilizing time and movement rate of controller. Of these two, the linear controller is less sensitive to the initial condition *i.e.*, the time when controller is implemented and gives less fluctuation in the control action when measurement noise is present. The nonlinear controller stabilizes the system quickly but gives a lot of spikes in the control action if noise is present. In this case, we assume that the states are measurable and available for calculation. If any state is not measurable, then a nonlinear observer can be used to estimate the

unknown states and calculate the control law. In this case, the performance of the controller will depend on the performance of the observer as well.

Chapter 6

Control of Solid Oxide Fuel Cell System

6.1 Introduction

A fuel cell system includes many components in addition to the fuel cell itself. The components are built around the fuel cell to maximize the efficiency of the system which, depending on the objective, may include heat exchangers, turbine, boiler, DC-AC converter etc. Optimal operation of the system thus requires efficient operation of these integral components, which put constraints on the overall operation of the fuel cell system. Thus, designing a controller of a fuel cell system requires handling multivariate objective and meeting constraints set by the components' safe operation limit. The nonlinear dynamics of the fuel cell makes it more challenging even when designing the regulatory controller.

Design of a controller for a fuel cell system has to address the following issues: i) handle the abrupt change nature of the fuel cell during transient operation, ii) reach the target load efficiently, and iii) meet the constraints set by the different components' safe operation limit. The first issue, which is accompanied by a sudden instantaneous change of voltage for a change in the load, can be handled with the addition of a capacitor. Theories and merits of the capacitor as an auxiliary power source have been addressed in section 3.6 in the fuel cell modeling chapter, and also in section 6.5.3 of this chapter. The other two problems can be met by employing a multivariate control

that has the capability of handling constraints. Consequently, it is proposed to solve the problems by employing nonlinear model predictive control (NMPC).

A number of different well established nonlinear control schemes have been available to improve the load following capability. However, in this work only nonlinear model predictive control (MPC) will be considered. The results from nonlinear MPC (NMPC) have also been compared with the traditional linear MPC (LMPC). The reason for applying nonlinear MPC, instead of other nonlinear controls, such as, back-stepping method, is two fold. First, in the previous case study, nonlinear MPC stood out to be the best compared to other nonlinear controls when applied to convective loop reactor. Second, development of nonlinear control like back-stepping method is relatively simple when the model is of simple nonlinear nature and if the energy function is also available. For a complex nonlinear model, like the fuel cell and its system, it is not easy to derive an energy function that can lead to physically understandable and implementable control law. Even if the energy function is available, the deduction of control law is difficult and, most importantly, it will not be able to handle the constraints.

In the previous chapter, the discretization of the nonlinear continuous fuel cell and system models have been performed by employing orthogonal collocation method. In this method, three interior nodal points have been used. This method does not give an explicit discrete model, but can still be easily incorporated with nonlinear MPC framework. A detailed discussion of this method has been provided in section 4.2.

In addition to discretization, implementation of nonlinear (or, linear MPC) requires estimation of unmeasured states. This can be performed by employing a suitable observer. In this work, unscented Kalman filter (UKF) has been chosen over well established extended Kalman filter (EKF). The advantage of UKF again comes from the inherent complex structure of fuel cell and system models. EKF, which requires Jacobian of the model, is difficult to implement for our case. On the other hand, UKF does not require the Jacobian. It also generates more accurate estimation over EKF (Haykin [54], Julier [70], Julier et al. [71], Lee [80], Rui and Chen [120], Wan and Merwe [141, 142]).

The chapter is organized as follows: section 6.2 gives a brief overview on the methodology of linear and nonlinear model predictive control followed by unscented Kalman filter for estimating unmeasured states in section 6.3. This section also validates the performance of UKF as a state estimator. Section 6.4 provides a detailed discussion on running the fuel cell system optimally such that indirect energy from the fuel cell system is minimal at steady state. Simulation results of linear MPC, nonlinear MPC, and maximization of the direct energy are provided in section 6.5 followed by a discussion on issues encountered during the simulation in section 6.6 and conclusion in section 6.7.

6.2 Nonlinear Model Predictive Control Revisited

Nonlinear model predictive control is a generalized version of linear model predictive control. It uses nonlinear process model to predict the effect of past input actions and calculates a series of inputs such that an objective function is minimized. The optimization scheme also includes different constraints that have to be satisfied. First of the future calculated moves is then implemented, and the entire optimization is carried out again. Mathematically the NMPC formulation can be expressed as:

$$\min_{u(k|k),u(k+1|k),\cdots,u(k+M-1|k)} J = \sum_{i=1}^{N} [\|\hat{x}(k+i|k) - x_{ref}\|_Q^2 + \|u(k+i|k) - u_{ref}\|_R^2 + \|\Delta u(k+i|k)\|_S^2] \quad (6.1)$$

subject to,

$$\hat{x}(k+1) = f(\hat{x}(k), u(k), w(k)) \quad (6.2)$$

$$y_{min} \leq \hat{y}_i \leq y_{max} \quad (6.3)$$

$$u_{min} \leq u_i \leq u_{max} \quad (6.4)$$

$$\Delta u_{min} \leq \Delta u_i \leq \Delta u_{max} \quad (6.5)$$

Since the model predictive control utilizes models to predict future outputs and compares them with the setpoints, the accuracy of the model is important for the performance of the controller. The fuel cell and system model described in chapter 4 can

be presented by the following general nonlinear form:

$$\dot{x} = f(x, u, w) \tag{6.6}$$

$$y = g(x, w) \tag{6.7}$$

The NMPC formulation can thus be rewritten, together with the discretized model from the orthogonal collocation method, as:

$$\min_{u(k|k),u(k+1|k),\cdots,u(k+M-1|k)} J = \sum_{i=1}^{N} [\|\hat{x}(k+i|k) - x_{ref}\|_Q^2 + \|u(k+i|k) - u_{ref}\|_R^2 + \|\Delta u(k+i|k)\|_S^2] \tag{6.8}$$

subject to,

$$\tilde{A}\tilde{X} = \tilde{F}(\tilde{X}, U) \tag{6.9}$$

$$y_{min} \leq \hat{y}_i \leq y_{max} \tag{6.10}$$

$$u_{min} \leq u_i \leq u_{max} \tag{6.11}$$

$$\Delta u_{min} \leq \Delta u_i \leq \Delta u_{max} \tag{6.12}$$

6.3 State Estimation: UKF

UKF has been applied to the fuel cell system described by the detail model [see section 4.3.1 for an overview of UKF]. As stated earlier in section 4.3.2, discretization of continuous model can be performed by employing backward approximation, by using orthogonal collocation method or, simply using a MATLAB built-in solver. Among these methods, backward approximation is suitable for simple linear and nonlinear model. For convective loop reactor, a time step of 0.001 provides as a good estimate of states as the other two methods. However, for fuel cell system models even smaller time steps fail to produce an acceptable estimate. The computational burden with the decrease of time step also makes it impractical to implement.

The rest two methods provide good estimates of the states with fairly similar accuracy. In this work, MATLAB ODE solver has been used to generate discrete data to be used as a discrete model in UKF. The performance of UKF has been tested for estimating

unmeasured states of stand-alone fuel cell and entire fuel cell system before applying it to nonlinear model predictive control. The simulation results follow.

Fig. 6.1 shows the estimated partial pressures of a stand-alone fuel cell described by the lumped model of section 3.4. Here only the exit temperature of the fuel cell gases (which is assumed to be same as the cell temperature) and the stack voltage are measured. Comparison of the estimated states with the true states reveals that even though the initial conditions of the states are not exactly known, the estimated states quickly converge to the true states.

Fig. 6.2 shows the performance of UKF as an estimator for the entire fuel cell system. Here, only different flow temperatures and stack voltage are assumed to be measurable. Other fuel cell component temperatures and the partial pressures of hydrogen, oxygen and steam are estimated. From the simulation, it is evident that the estimated states quickly converge to the true value of the system.

6.4 Maximizing Direct Energy, or Minimizing Indirect Energy

Fuel cell converts chemical energy of fuel directly into electrical energy and thus can have high efficiency. The unreacted fuel can then be burned to produce additional energy. The high temperature exhaust from the fuel cell system can be used to generate further electricity using gas turbine or simply produce hot water and steam for home and industrial use. The energy produced from a fuel cell system can be classified into two parts:

- **Direct Energy:** Energy produced by the fuel cell itself. This energy is named "Direct", because of the fact that the fuel cell converts chemical energy directly into electric energy.
- **Indirect Energy:** Energy produced from the unreacted fuel gas from the fuel cell.

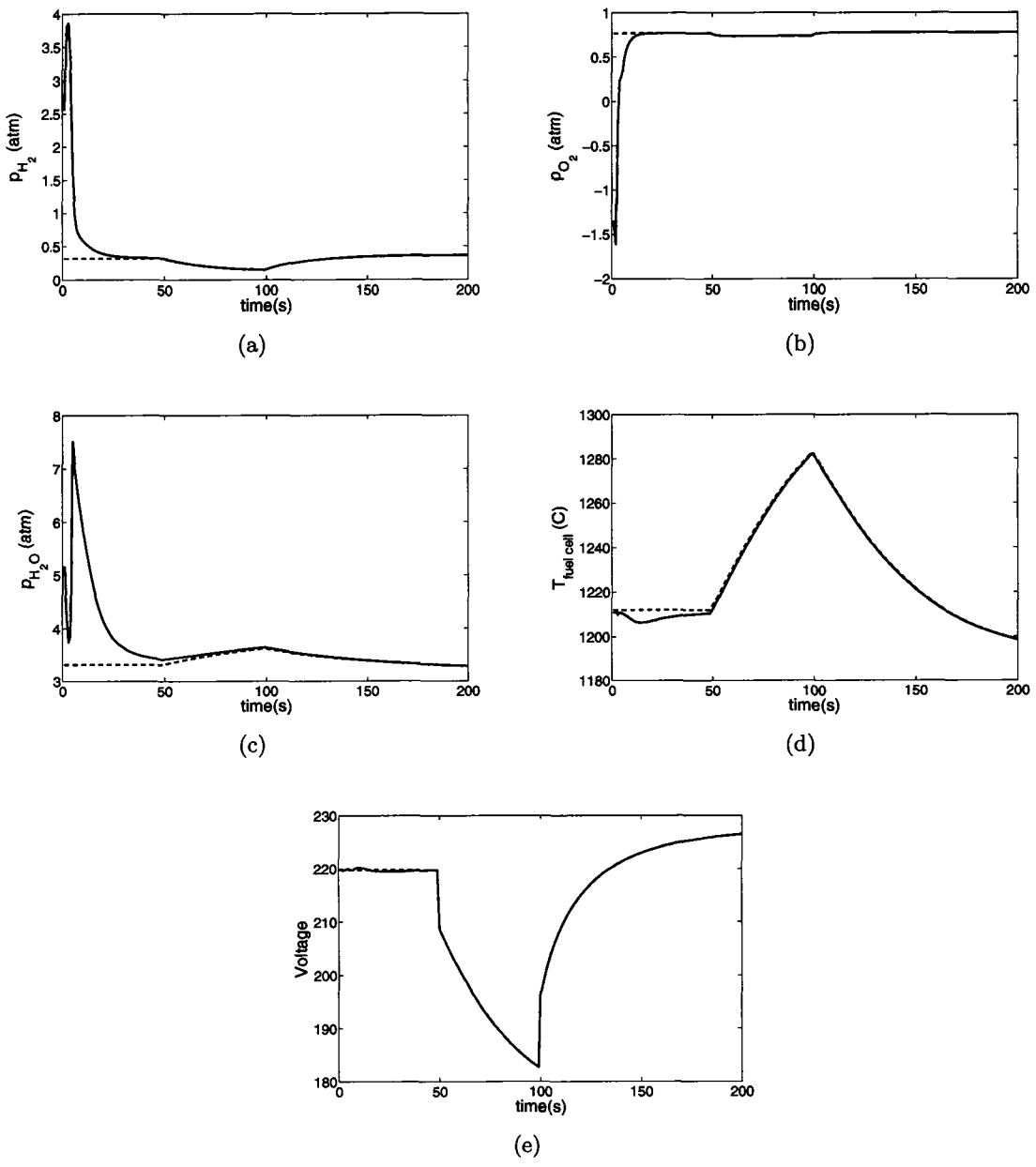

Figure 6.1: State estimation of stand-alone SOFC by UKF by assuming that only the cell temperature and voltage are measurable

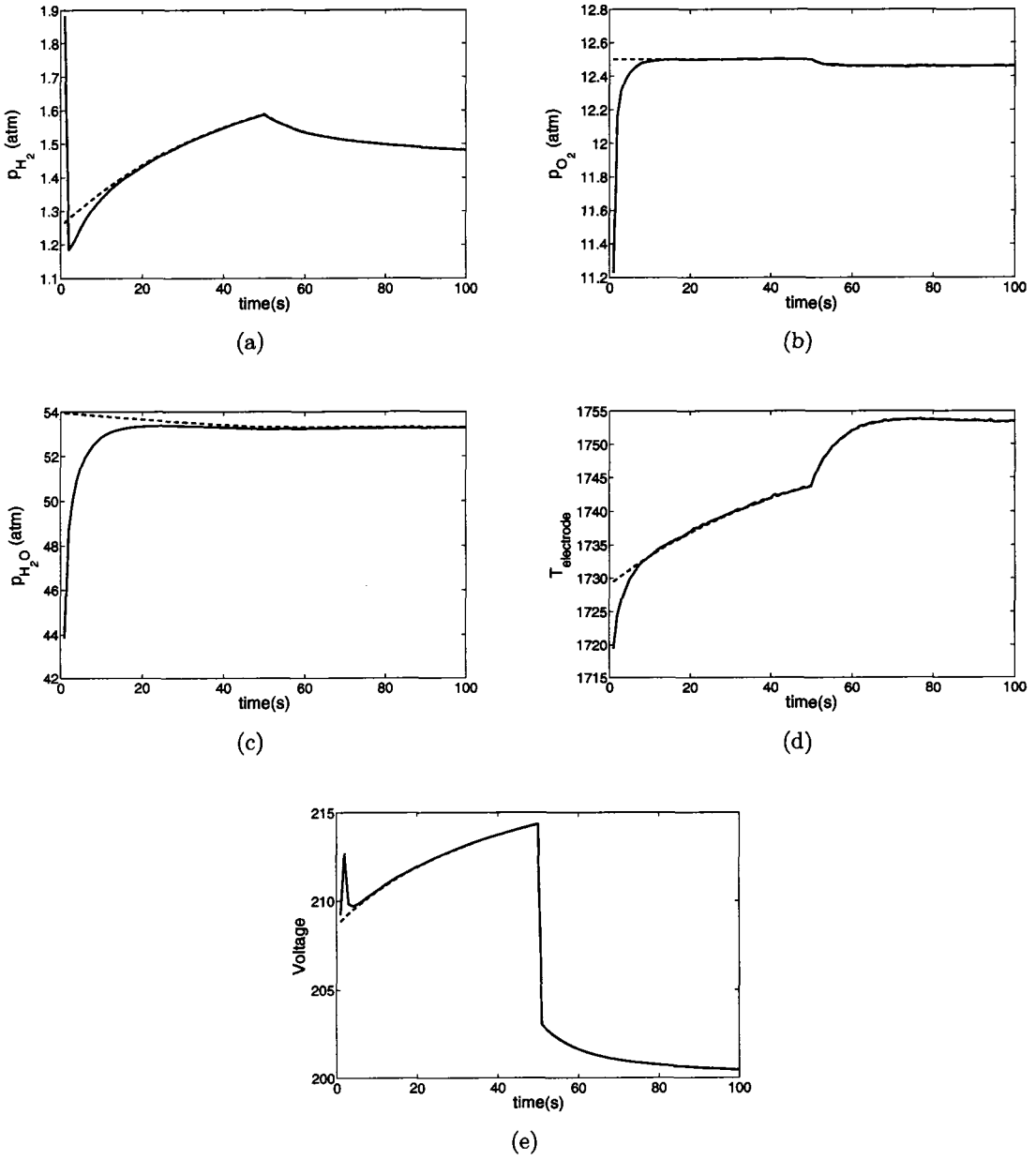

Figure 6.2: State estimation of SOFC system by UKF by assuming that only the flow temperatures and stack voltage are measurable

Even though the indirect energy provides a good part of the fuel cell system power, the main objective for a fuel cell system is to produce as much direct energy as possible. In other words, the energy content of exhaust from a fuel cell system should be minimal.

Since the energy from the exhaust mainly comes from burning the unreacted fuel, minimizing the cost or heating value of unreacted fuel maximizes direct energy output. However the unreacted fuels are burnt and then used to preheat the fuels in the system. Thus instead of minimizing cost or, heating value of the unreacted fuel, minimizing extractable energy from the exhaust gas is more appropriate. This, in turn, is equivalent to minimizing fuel use for producing power at the designated voltage. The objective thus is to operate the fuel cell system at an optimal steady state such that extractable energy of the exhaust gas is minimal for a given demand current and designated voltage. For the fuel cell system depicted in fig. 3.3, the mathematical formulation can be written as follows:

$$\min_{U_s} \sum \dot{n}_{i,E} \int_{T_{ref}}^{T_{AE}} C_{p,i}(T)dT + \dot{n}_{i,E}\frac{1-r}{r}\int_{T_{ref}}^{T_B} C_{p,i}(T)dT \tag{6.13}$$

subject to,

$$\begin{aligned} & f(X_s, U_s, W_s) = 0 \qquad \text{[steady-state model]} \\ & V_s = V_{ref} \\ & X_{min} < \hat{X}_s < X_{max} \quad \text{[NMPC constraints]} \end{aligned}$$

where, U_s's are the steady-state inputs (flow rates and splitting ratio, r) of the fuel cell system; $\dot{n}_{i,E}$'s are the flow rates of exhaust gases out of air heat exchanger; T_{AE} and T_B are the exit temperatures of the air heat exchanger and burner respectively; T_{ref} is the reference temperature.

The optimal inputs from the above formulation can then be used as a reference input in nonlinear model predictive control [eqn. (4.3)] for a guaranteed minimal energy in the exhaust at steady-state. This steady-state optimizer can be used on top of the MPC controller and invoked when necessary.

Minimization of direct energy can also be performed dynamically at each NMPC step as opposed to the steady state optimization described above. In this case, the above objective function can be merged with the objective function of NMPC with appropriate weights of Q, R, S, and $W_{indirect}$:

$$\begin{aligned}\min_{u(k|k),u(k+1|k),\cdots,u(k+M-1|k)} J = \sum_{i=1}^{N}[&\|\hat{x}(k+i|k) - x_{ref}\|_Q^2 \\ &+ \|u(k+i|k) - u_{ref}\|_R^2 + \|\Delta u(k+i|k)\|_S^2] \\ &+ W_{indirect}\Big[\sum \dot{n}_{i,E}\int_{T_{ref}}^{T_{AE}} C_{p,i}(T)dT \\ &+ \dot{n}_{i,E}\frac{1-r}{r}\int_{T_{ref}}^{T_B} C_{p,i}(T)dT\Big] \end{aligned} \tag{6.14}$$

subject to,

$$\hat{x}(k+1) = f(\hat{x}(k), u(k), w(k))$$

$$y_{min} \leq \hat{y}_i \leq y_{max}$$

$$u_{min} \leq u_i \leq u_{max}$$

$$\Delta u_{min} \leq \Delta u_i \leq \Delta u_{max}$$

This formulation has two disadvantages. First, the computational burden will be unduely high provided that the system is expected to operate mostly around steady state with occasional change in the demand current. Second, the weighting matrices Q, R, S, and $W_{indirect}$ in the objective function will determine whether the system is controlled dynamically or, optimized for steady state. Emphasizing on minimization of indirect energy will cost the control performance at transient state and vice versa. On the other hand, if the schemes are kept separated, then both objectives are satisfied without sacrificing any of them. Thus, the SOFC system will be optimized to run at minimal energy at steady state as described by objective function in eqn. (6.13). The simulation results of nonlinear MPC by employing the reference input are shown in section 6.5.4.

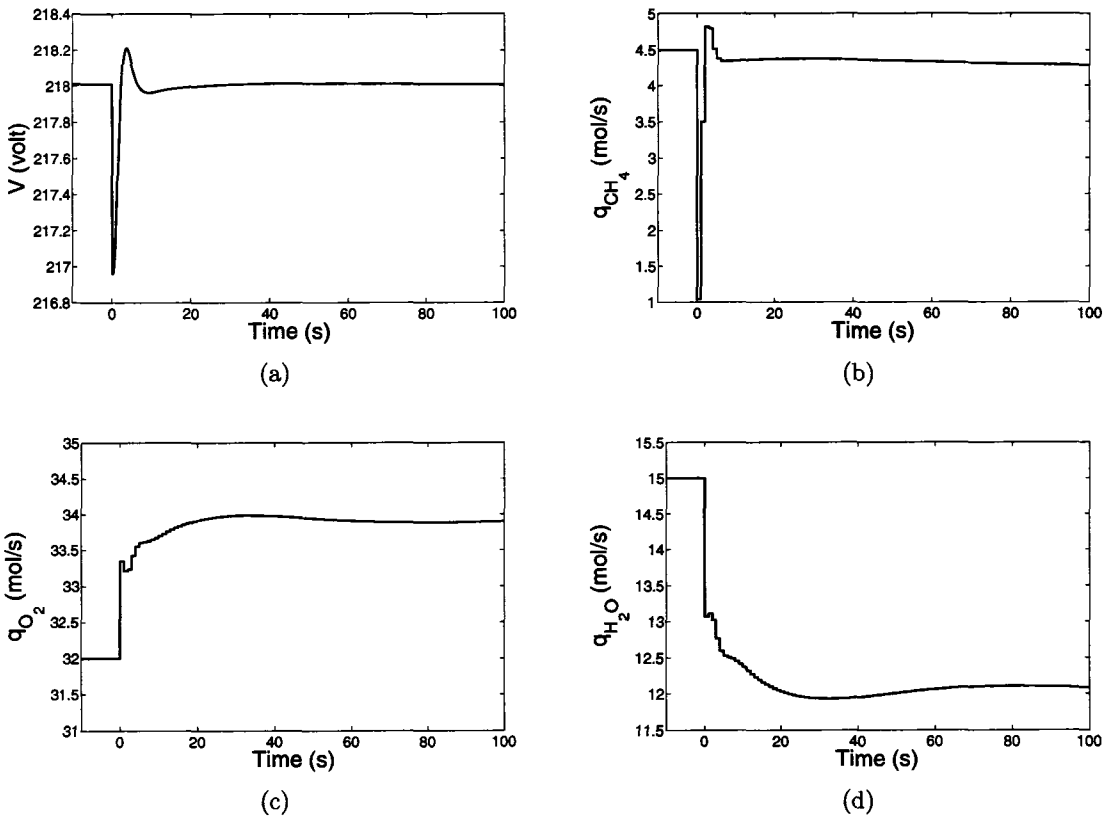

Figure 6.3: Response to a load change of 500 to 510 amp; Here, PH=10, CH=3, Ts=1 sec

6.5 Results

In this section, simulations are performed to determine the load rejection capability of both linear and nonlinear MPC. Both linear and nonlinear MPCs have been applied to stand-alone fuel cell and fuel cell system along with a capacitor connected in parallel with the fuel cell. The results are given in the following subsections.

6.5.1 Linear MPC

MATLAB MPC toolbox has been used for applying linear MPC on the fuel cell system. The fuel cell system, in this case, is linearized around a nominal operating point using MATLAB linear system analysis toolbox. The state estimation of the unmeasured states is integrated into MPC formulation. Thus, no external observer is required.

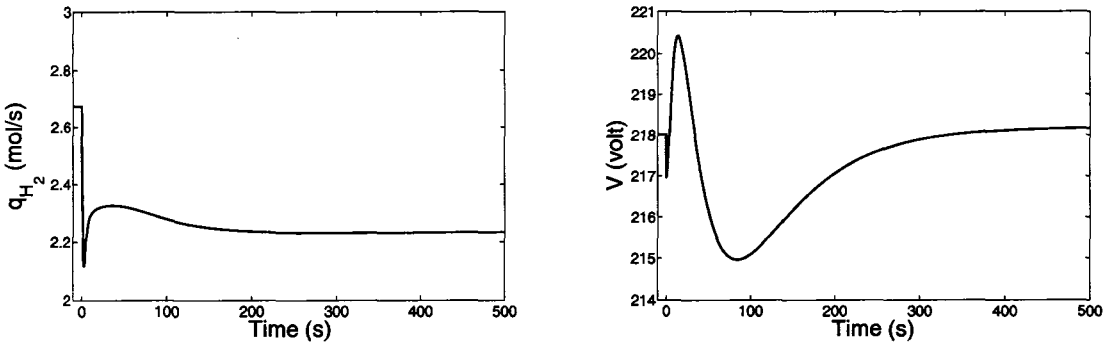

(a) (b)

Figure 6.4: (a) Exit flow rate of H_2 (mol/s) from reformer (b) Response to a load change of 500 amp to 510 amp with simultaneous change in flow rates to its optimal steady state value estimated by LMPC from fig. 6.3.

Fig. 6.3 shows the transient response of the fuel cell system and the control actions taken by the controller for small load disturbance of $I = 500$ to 510 amp. The prediction and control horizons of the linear MPC are 10 and 3 respectively with a sampling interval of 1 second.

From fig. 6.3, it is seen that flow rate of methane settles down from 4.50 mol/s to a lower value of 4.24 mol/s even though the current load has been increased from 500 amp to 510 amp. By intuition, the fuel flow rate should increase with the increase in the load demand. But, in fact, voltage and current relationship does not only depend on the flow rate of fuel but also on the flow rates of O_2 and H_2O. From the Nernst equation, it is evident that the voltage increases with an increase in the partial pressures of flow rates of H_2 and O_2 and decreases with the increase of partial pressure of H_2O. For this particular case, the H_2 production rate from the reformer is shown in fig. 6.4(a). Even though the flow rate of H_2 from the reformer decreases with the increase in load, the increase in the flow rate of O_2 from 32 mol/s to 33.96 mol/s and decrease of H_2O flow rate from 15 mol/s to 12 mol/s overshadow this effect and thus help bring voltage to its reference value [see, fig. 6.3(c), fig. 6.3(d)].

The response of the fuel cell system for a load change of 500 to 510 amp with simultaneous changes in the flow rates calculated by LMPC is shown in fig. 6.4(b). The controller quickly stabilizes the system to its target, which is one of the main attractive features of model predictive control.

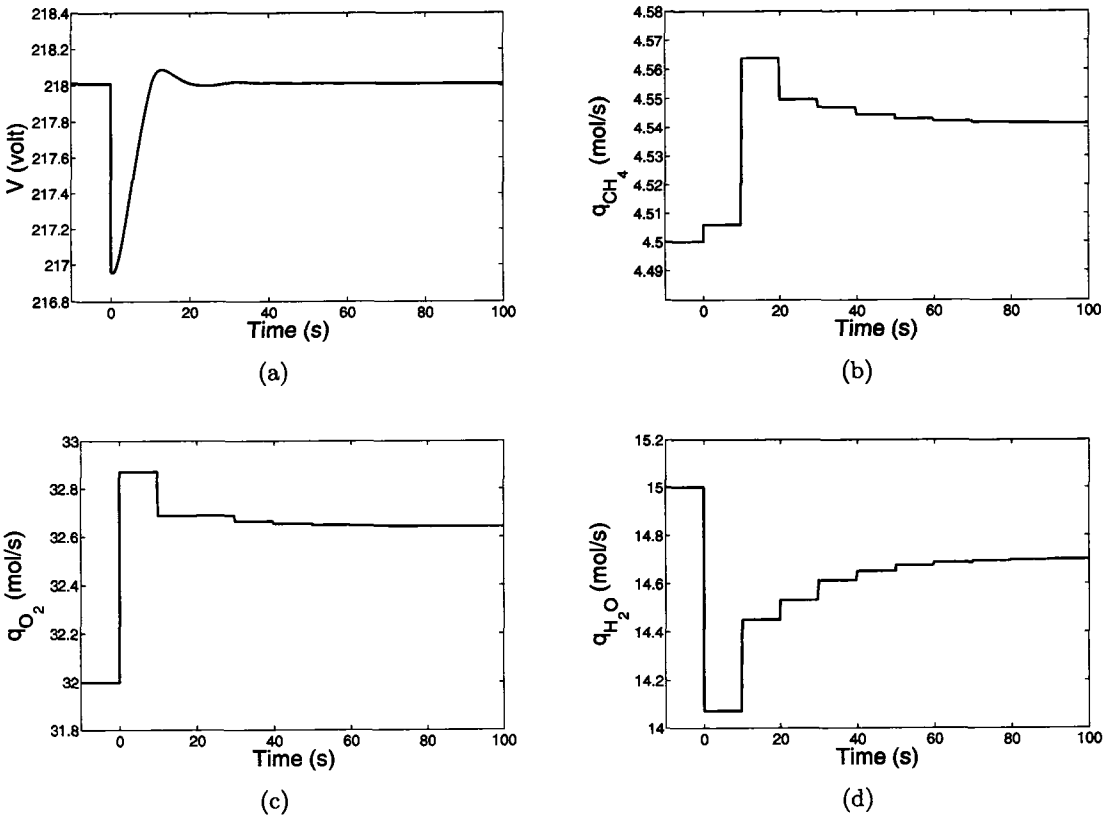

Figure 6.5: Response to a load change of 500 to 510 amp; Here, PH=10, CH=3, Ts=10 sec

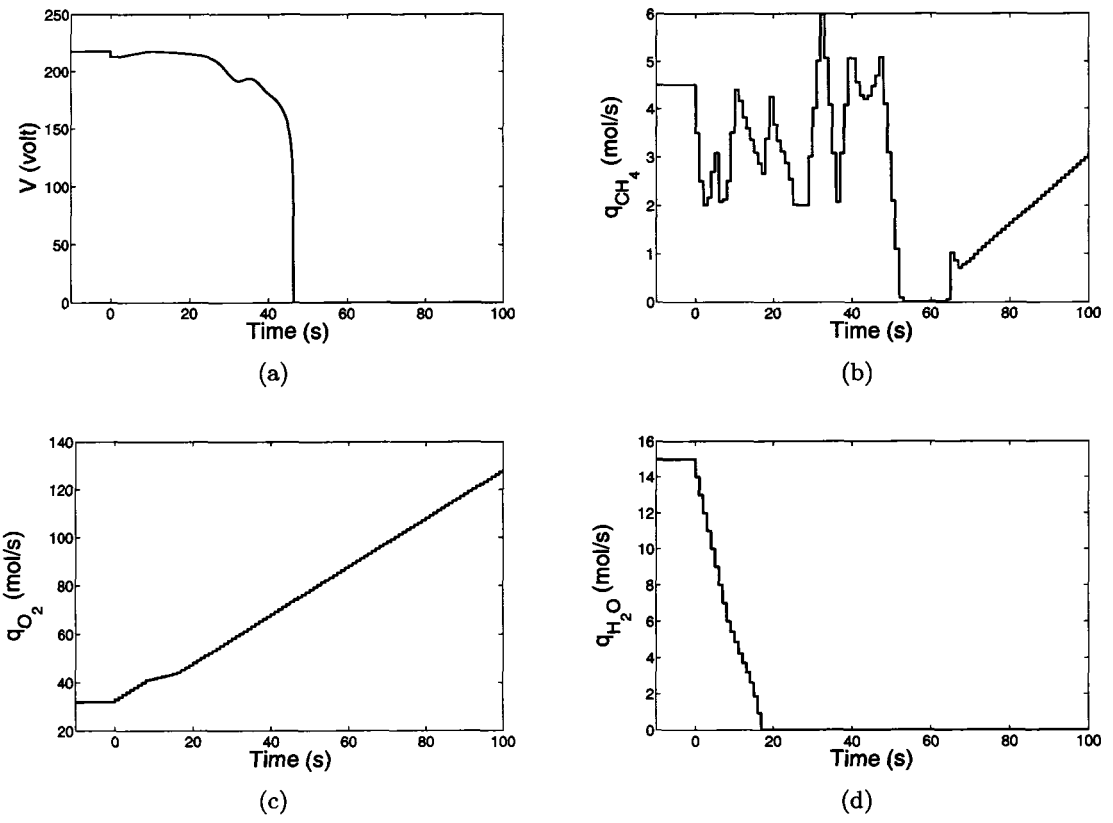

Figure 6.6: Response to a load change of 500 to 550 amp; Here, PH=10, CH=3, Ts=1 sec

Fig. 6.5 shows the effect of increasing the sampling interval from 1 second to 10 second. For small load disturbance, the effect of prediction horizon, in terms of time frame, is not prominent. But for large disturbances, the choice of sampling interval contributes to the performance of the controller, as shown in fig. 6.7.

Following a small successful load disturbance rejection by LMPC, several load changes of different magnitudes have been applied to the system for different prediction and control horizons. However, it can be seen from fig. 6.6, that LMPC is not able to regulate the voltage to its reference value for a load change of 500 to 550 amp and eventually shows unstable behavior, leading to shutdown of the fuel cell system. In this case, the prediction and control horizon are 10 and 3 respectively with a sampling interval of 1 second.

This type of unstable behavior is not unexpected from linear MPC with small prediction horizon. It should be remembered that the nonlinear model is first linearized

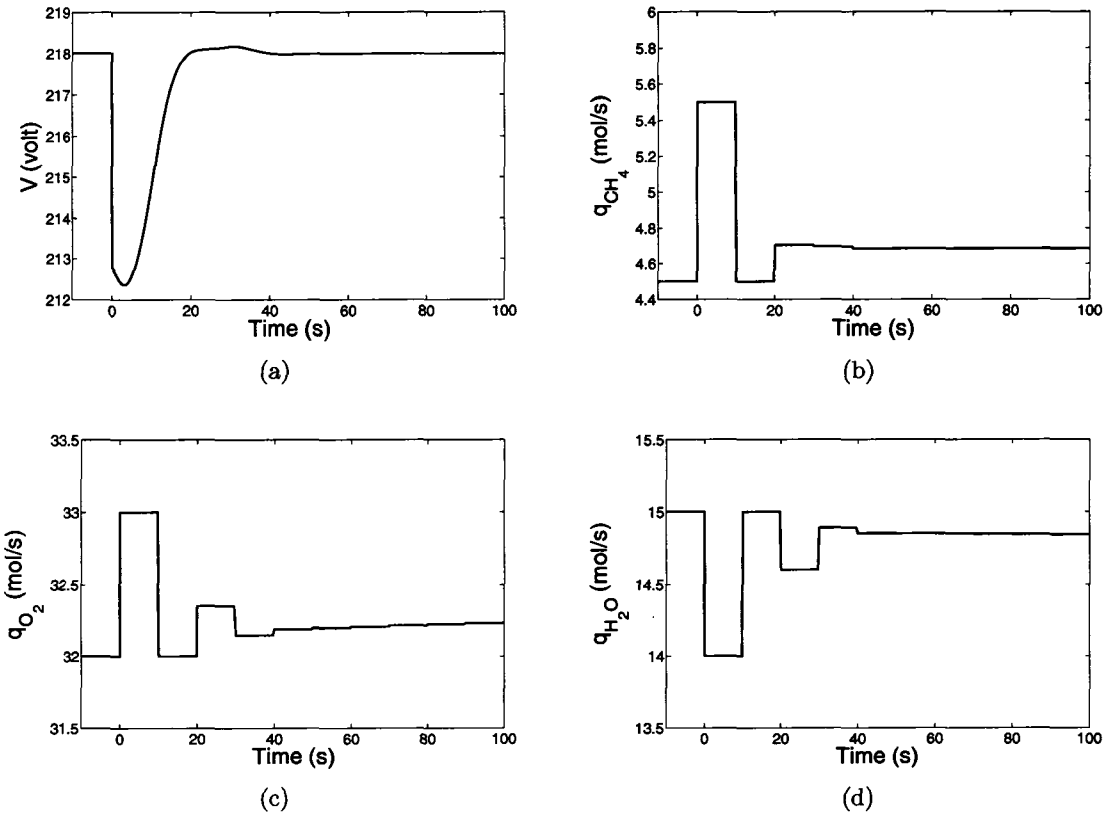

Figure 6.7: Response to a load change of 500 to 550 amp; Here, PH=10, CH=3, Ts=10 sec

around initial steady-state operating conditions corresponding to 500 amp load. The linearized model is then discretized by taking sampling interval $T_s = 1$ *sec.* This linearized and discretized model works well with linear MPC around its nominal operating condition. Since the settling time of the nonlinear fuel cell system model is approximately 500 seconds, the prediction horizon of only 10 second with linearized model is too short to control the system.

Linear MPC has then been applied to the fuel cell system by increasing the sampling interval from 1 to 10 second. This results in a longer prediction horizon (100 second) which could stabilize the system as shown in fig. 6.7. It is however noticed that it takes longer time and larger control effort for the linear MPC to control it even for a load disturbance of only 50 amp.

Even though LMPC can stabilize the system for a load change of 50 amp, it fails to control the system for higher load disturbances. This has motivated us to employ

nonlinear MPC which is not restricted by the operating region. The simulation results of nonlinear MPC are given in the following section.

6.5.2 Nonlinear MPC

Simulations have also been performed by applying nonlinear MPC on both stand-alone fuel cell and fuel cell system for different load changes to compare its performance with linear MPC. As mentioned earlier, the discretization of the nonlinear CT model is done by orthogonal collocation method and the unmeasured states are estimated by using unscented Kalman filter. In all cases, NMPC outperformed linear MPC in terms of load disturbance rejection. For NMPC, a sampling interval of $T_s = 1$ second with prediction and control horizon 5 and 2 respectively have been sufficient for controlling the system. Higher prediction and control horizon however took larger computational power and time, which is an inherent disadvantage of nonlinear MPC.

Fig. 6.8 shows the response of a stand-alone fuel cell connected in parallel with a capacitor for a series of step changes and the control actions taken by the nonlinear MPC.

Fig. 6.9 shows the voltage response and the control actions taken by NMPC for a step change of current demand from 300 to 500 amp. The output voltage and control actions settles down to their optimal values within 10 seconds.

Nonlinear MPC has also been applied to the fuel cell system along with capacitor for a series of step changes in the current demand. Fig. 6.10 shows the response of the fuel cell system and flow rates of methane, steam and oxygen (*i.e.*, air) as controlled by NMPC with prediction and control horizon 5 and 2 respectively. The sampling interval, in this case, is also kept at $T_s = 1$ second. It is noticed that even for the entire fuel cell system, NMPC can quickly bring the voltage to its target in 12 second.

The voltage response from the fuel cell system and control actions taken by NMPC are shown in fig. 6.11 for a step change in current demand from 300 amp to 500 amp.

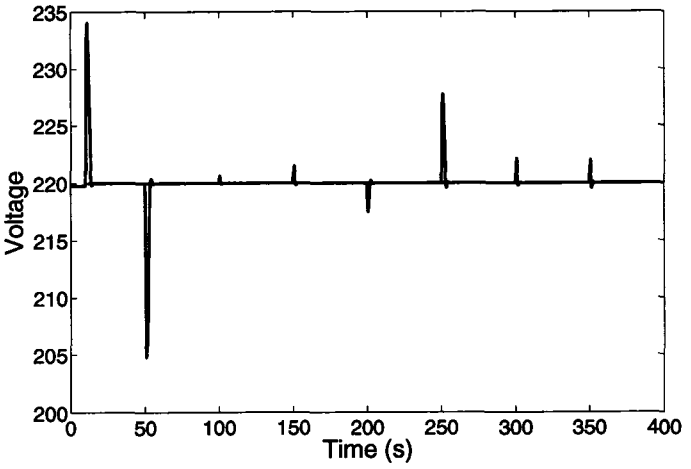

(a)

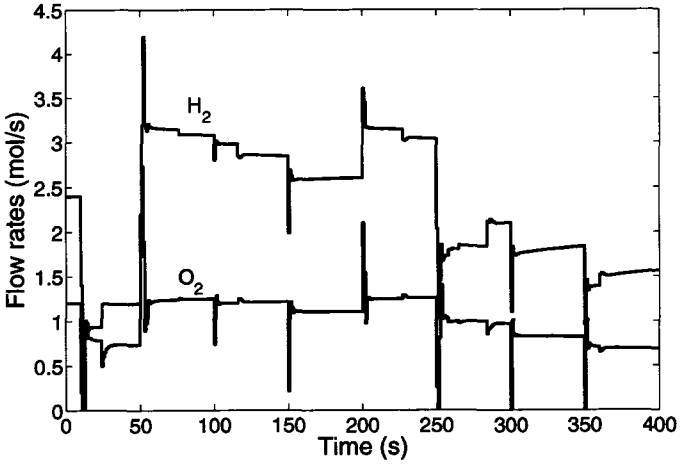

(b)

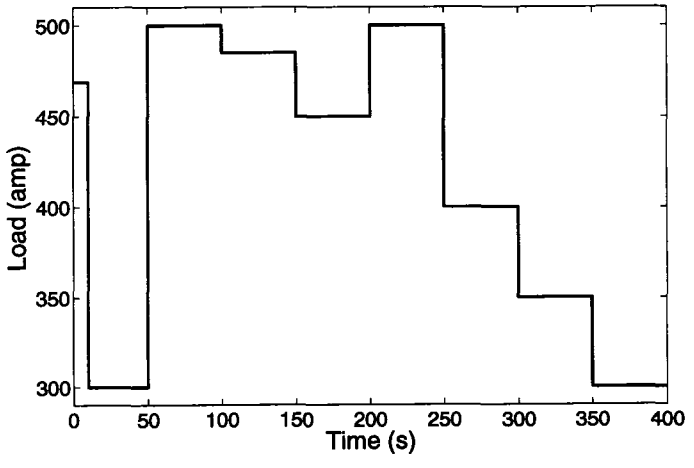

(c)

Figure 6.8: Stand-alone fuel cell along with capacitor

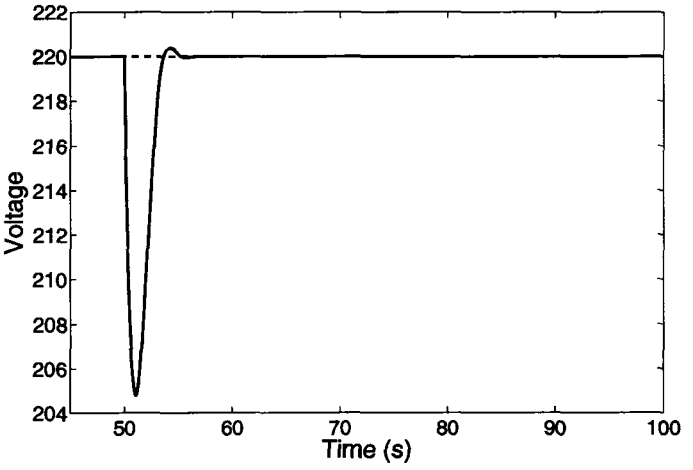

(a)

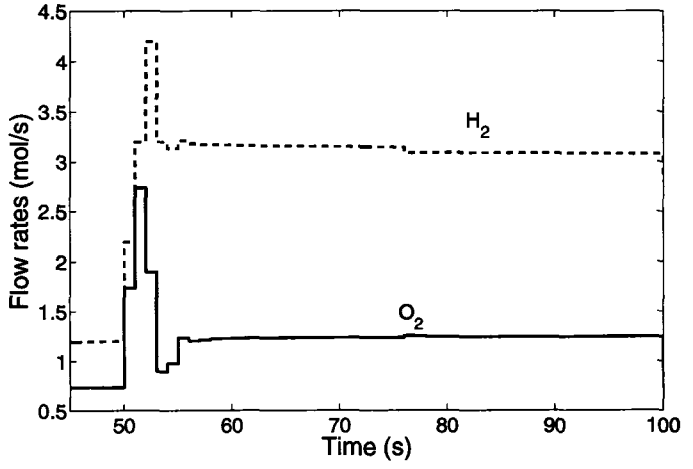

(b)

Figure 6.9: Close up shot of fig. 6.8

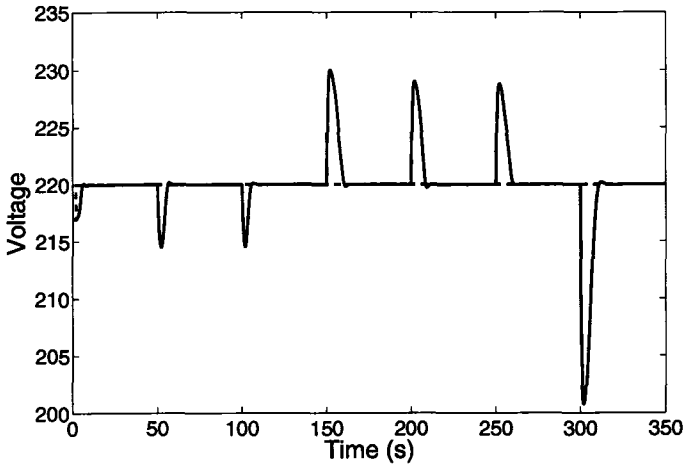

(a)

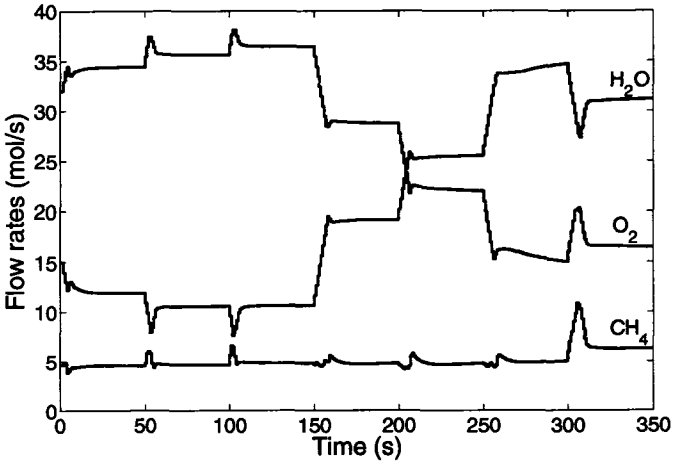

(b)

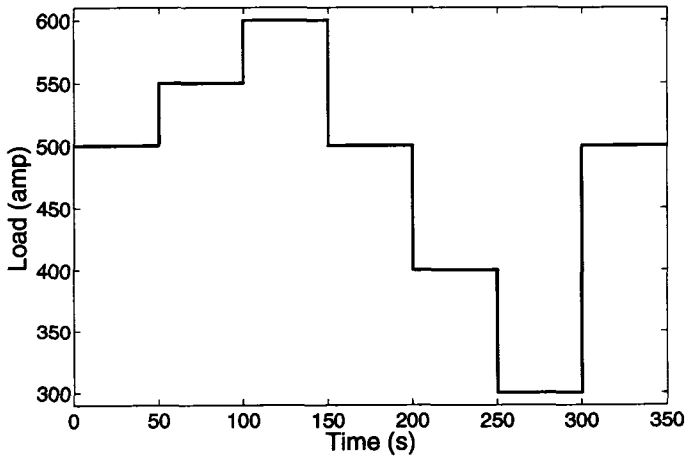

(c)

Figure 6.10: NMPC has been applied for load changes to a fuel cell system along with capacitor; Here, PH=5, CH=2, Ts=1 sec

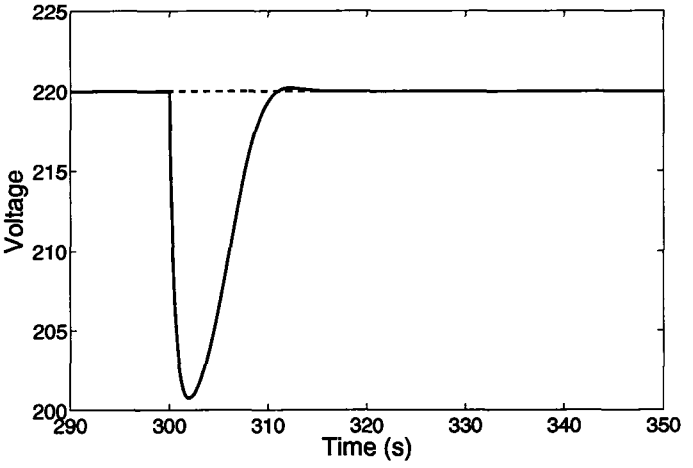

(a)

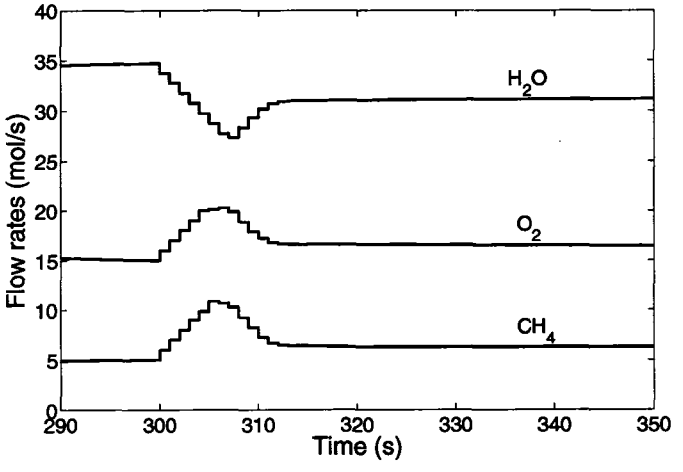

(b)

Figure 6.11: Close up shot of fig. 6.10

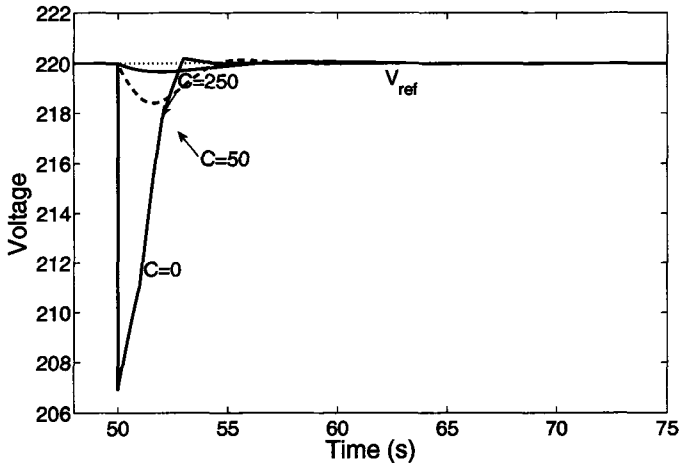

Figure 6.12: Transient response of a stand-alone fuel cell compared to a fuel cell connected in parallel to a 50 *farad* and a 250 *farad* capacitor controlled by NMPC with PH=5, CH=2, Ts=1 sec. Here, the current demand was increased from 500 to 600 *amp*

6.5.3 Effect of Capacitor

The effect of capacitor connected in parallel with a stand-alone fuel cell has been discussed in section 3.6. In this work, it has been shown that when capacitor and fuel cell are connected in parallel, the capacitor shares load from the sudden change in the current demand and thus smoothes the sudden drop or rise in the fuel cell stack voltage. The more the capacitance of the capacitor, the more it can share the current demand load. The fuel cell current and the stack voltage thus reach their final current demand with a behavior of first order response [see fig. 3.11(a), fig. 3.11(b), fig. 3.11(c)]. It is also expected that since there is no steep voltage drop, a controller connected with the fuel cell will be able to keep the voltage to its target value with fair ease.

Nonlinear MPC has been applied to a stand-alone fuel cell connected in parallel with capacitors of different capacitance. Fig. 6.5.3 shows the response from the fuel cell without any capacitor compared to those connected with 50 *farad* and 250 *farad* capacitors respectively. When the fuel cell is not connected with any capacitor, there is a steep voltage drop. But stack voltage deviates less from its targeted value with the increase of the capacitance. Fig. 6.13(a) and fig. 6.13(b) show the load shared by the fuel cell and the capacitor respectively for increase in the demand current.

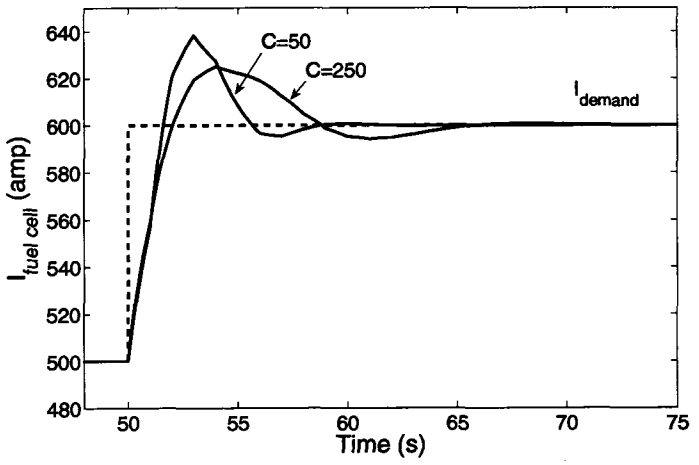

(a)

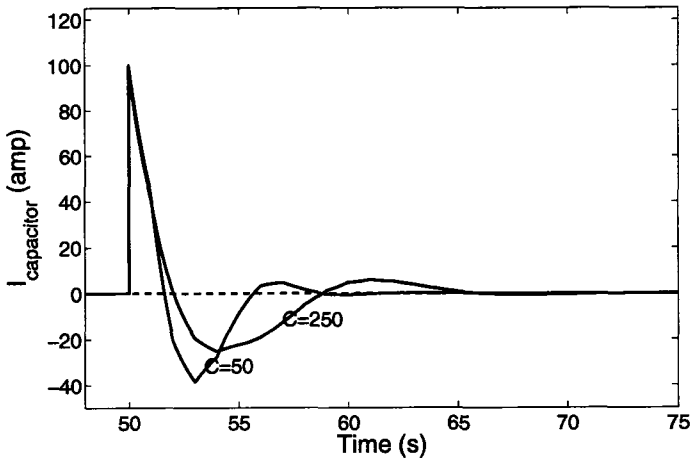

(b)

Figure 6.13: Load distribution between a fuel cell and a capacitor

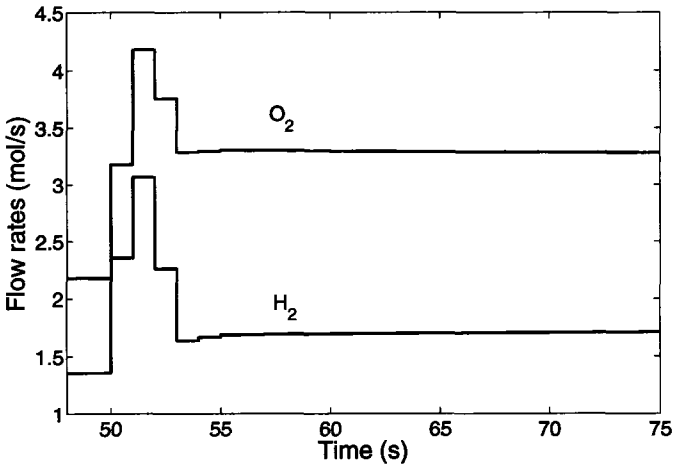

(a)

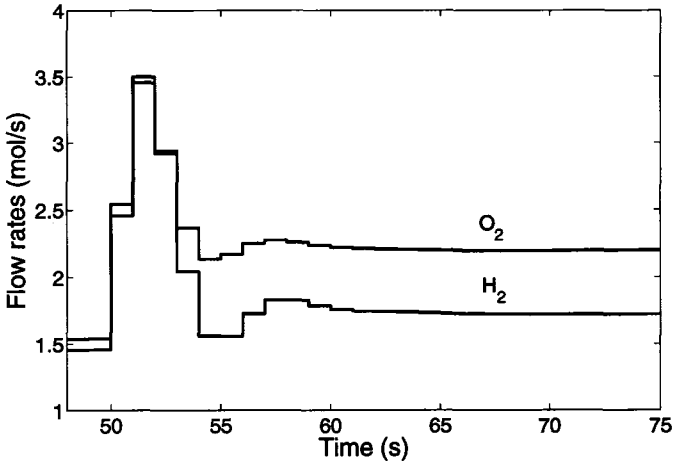

(b)

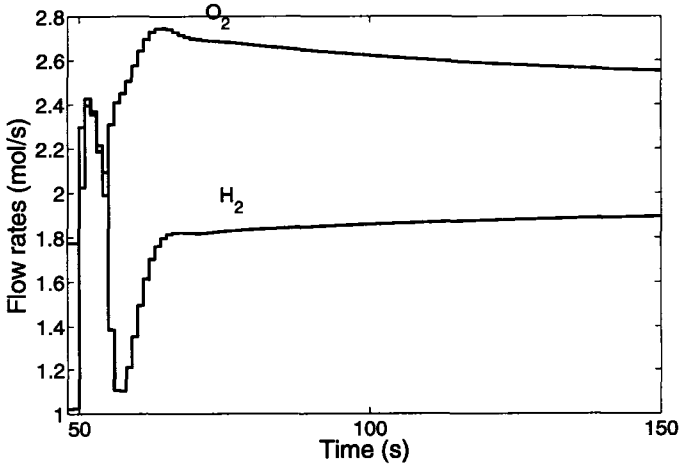

(c)

Figure 6.14: Control action taken by NMPC (a) for a stand-alone fuel cell, (b) for a fuel cell connected in parallel to a 50 *farad* capacitor (c) 250 *farad* capacitor

Table 6.1: Optimal fuel flows for minimum indirect energy

Demand current, I (amp)	Optimal flow rates (mol/s)				Optimal splitting ratio	Exhaust energy (KJ/amp)
	$\dot{n}_{CH_4}$	$\dot{n}_{O_2}$	$\dot{n}_{H_2O}$	$\dot{n}_{O_2,burner}$		
200	0.2272	0.7197	0.3327	0.2272	0.3365	1.1597
300	0.3579	1.1181	0.4165	0.3579	0.3298	1.2127
400	0.5465	1.8736	0.5111	0.5465	0.3411	1.4057
500	0.9322	4.1958	0.5863	0.9322	0.3990	2.0100
600	1.6756	14.9550	0.6690	1.6756	0.8165	4.1428

It is noticed that for higher capacitance, the settling time for fuel cell current is higher and thus the control actions taken by the controller has a lingering effect as shown in fig. 6.14.

6.5.4 Maximizing Direct Energy

The idea for running fuel cell system to produce maximum direct energy has been addressed in section 6.4. This formulation will be used to find a set of optimal inputs for different load distribution, which can be used as the reference inputs in NMPC objective function. The results are shown in table 6.1.

Fig. 6.15 and Fig. 6.17 depicts the response of NMPC for a step change of current demand from 500 amp to 600 amp with a simultaneous change in their corresponding reference inputs [table 6.1]. The system output quickly reaches its target. However, unlike previous response, the control actions taken by the nonlinear MPC match the optimal inputs at steady state.

It is evident from table 6.1 and fig. 6.10, that the consumption of methane for a demand current of 500 amp is much lower at minimal indirect energy than the 5 $kmol/s$ flow rate (approximately) when the system is not optimized. However, It is also noticed that the fuel flow rates are much higher at higher current demand compared to that of the lower current demand which is also evident from the efficiency of the optimization, defined as exhaust energy in KJ per amp of current load. The inefficient operation of fuel cell system at higher load is generated by the limitation of the reformer and the heat exchangers. These system components are designed to

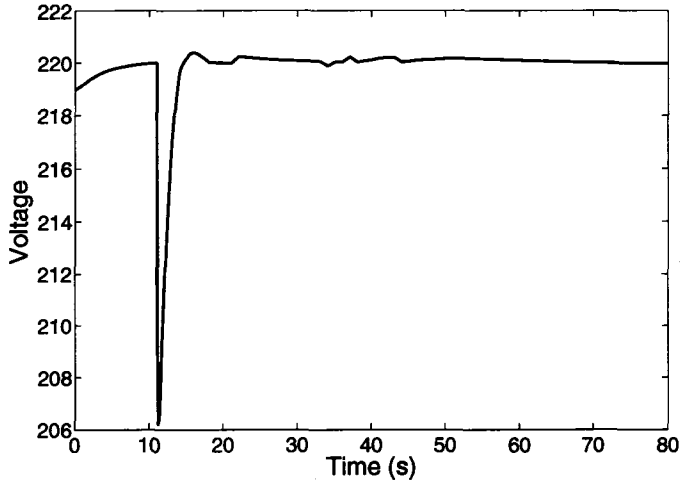

(a)

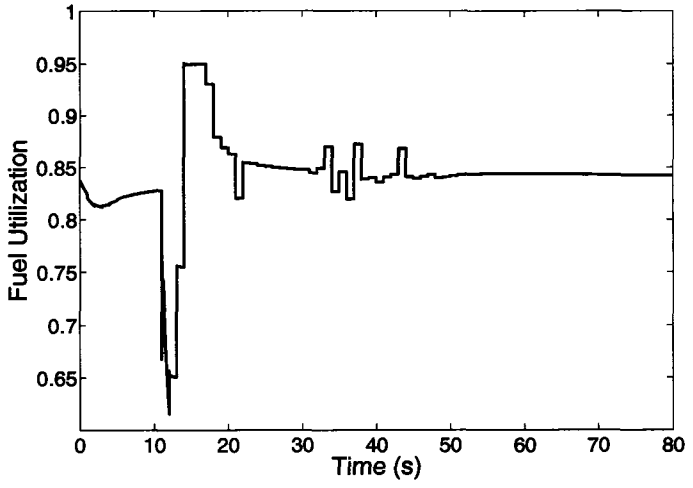

(b)

Figure 6.15: Response (a) voltage and (b) fuel utilization, to a load change of 500 amp to 600 amp with weights: $Q = 1$, $R = 10$, $S = 10$; Optimal steady state input targets from energy minimization has been applied here

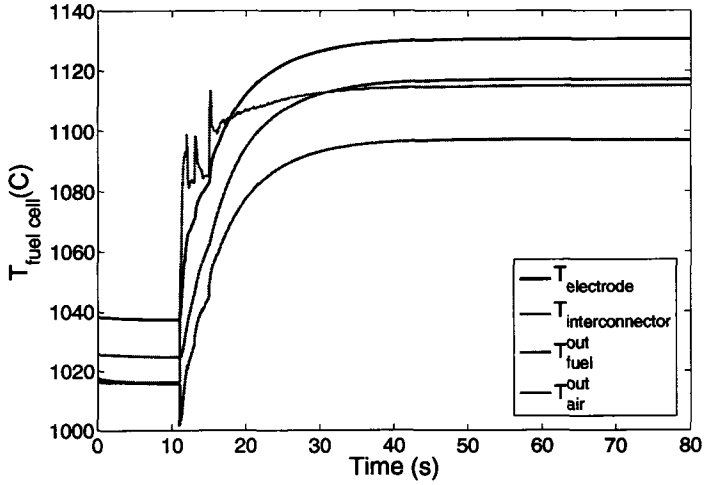

(a)

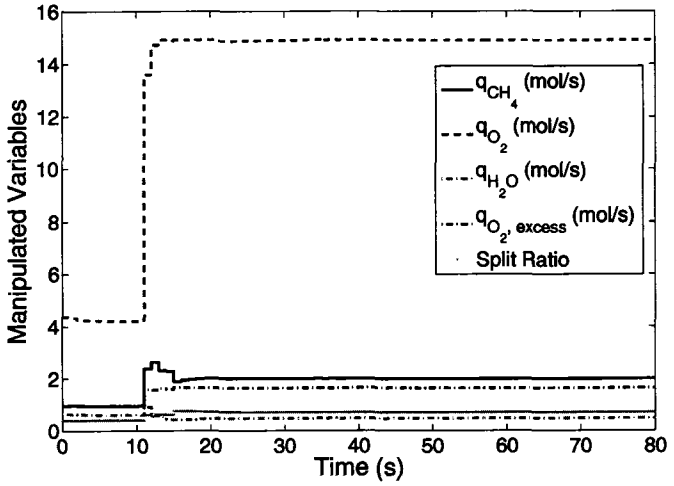

(b)

Figure 6.16: Response (a) Fuel cell temperature and (b) control inputs, to a load change of 500 amp to 600 amp with weights: $Q = 1$, $R = 10$, $S = 10$; Optimal steady state input targets from energy minimization has been applied here

Table 6.2: Sets of different steady state solution for different initial conditions

Demand current I (amp)	Set No.	Optimal flow rates (mol/s)				Optimal splitting ratio
		$\dot{n}_{CH_4}$	$\dot{n}_{O_2}$	$\dot{n}_{H_2O}$	$\dot{n}_{O_2,burner}$	
200	Set 1	6.0679	65.2014	8.1841	6.0679	0.5851
	Set 2	0.2272	0.7197	0.3327	0.2272	0.3365
300	Set 1	2.4745	22.7990	3.3505	2.4745	0.5406
	Set 2	0.3579	1.1181	0.4165	0.3579	0.3298
400	Set 1	1.0942	6.3157	1.4062	1.0942	0.4316
	Set 2	0.5465	1.8736	0.5111	0.5465	0.3411

operate at current load 200 to 300 amp. As the load is increased, the conversion rate of methane to hydrogen in the reformer is decreased. The unreacted methane in turn increases the temperature and the energy content of the exhaust gas. A reformer of higher capacity will reduce the inefficiency at higher load.

6.6 Issues

Several important issues need to be considered during the simulation and implementation of both steady-state optimizer and NMPC. Some of these issues are discussed in the following sections:

- **Initial Value:** Initial value is important for optimization algorithm in NMPC. If the initial state is too far away from the optimal point, the solution may become infeasible. Same is true for steady-state optimization.

  The solution from steady-state optimization is not unique. Depending on the initial guess, the steady-state solution may converge to different points - all of which satisfy the constraints and process operating conditions. Table 6.2 provides different steady-state solutions for same target load but with different initial guesses.

  It is not straightforward to decide which one of these solutions is optimal and, which one is sub-optimal. The optimal solution may be picked up in two ways. First, compare the final values of the objective functions, and choose the solution that is minimum. Second, set a target manipulated variable that is most economically viable, *e.g.*, fuel flow rate, and choose the solution with minimum

fuel flow rate. This can also be done by introducing penalty on fuel flow rate in the steady-state objective function. Mathematically, it can be written as:

$$\min_{U_s} \sum \dot{n}_{i,E} \int_{T_{ref}}^{T_{AE}} C_{p,i}(T)dT + \dot{n}_{i,E}\frac{1-r}{r}\int_{T_{ref}}^{T_B} C_{p,i}(T)dT + \|\dot{n}_{CH_4}\|_2^Q$$

subject to,

$$\begin{aligned} & f(X_s, U_s, W_s) = 0 \qquad \text{[steady-state model]} \\ & V_s = V_{ref} \\ & X_{min} < \hat{X}_s < X_{max} \quad \text{[NMPC constraints]} \end{aligned}$$

Choosing minimum flow rate has an inherent disadvantage though. If load is increased suddenly during the operation with minimal flow rate, the voltage might drop alarmingly, causing damage to the cell. One solution to this case is to use capacitor as an auxiliary power source, which has already been discussed.

- **Modeling:** The reformer model, as described in section 3.7.2, does not have any species dynamics associated with it. The model provides dynamic aspect of thermodynamic behavior of the reformer only. As a result, the flow rates of hydrogen and steam, produced by reforming and water-gas shift reaction, are affected dynamically by the slow dynamics of the reformer temperature only. This results in an almost instantaneous change in the flow rates with the change in the inlet flows of fuels. As a result, the estimated fuel utilization of the fuel cell also shows similar fast dynamic behavior in fig. 6.15(b). Similar situations arise due to the temperature-dynamics-only model of fuel heat exchanger, air heat exchanger, and the burner.

- **NMPC Tuning:** Tuning of NMPC is one of the most important factors for robust performance of the controlled system. A general guideline of MPC tuning has been addressed in section 4.1.2. The three main parameters in the NMPC objective function described by eqn. (4.8) are the output weight matrix Q, input weight matrix R, and the penalty matrix S on the deviation of the manipulated variables. Depending on the weights of these matrices, certain terms in the objective function may get more attention than the others.

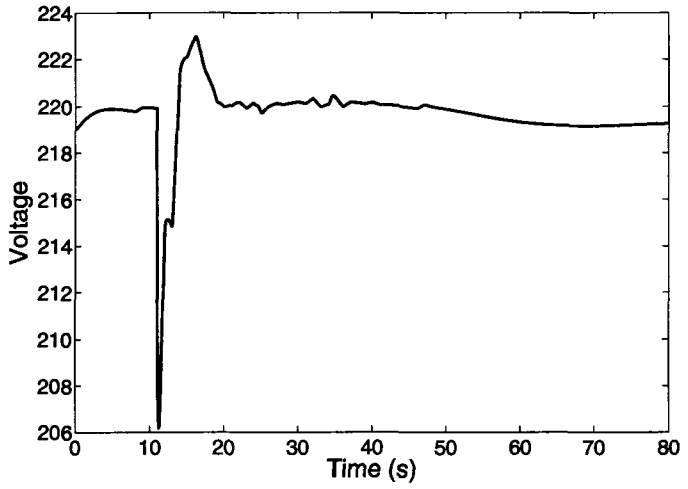

(a)

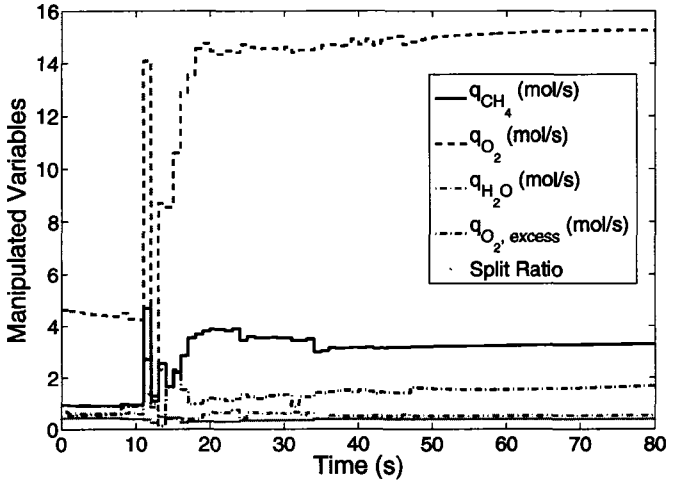

(b)

Figure 6.17: Response to a load change of 500 amp to 600 amp with weights: $Q = 1$, $R = 1$, $S = 1$; The steady state input targets from energy minimization has been applied here

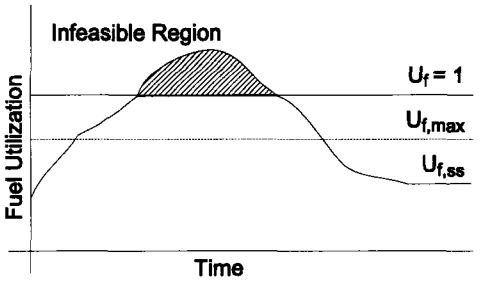

Figure 6.18: Constraint violation during online implementation of controller

For example, in our fuel cell simulation the output (voltage) is about 100 times larger in magnitude than the manipulated variables (flow rates in mol/s). Taking all the weights Q, R, and S as unit matrices results in less penalties on the manipulated variables. The consequence is more aggressive control actions and slow convergence of the manipulated variables to their steady state targets. This type of too much drastic action may some time lead to instability of the system.

This scenario is depicted in fig. 6.17. The weights for this simulation has been taken as $Q = 1$, $R = 1$, and $S = 1$. The controller makes large moves to quickly stabilize the system, which in turn results in more lingering disturbance in the system. More penalties on inputs and deviation on manipulated variables, on the other hand, results in slow but steady control actions as shown in fig. 6.15.

- **Steady-state vs. Dynamic Constraint:** In steady-state optimization, the attention is paid on the final value. But a feasible solution from steady-state optimization does not mean that it will always produce feasible solution during online implementation of the controller. This is schematically depicted in fig. 6.18. A set of feasible solutions for manipulated variables from steady-state optimization may guarantee fuel utilization of Uf=0.85 at steady state. When the same sets of manipulated variables are applied to the system during online implementation, this may lead to unstable behavior due to violation of the constraint (shaded area). But careful choice of constraints, such as a lower constraint limit below the critical value, and more degrees of freedom, usually solves the problem.

- **Steady-state vs. Dynamic Target:** Fuel utilization is defined as a ratio

of reacted hydrogen to input hydrogen. Thus lower fuel utilization leads to unreacted hydrogen out of the fuel cell and results in waste of energy. On the other hand, overused fuel will lead to fuel starvation and permanent damage to the cell. It is always recommended to operate the fuel cell at an optimal value of 0.85, but never exceeding 0.95 during transient operation.

The steady-state optimal inputs given in table 6.1 have been calculated with a target fuel utilization of 0.85. However, during the implementation of NMPC, fuel utilization has been taken as a constraint with an upper and lower limit of 0.95 to 0.05 respectively. This ensures more flexibility during the transient period, yet with guaranteed optimal fuel utilization at steady state.

6.7 Conclusion

The main objective of this work is to develop suitable controllers for stand-alone SOFC and SOFC system described by the models in chapter 3 where two sets of models are presented along with models of balance of plant (BOP) and necessary formulation of running fuel cell connected in parallel with a capacitor.

All of the described models are developed by first principle knowledge and thus posses the typical nonlinear, continuous time characteristics of first principle models. Both linear and nonlinear MPCs have been applied to the system in order to compare their performance. For linear MPC, MATLAB MPC toolbox has been used and thus discretization of the models and state estimation of the unmeasured states based on input-output data are not required. Implementation of nonlinear MPC however requires discretization, which is done by using the orthogonal collocation method. Unmeasured states, on the other hand, are estimated by unscented Kalman filter.

From the simulation, as well as from the inherent nature of the control, state estimation and discretization algorithms, the following conclusions can be drawn:

- **Linear MPC** works for simple nonlinear system near nominal operating conditions around which the linear model is approximated. In this work, linear MPC

Table 6.3: Comparison of linear and nonlinear model predictive control

	Linear MPC	Nonlinear MPC
Settling Time	$>$ 20 sec	$<$ 10 sec
Offset from setpoint	Yes, if load disturbance is higher than 50 *amp* from nominal operating conditions	No offset
Stability	Unstable, if load disturbance is higher than 50 *amp* from nominal operating conditions	Stable

works for small load disturbances fairly well. For load change of 50 amp, higher prediction and control horizon is required which can be done simply by increasing the time interval and thus reducing computation load. But for even higher load change, linear MPC fails to regulate the voltage to its reference point and eventually exhibits unstable behavior.

- **Nonlinear MPC** can control the system for larger load disturbances provided that it does not exceed the design capacity of the fuel cell system. The prediction and control horizon of NMPC can be small which in turn reduces computation power and time. In addition to depending on the complexity of the model, the computational loads of linear and nonlinear MPC also depend on the efficient coding style. In this work, linear MPC has been applied by using MATLAB MPC toolbox. On the other hand, nonlinear MPC has been coded by the author himself. Thus, a direct comparison of computational loads between the MPC toolbox of MATLAB and the coded nonlinear MPC by the author will not give a true account of the load. Instead, a comparison of linear and nonlinear MPC in terms of stability and performance is provided in table 6.3.

- **Orthogonal collocation method** is very efficient in converting nonlinear continuous time model to a set of nonlinear algebraic equations. This method does not require selection of node points and thus less prone to human-error. In addition, the algorithm can be directly fit into the MPC formulation.

- **Unscented Kalman filter (UKF)** can be used to estimate unmeasured states from input-output data. Unlike extended Kalman filter (EKF), UKF does not require Jacobean of the model and thus is fairly easy to implement. In addition, the accuracy of the state estimation is higher than EKF. Implementation of UKF

requires the discrete model, which again can be done by orthogonal collocation method, backward approximation or, by using MATLAB built-in ODE solvers. Tuning of UKF parameters however requires a bit of attention as discussed in section 4.3.3.

- **Maximizing direct energy** of the fuel cell system can be performed which, in turn, provides direction of running SOFC system with minimal fuel.

Chapter 7

A Linear Matrix Inequality Approach to Data-Driven Fault Detection

7.1 Introduction

Advanced controllers such as, nonlinear model predictive control can be used to maintain operation of complex systems like convective loop reactor and solid oxide fuel cell system more closely near the constraints. This results in an increase in profit and maintenance of stringent environmental regulations.

The performance of the controller, conventional or, advanced, however depends on the accuracy of the data collected. The instruments that are used for data collection may become faulty. In some cases, the faulty instrument may provide a bad data signal giving the operators to take unnecessary actions. In worst case scenario, the instrument may simply provide faulty data giving a false impression of an operating condition which is completely different from the actual one. The control actions, based on these data, may result in unsafe operation of the system. Naturally, fault detection and isolation of critical variables as well as the operating region is an important part of any automation process. Early detection of fault and isolation of the root cause can help avoid abnormal situation and reduce production loss.

Based on the nature of the underlying models, fault detection and identification

(FDI) techniques can be classified into three main categories: quantitative model-based, qualitative model-based and process history-based methods. The first principle models are obtained based on the physical understanding of the process including mass, energy and momentum balances as well as hard constraint of the processes. Due to the nonlinear nature of the most process models, this method is difficult to implement. In contrast, process history-based methods such as principal component analysis (PCA) only require process historical data. In this method, steady state process data are analyzed and used as *a priori* knowledge for diagnosis. It is a multivariate statistical technique, which utilizes first few principal components of the covariance matrix for capturing process variable correlation.

In this work a hybrid fault detection (HFD) framework is introduced, which formulates the fault detection problem as a linear matrix inequality (LMI) (Boyd et al. [18], Rajamoni and Ganguli [115]). Unlike the process history-based methods, the proposed framework can easily accommodate certain types of physical constraints known from process models. This capability of incorporating insightful knowledge into the process history makes the hybrid method more accurate and can help in the early detection of faults. It is further shown that the traditional PCA can be converted to the proposed framework to form a hybrid PCA (HPCA) method for fault diagnosis. The proposed HPCA method is validated by applying the framework on the industrial data as well as solid oxide fuel cell system.

The remainder of this chapter is organized as follows: In section 7.2 the general framework of residual test as an LMI is introduced, followed by a discussion on constraints in section 7.3, and worst case scenario and its solution in section 7.4. In section 7.5 traditional PCA is described and converted to the proposed framework. Updating requirement of the model data matrix is discussed in section 7.6. Results from simulated example and industrial data sets are presented in section 7.7. The framework has also been applied on stand-alone solid oxide fuel cell and fuel cell system for different faulty situations. The results are provided in section 7.8.

7.2 A General Framework

Consider a model:

$$\underline{y}_t = \mathbf{C}\underline{x}_t + \underline{e}_t \tag{7.1}$$

where $\underline{y}_t \in \Re^{m\times 1}$ is the current data sample, $\underline{x}_t \in \Re^{k\times 1}$ is the co-ordinates of the projection of $\underline{y}_t$ in the reduced subspace expanded by the columns of $\mathbf{C} \in \Re^{m\times k}$, and $\underline{e}_t \in \Re^{m\times 1}$ is the white noise sequence with a distribution of $\mathcal{N}(0, \mathbf{\Sigma}_e)$. It will be shown in section 7.5.2 that, this could be the same model as identified by a traditional PCA with the orthogonal property of $\mathbf{C}$ *i.e.*, $\mathbf{C}^T\mathbf{C} = \mathbf{I}$, where $\mathbf{I}$ is an identity matrix

.

The model with the fault can be written as,

$$\underline{y}_t = \mathbf{C}\underline{x}_t + \mathbf{C_f}\underline{f}_t + \underline{e}_t \tag{7.2}$$

where $\underline{f}_t$ and $\mathbf{C_f}$ are the fault and the effect of the fault respectively.

In principle, any faulty situation may be monitored through the following test:

$$\mathcal{H}_0 : \underline{\epsilon}_t = \underline{y}_t - \mathbf{C}\underline{x}_t \quad \sim \mathcal{N}(0, \mathbf{\Sigma}_\epsilon) \tag{7.3}$$

$$\text{vs. } \mathcal{H}_1 : \underline{\epsilon}_t = \underline{y}_t - \mathbf{C}\underline{x}_t \quad \sim \mathcal{N}(\mathbf{C_f}\underline{f}_t, \mathbf{\Sigma}_\epsilon) \tag{7.4}$$

where $\underline{\epsilon}_t$ is the residual. Here, $\mathcal{H}_0$ and $\mathcal{H}_1$ are the fault-free and faulty hypotheses respectively. This notation of the hypothesis test will be used throughout this paper.

Instead of checking the normality assumption for the residual under fault-free condition, the following quadratic form of the residual may also be checked:

$$Q_{SPE} = \underline{\epsilon}_t^T \mathbf{\Sigma}_\epsilon^{-1} \underline{\epsilon}_t \sim \chi_p^2(\alpha) \tag{7.5}$$

where p is the degrees of freedom for the Chi-square distribution and the residual covariance matrix, $\mathbf{\Sigma}_\epsilon$ is full ranked and invertible. However if $\mathbf{\Sigma}_\epsilon$ is not invertible then this test statistics cannot be used. For example if $\mathbf{C}$ is determined using traditional PCA then it can be shown that $rank(\mathbf{\Sigma}_\epsilon) \leq m-k$, where m and k are the dimensions of the original and reduced spaces respectively. To circumvent this problem, the

hypothesis may be changed to the following one:

$$\begin{aligned} \mathcal{H}_0 &: \ Q_{SPE} = \underline{\epsilon}_t^T \underline{\epsilon}_t \leq Q_\alpha \\ \mathcal{H}_1 &: \ \text{Otherwise} \end{aligned} \tag{7.6}$$

where Q_{SPE} and Q_α are the squared prediction error and the threshold respectively.

There are two ways to solve the above hypothesis test. The first one is to find the minimum Q_{SPE} and check it against the threshold. This is in fact a minimization problem defined as:

$$\min_{\underline{x}_t^*} J = (\underline{y}_t - \mathbf{C}\underline{x}_t^*)^T(\underline{y}_t - \mathbf{C}\underline{x}_t^*) \tag{7.7}$$

Clearly the solution of $\underline{x}_t^*$ is,

$$\underline{x}_{opt}^* = (\mathbf{C}^T\mathbf{C})^{-1}\mathbf{C}^T\underline{y}_t \tag{7.8}$$

and,

$$Q_{SPE,min} = J|_{x_{opt}^*} = [\underline{y}_t - \mathbf{C}(\mathbf{C}^T\mathbf{C})^{-1}\mathbf{C}^T\underline{y}_t]^T[\underline{y}_t - \mathbf{C}(\mathbf{C}^T\mathbf{C})^{-1}\mathbf{C}^T\underline{y}_t] \tag{7.9}$$

The explicit solution of this minimization problem is possible only if there is no other additional constraint. If $Q_{SPE,min} < Q_\alpha$, then accept H_0, i.e. no fault is detected. This is equivalent to saying that there exists a $\underline{x}_t$ such that eqn. (7.1) holds and therefore no fault is detected. The interpretation is similar to the traditional model based parity space approach to fault detection.

Second, the above test is also equivalent to finding a member $\underline{x}_t^*$ from the set S:

$$S := \{\underline{x}_t^* : Q_{SPE} \leq Q_\alpha\} \tag{7.10}$$

If there is no fault then S will not be an empty set and the optimal value $\underline{x}_{opt}^*$ must be a member of S. In other words, if S is not empty, then H_0 must be true. So, instead of finding $\underline{x}_{opt}^*$, the problem can be reformulated to finding any feasible solution $\underline{x}_t^*$ that satisfies the inequality $Q_{SPE} \leq Q_\alpha$. This framework for testing faults will make it flexible to include any additional constraints and reduce the computation time as well, since the optimization algorithm stops carrying out further calculation once it finds any member of the feasible set S. This is depicted in fig. 7.1. Hence the

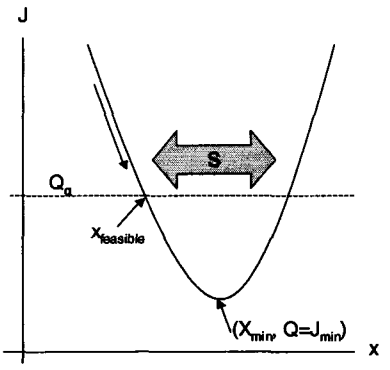

Figure 7.1: Physical interpretation of finding a feasible solution

fault-detection hypothesis can be stated as:

$$\begin{aligned} \mathcal{H}_0 &: \text{ If there exists } \underline{x}_t^* \text{ s.t.,} \\ &(\underline{y}_t - \mathbf{C}\underline{x}_t^*)^T(\underline{y}_t - \mathbf{C}\underline{x}_t^*) \leq Q_\alpha \qquad (7.11) \\ \mathcal{H}_1 &: \text{ Otherwise} \end{aligned}$$

Using Schur complement the above inequality can be written as a linear matrix inequality form:

$$\begin{bmatrix} Q_\alpha & (\underline{y}_t - \mathbf{C}\underline{x}_t^*)^T \\ \underline{y}_t - \mathbf{C}\underline{x}_t^* & \mathbf{I} \end{bmatrix} \geq 0 \qquad (7.12)$$

Expressing the fault detection criterion as an inequality problem has the added advantage of its capability to include constraints which is not possible in the traditional process history-based FDI methods such as PCA. If first principal knowledge of the processes like limiting values of the variables under investigation, or energy constraints are available, then these can easily be incorporated under the proposed framework such as:

$$\begin{bmatrix} Q_\alpha & (\underline{y}_t - \mathbf{C}\underline{x}_t^*)^T \\ \underline{y}_t - \mathbf{C}\underline{x}_t^* & I \end{bmatrix} \geq 0 \qquad (7.13)$$

$$A\underline{\hat{y}}_t \leq b_1 \qquad (7.14)$$

$$\underline{\hat{y}}_t^T \mathbf{R} \underline{\hat{y}}_t \leq b_2 \qquad (7.15)$$

$$A\underline{y}_t \leq b_3 \qquad (7.16)$$

where $\underline{\hat{y}}_t$ is the noise-free counterparts of $\underline{y}_t$, and A, $\mathbf{R}$, and b_i's are the constraint parameters and matrices containing first-principle process model parameters.

The capability to include additional constraints makes the proposed method a hybrid one including process data history and quantitative model based methods. The detailed algorithms of incorporating these additional constraints under the new framework are given in the following section.

7.3 Constraints

As stated earlier one of the main advantages of the proposed method is that it can incorporate certain types of inequality constraints in the algorithm. Formulation of the hypothesis tests of some of these inequality constraints is given next. These inequality constraints can be combined with residual test [eqn. (7.11)] to detect faults.

7.3.1 Constraints on the Noise-free Variables

$$\text{Process:} \qquad \underline{y}_t = \mathbf{C}\underline{x}_t + \underline{e}_t \tag{7.17}$$

$$\text{Model:} \qquad \underline{\hat{y}}_t = \mathbf{C}\underline{x}_t \tag{7.18}$$

$$\text{Constraints:} \qquad A\underline{\hat{y}}_t \leq b_1 \tag{7.19}$$

$$(\underline{\hat{y}}_t - \underline{a})^T\mathbf{R}(\underline{\hat{y}}_t - \underline{a}) \leq b_2 \tag{7.20}$$

The inequalities can be transformed to:

$$A\mathbf{C}\underline{x}_t \leq b_1 \tag{7.21}$$

$$(\mathbf{C}\underline{x}_t - \underline{a})^T\mathbf{R}(\mathbf{C}\underline{x}_t - \underline{a}) \leq b_2 \tag{7.22}$$

All these linear and quadratic inequalities can be transferred to LMIs.

The general quadratic constraint can be combined with the residual test in eqn. (7.11) to formulate an LMI problem as shown below:

H_0: There exists $\underline{x}_t^*$ s.t.,

$$\begin{aligned} &\begin{bmatrix} \bar{Q}_\alpha & (\underline{y}_t - \bar{\mathbf{C}}\underline{x}_t^*)^T \\ \underline{y}_t - \bar{\mathbf{C}}\underline{x}_t^* & I \end{bmatrix} \geq 0 \\ &A\mathbf{C}\underline{x}_t \leq b_1 \\ &(\mathbf{C}\underline{x}_t - \underline{a})^T\mathbf{R}(\mathbf{C}\underline{x}_t - \underline{a}) \leq b_2 \end{aligned} \tag{7.23}$$

7.3.2 Limiting Value Constraints on the Measured Variables

$$\text{Process:} \qquad \underline{y}_t = \mathbf{C}\underline{x}_t + \underline{e}_t \tag{7.24}$$

$$\text{Constraint:} \qquad \underline{A}\underline{y}_t \leq b_3 \tag{7.25}$$

The inequality in eqn. (7.25) represents certain process constraint such that, for example, the operating region of the process or the limiting value of the process measurements.

Since the disturbance is unknown, to incorporate this constraint we have to rely on probability tests. Under the probability framework the constraint may be considered as finding an inequality in terms of the reduced subspace variable $\underline{x}_t$ such that the probability $P(\underline{A}\underline{y}_t \leq b_3)$ is greater than a certain limiting value $1-\alpha$ *i.e.*, find a constraint on $\underline{x}_t$ such that

$$P(\underline{A}\underline{y}_t \leq b_3) \geq 1-\alpha \tag{7.26}$$

To this end, we note that the constraint in eqn. (7.25) can be expressed as:

$$\begin{aligned} & \underline{A}\mathbf{C}\underline{x}_t + \underline{A}\,\underline{\epsilon}_t \leq b_3 \\ \Rightarrow \quad & b_3 - \underline{A}\mathbf{C}\underline{x}_t \geq \underline{A}\,\underline{\epsilon}_t \quad \text{where, } \underline{A}\,\underline{\epsilon}_t \sim \mathcal{N}(0, \underline{A}\boldsymbol{\Sigma}_\epsilon \underline{A}^T) \\ \Rightarrow \quad & \frac{b_3 - \underline{A}\mathbf{C}\underline{x}_t}{\sqrt{\underline{A}\boldsymbol{\Sigma}_\epsilon \underline{A}^T}} \geq \frac{\underline{A}\,\underline{\epsilon}_t}{\sqrt{\underline{A}\boldsymbol{\Sigma}_\epsilon \underline{A}^T}} \end{aligned} \tag{7.27}$$

Here the standardized variable $z \triangleq \frac{\underline{A}\epsilon_t}{\sqrt{\underline{A}\boldsymbol{\Sigma}_\epsilon \underline{A}^T}}$ is distributed as $\mathcal{N}(0,1)$, and the $(1-\alpha)$ probability of its being greater than or equal to a critical value z_α can be written as:

$$P\left(\frac{\underline{A}\epsilon_t}{\sqrt{\underline{A}\boldsymbol{\Sigma}_\epsilon \underline{A}^T}} \leq z_\alpha\right) = 1-\alpha \tag{7.28}$$

The value of z_α for standard normal distribution data can be found from a normal distribution table.

Hence the probability inequality in eqn. (7.26) can now be expressed as:

Find a constraint on $\underline{x}_t$ such that

$$P\left(\frac{b_3 - \underline{A}\mathbf{C}\underline{x}_t}{\sqrt{\underline{A}\boldsymbol{\Sigma}_\epsilon\underline{A}^T}} \geq \frac{\underline{A}\epsilon_t}{\sqrt{\underline{A}\boldsymbol{\Sigma}_\epsilon\underline{A}^T}}\right) \geq 1-\alpha \tag{7.29}$$

Clearly if let

$$\frac{b_3 - \underline{A}\mathbf{C}\underline{x}_t}{\sqrt{\underline{A}\boldsymbol{\Sigma}_\epsilon\underline{A}^T}} \geq z_\alpha \tag{7.30}$$

then

$$\begin{aligned} P\left(\frac{\underline{A}\epsilon_t}{\sqrt{\underline{A}\boldsymbol{\Sigma}_\epsilon\underline{A}^T}} \leq \frac{b_3 - \underline{A}\mathbf{C}\underline{x}_t}{\sqrt{\underline{A}\boldsymbol{\Sigma}_\epsilon\underline{A}^T}}\right) \\ \geq P\left(\frac{\underline{A}\epsilon_t}{\sqrt{\underline{A}\boldsymbol{\Sigma}_\epsilon\underline{A}^T}} \leq z_\alpha\right) \\ \Rightarrow P\left(\frac{\underline{A}\epsilon_t}{\sqrt{\underline{A}\boldsymbol{\Sigma}_\epsilon\underline{A}^T}} \leq \frac{b_3 - \underline{A}\mathbf{C}\underline{x}_t}{\sqrt{\underline{A}\boldsymbol{\Sigma}_\epsilon\underline{A}^T}}\right) \geq 1-\alpha \\ \Rightarrow P(\underline{A}\underline{y}_t \leq b_3) \geq 1-\alpha \end{aligned} \tag{7.31}$$

Hence under the significance level of α, constraint in eqn. (7.25) can be satisfied through the inequality in eqn. (7.30). Then the fault detection with inequality constraint [eqn. (7.25)] can be expressed as:

If there exists $\underline{x}_t^*$ s.t.,

$$\begin{aligned} \begin{bmatrix} Q_\alpha & (\underline{y}_t - \mathbf{C}\underline{x}_t^*)^T \\ \underline{y}_t - \mathbf{C}\underline{x}_t^* & I \end{bmatrix} \geq 0 \\ \frac{b_3 - \underline{A}\mathbf{C}\underline{x}_t^*}{\sqrt{\underline{A}\boldsymbol{\Sigma}_\epsilon\underline{A}^T}} \geq z_\alpha \end{aligned} \tag{7.32}$$

which is once again the LMI problem.

7.4 Geometric Interpretation

The geometric interpretation of the residual hypothesis test given in eqn. (7.11) can be explained further by fig. 7.2. If a cone is drawn extended from the current measurement, $\underline{y}_t$, on the plane defined by $\mathbf{C}$ with inclined length equal to Q_α, then the intersection of the cone and the C-plane will create a circle on the C-plane. If $\underline{y}_t$ is

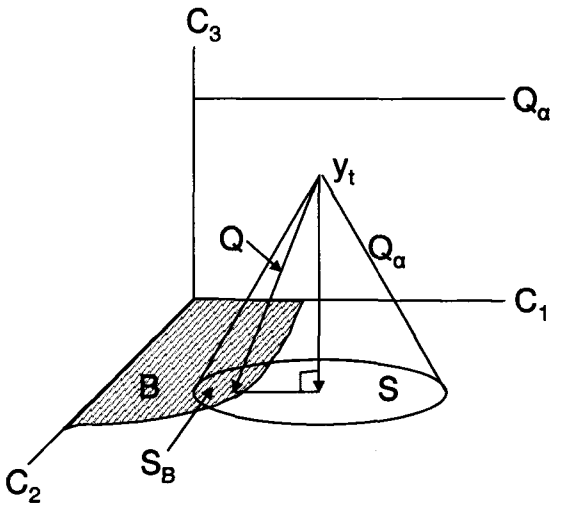

Figure 7.2: Physical interpretation of residual test

closer to the C-plane then the circle becomes larger and in limiting case converges to a circle with radius Q_α. Any oblique projection onto the area within and on the circle from $\underline{y}_t$ will satisfy the inequality in eqn. (7.11), since the residual of the oblique projection $Q_{SPE} \leq Q_\alpha$. So the set S can now be defined by this base circle and the optimal solution of $\underline{x}_t$ will be the projection of $\underline{y}_t$ onto the center of the circle. Therefore, the LMI feasibility test [eqn. (7.11)] of the residual can now be defined as to finding whether the cone intersects the C-plane. Now consider another inequality constraint, set B, along with the residual constraint, set S, as depicted in fig. 7.2. Even though the orthogonal projection of $\underline{y}_t$, the center of the circle, may be out of bound of the inequality constraint B, the set of feasible solutions $S_B := \{S \cap B\}$ is not empty. Hence the LMI feasibility test will not pick up the violation of the inequality constraint *i.e.*, no fault is detected. Therefore, the test is more robust to the disturbances/model uncertainty but as a result less sensitive to the fault.

If, however, one performs the orthogonal projection, then S shrinks to one point (if the cone and the C-plane has intersection). A fault will be detected as long as this point does not fall into B. Therefore, the test based on orthogonal projection is more sensitive to the fault but is also less robust to the disturbances/model uncertainty. The orthogonal projection can be easily included into the proposed LMI test by

introducing a orthogonality constraint:

$$(\underline{y}_t - \mathbf{C}\underline{x}_t)^T\mathbf{C} = 0 \tag{7.33}$$

Clearly, the two constraint LMI tests have their advantage and disadvantage in terms of their sensitivity to the fault and disturbance/model uncertainty. Alternative choice would be somewhere in between. Rather than constraining the test to the perfect orthogonality, the test may be defined as:

If there exists $\underline{x}_t^*$ s.t.,

$$|(\underline{y}_t - \mathbf{C}\underline{x}_t^*)^T\mathbf{C}| \leq \xi\underline{1}_{1\times k} \tag{7.34}$$

or if there exists $\underline{x}_t^*$ s.t.,

$$\|(\underline{y}_t - \mathbf{C}\underline{x}_t^*)^T\mathbf{C}\| \leq \xi \tag{7.35}$$

which provides freedom to tune the sensitivity of the monitoring algorithm by choosing ξ. Here, $\underline{1}_{1\times k} = [1, 1, \ldots, 1] \in \Re^{1\times k}$. $|\cdot|$ and $\|\cdot\|$ are the absolute value and second order norm of $(\cdot)$ respectively. This is equivalent to constraining the angle of the cone to the neighborhood of the orthogonal projection if so desired.

The feasibility tests defined in eqn. (7.23) and eqn. (7.32) can now be combined with the orthogonality constraint for detecting faults as expressed in eqn. (7.36) and eqn. (7.37).

Constraint in the noise-free variables:

If there exists $\underline{x}_t^*$ s.t.,

$$\begin{aligned} \|(\underline{y}_t - \mathbf{C}\underline{x}_t^*)^T\mathbf{C}\| &\leq \xi \\ A\mathbf{C}\underline{x}_t &\leq b_1 \\ (\mathbf{C}\underline{x}_t - \underline{a})^T\mathbf{R}(\mathbf{C}\underline{x}_t - \underline{a}) &\leq b_2 \end{aligned} \tag{7.36}$$

Constraint in the measured variables:

If there exists $\underline{x}_t^*$ s.t.,

$$\begin{aligned} \|(\underline{y}_t - \mathbf{C}\underline{x}_t^*)^T\mathbf{C}\| &\leq \xi \\ \frac{b - \underline{A}\mathbf{C}\underline{x}_t^*}{\sqrt{\underline{A}\mathbf{\Sigma}_\epsilon\underline{A}^T}} &\geq z_\alpha \end{aligned} \tag{7.37}$$

7.5 Hybrid PCA as a special case of hybrid fault detection (HFD)

The main objective of PCA is to find orthogonal spaces of a lower dimension which can describe the original data set without losing much information. It is based on the orthogonal decomposition of the covariance matrix of the original data set. Since data are projected to a low dimension, they can be easily monitored for unusual events rather than monitoring original variables of larger dimension.

7.5.1 Traditional PCA revisited

Consider a data set $\mathbf{Y} = [\underline{Y}_1, \underline{Y}_2, \ldots, \underline{Y}_m] \in \Re^{n \times m}$, where n and m are total numbers of samples and variables respectively. Then the idea is to find uncorrelated variables $\underline{X}_1, \underline{X}_2, \ldots, \underline{X}_m$ (named as principal components) such that the first few principal components account for the most variability in $\mathbf{Y}$. Mathematically this can be written as a problem of finding $\underline{X}_i$'s defined as a linear combination of the original variables.

It can be shown that the original variables can be written as:

$$\mathbf{Y} = \underline{X}_1 \underline{C}_1^T + \underline{X}_2 \underline{C}_2^T + \ldots + \underline{X}_m \underline{C}_m^T \tag{7.38}$$

where the vectors $\underline{C}_i$'s are the eigenvectors of the covariance $\mathbf{\Sigma}_Y$ of the original data matrix $\mathbf{Y}$ corresponding to its eigenvalues $\lambda_1 \geq \lambda_2 \geq \ldots \geq \lambda_m \geq 0$. In general first k principal components can account for the most variability of the data and thus the model can be written in terms of the reduced space $\mathbf{X} = [\underline{X}_1, \underline{X}_2, \ldots, \underline{X}_k]$ as:

$$\mathbf{Y} = \mathbf{X}\mathbf{C}^T + \mathbf{E} \tag{7.39}$$

where $\mathbf{C} = [\underline{C}_1, \underline{C}_2, \ldots, \underline{C}_k] \in \Re^{m \times k}$.

7.5.2 Fault detection using Traditional PCA

For a new sample $\underline{y}_t = [y_1, y_2, \ldots, y_m]^T$, the model can be written in terms of the reduced orthogonal space spanned by the columns of $\mathbf{C}$, as:

$$\text{Model: } \underline{y}_t = \mathbf{C}\underline{x}_t + \underline{e}_t \tag{7.40}$$

where $\underline{x}_t = [x_1, x_2, \ldots, x_k]^T \in \Re^{k\times 1}$ and $e_t \in \Re^{m\times 1}$. The projection of the new data sample $\underline{y}_t$ can then be calculated using the orthogonal property of $\mathbf{C}$ *i.e.*, $\mathbf{C}^T\mathbf{C} = \mathbf{I}$:

$$\underline{x}_t = \mathbf{C}^T\underline{y}_t \tag{7.41}$$

It is to be noted that this is the same solution as described in eqn. (7.8):

$$\underline{x}_t = (\mathbf{C}^T\mathbf{C})^{-1}\mathbf{C}^T\underline{y}_t = \mathbf{C}^T\underline{y}_t \tag{7.42}$$

This new sample can then be monitored using Hottellings' T^2-statistics for abnormal operating region data and Q-statistics (squared prediction error of the residual subspace) for checking the deviation of the data from the reduced space.

7.5.2.1 Hottellings' T^2-statistics

The Hottellings' T^2-statistics for the reduced space is defined as:

$$T^2 = \underline{x}_t^T\mathbf{L}^{-1}\underline{x}_t \sim \chi_k^2(\alpha) \tag{7.43}$$

where $\mathbf{L} = diag(\lambda_1, \lambda_2, \ldots, \lambda_k)$. Then detection of abnormal operating region data can be done by calculating Hottellings' T^2-statistics and comparing it with the threshold $\chi_k^2(\alpha)$.

7.5.2.2 Q-statistics

From the model of the system the residual can be written as:

$$\underline{\epsilon}_t = \underline{y}_t - \mathbf{C}\underline{x}_t \tag{7.44}$$

The Q-statistics or the squared prediction error (SPE) is defined as:

$$Q_{SPE} = \underline{\epsilon}_t^T\underline{\epsilon}_t = (\underline{y}_t - \mathbf{C}\underline{x}_t)^T(\underline{y}_t - \mathbf{C}\underline{x}_t) \tag{7.45}$$

Then the detection of deviation of the new data sample from the reduced space can be done by comparing Q_{SPE} with its threshold [eqn. (7.6)], which is given as follows (Jackson and Mudhokar [65]):

$$Q_\alpha = \theta_1\left[1 + \frac{h_0 c_\alpha\sqrt{2\theta_2}}{\theta_1} + \frac{\theta_2 h_0(h_0-1)}{\theta_1^2}\right]^{\frac{1}{h_0}} \tag{7.46}$$

where $\theta_i = \sum_{j=k+1}^{m}\lambda_j^i$, $h_0 = 1 - \frac{2\theta_1\theta_3}{3\theta_2^2}$ and c_α is the normal critical value at $(1-\alpha)\%$ probability.

7.5.3 Hybrid PCA

While it is easy to calculate the Hottellings' T^2-statistics and Q-statistics for monitoring future data sample, it is not possible to introduce additional constraints in the model that comes from first principal knowledge of the process. To include such type of situations, the PCA algorithm should be posed as a hybrid framework as discussed in section 7.2.

The Q-statistics test under the HFD Framework can be expressed as the following hypothesis test:

$$\begin{aligned} &\mathcal{H}_0 : \text{If there exists } \underline{x}_t^* \text{ such that,} \\ &\qquad (\underline{y}_t - \mathbf{C}\underline{x}_t^*)^T(\underline{y}_t - \mathbf{C}\underline{x}_t^*) \leq Q_\alpha \\ &\mathcal{H}_1 : \text{Otherwise} \end{aligned} \tag{7.47}$$

It is noted that $\underline{x}_t^*$ from the above formulation may not equal to the optimal value $\underline{x}_{opt} = \underline{x}_t$ found from the traditional PCA. But if there exists $\underline{x}_t^* \in S$ such that S is not empty, then there will be a guarantee to have $\underline{x}_{opt}$ for which $Q_{SPE} = Q_{SPE,min} \leq Q_\alpha$.

The Hottellings' T^2-statistics test can be expressed under the proposed framework as the following hypothesis test:

$$\begin{aligned} &\mathcal{H}_0 : \text{If there exists } \underline{x}_t^* \text{ such that,} \\ &\qquad \underline{x}_t^{*T}\mathbf{L}^{-1}\underline{x}_t^* \leq \chi_k^2(\alpha) \\ &\qquad \|(\underline{y}_t - \mathbf{C}\underline{x}_t^*)^T\mathbf{C}\| \leq \xi \\ &\mathcal{H}_1 : \text{Otherwise} \end{aligned} \tag{7.48}$$

where $\chi_k^2(\alpha)$ is the Chi-square critical value with k degrees of freedom and a confidence level α. The reason to include the orthogonal constraint in this case is due to the fact that PCA is based on the orthogonal projection.

Finally, by considering other constraints, HPCA may be formulated by the following

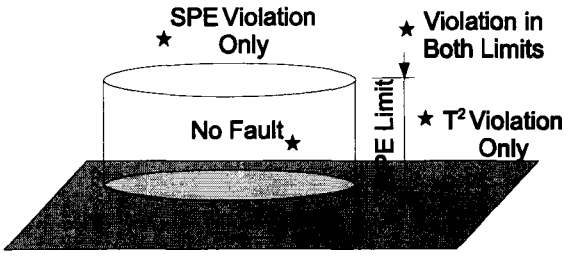

Figure 7.3: Schematic diagram of linear process and PCA framework

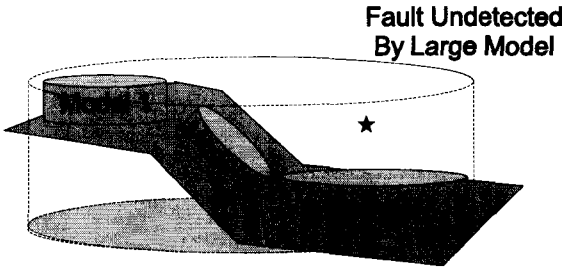

Figure 7.4: Schematic diagram of nonlinear process and PCA framework

LMI problem:

$$\begin{aligned} &(\underline{y}_t - \mathbf{C}\underline{x}_t^*)^T(\underline{y}_t - \mathbf{C}\underline{x}_t^*) \leq Q_\alpha \\ &\underline{x}_t^{*T}\mathbf{L}^{-1}\underline{x}_t^* \leq \chi_k^2(\alpha) \\ &\|(\underline{y}_t - \mathbf{C}\underline{x}_t^*)^T\mathbf{C}\| \leq \xi \\ &\text{Other linear or quadratic constraints} \end{aligned} \tag{7.49}$$

7.6 Moving Horizon Model Update

Both the traditional PCA and the proposed hybrid framework relies on the steady-state operating data of the process and are valid for linear systems. Any fault in the linear process can be easily captured by the proposed method. For example, fault in one of the model variable will result in invalid model structure and will be captured by SPE violation. On the other hand, if the current operating point falls outside the bounds of the model, T^2 limit will be violated. Thus including more valid operating points will increase the reliability and fault detection capability of the framework. This is depicted in fig. 7.3.

For dynamic nonlinear process, the scenario is different. When the process moves

to a new operating region, the old PCA model becomes invalid. Inclusion of more operating point into the model similar to linear case, however, does not solve the problem. Rather, it introduces large SPE limit, making it difficult to detect fault. This is depicted in fig. 7.4. The current operating point represented by star($\star$) is not detected by a single large linear model encompassing all the operating regions under consideration. Whereas if the PCA model is updated from "Model 1" to "Model 3", it will be able to detect the fault.

This particular problem of nonlinearity can be overcome by employing several methods - ranging from nonlinear PCA, multiple model technique, moving horizon technique to adaptive PCA. In this work, moving horizon technique has been employed to address the nonlinearity issues of solid oxide fuel cell system for fault detection and isolation. In this technique, the model data matrix is updated continuously or, based on some predefined criterion such as Hottellings' T^2, since it gives hint about changing operating conditions. In this criterion, whenever T^2 crosses its limit, the model is updated by including the new point and purging the oldest point from the model data matrix. Moving horizon update poses a certain problem though. Since it does not differentiate between faulty situations and change in operating conditions, it will detect fault, and then adapt the model to include the faulty situation. Eventually, it will make the scheme hard to detect similar faults in series. Thus it is best to update the model based on experience, rather than completely relying on statistical criterion. In this work, both continuous and Hottellings' T^2 based moving horizon update have been applied on the fuel cell system during open loop dynamic simulation, as well as, during controlling the system by employing nonlinear model predictive control. The results are given in section 7.8.

7.7 Illustrative Example

To test the proposed algorithm, a data set $\mathbf{Y} = [\underline{Y}_1, \underline{Y}_2, \underline{Y}_3]$ is generated so that the following relationship holds:

$$y_3 = 2y_1 + 5y_2 + 0.2e \tag{7.50}$$

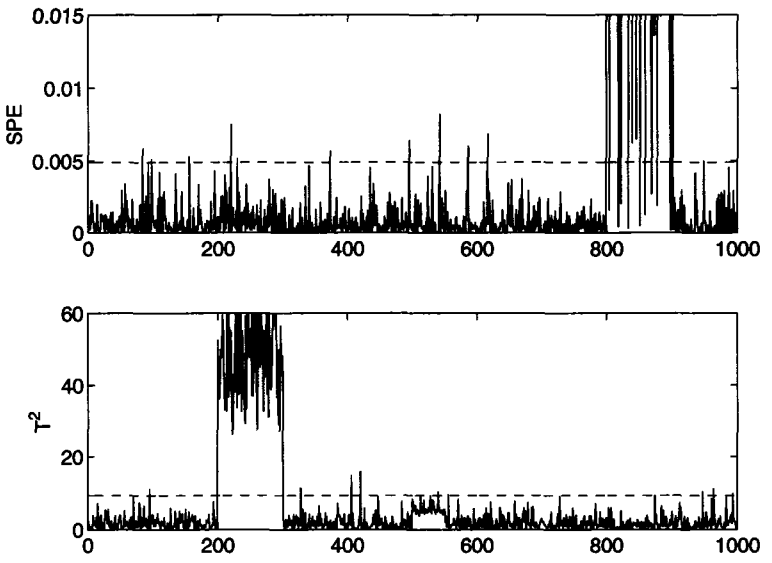

Figure 7.5: SPE and T^2 plots from traditional PCA

where y_1, y_2 and e are distributed as $\mathcal{N}(0,1)$. The model parameter $\mathbf{C}$ in eqn. (7.1) is calculated using traditional PCA. New data points are generated independent of the model data matrix with bias in y_1 and y_2 from samples $(200-300)$ and $(500-550)$ respectively. Data are also generated so that the model structure as stated in eqn. (7.50) does not hold between samples $(800-900)$. The faults between samples $(200-300)$ and $(800-900)$ can be captured by both the traditional PCA model and the proposed HFD framework as shown in the T^2 and SPE plots of fig. 7.5 and fig. 7.6. On the other hand, the bias in y_2 between samples $(500-550)$ can not be picked up by the T^2 plots of both frameworks. However it can be picked up by setting an upper limit constraint for the noise-free variable $\hat{y}_2$ in the proposed method as shown in fig. 7.7. In the simulations, if two consecutive points come as infeasible then those are marked as infeasible problem and given the value 1. Otherwise they are branded as outliers and assigned the value 0, i.e., no warning is issued. For feasible situation its value is 0, i.e. no alarms.

7.8 Monitoring SOFC System

Fault detection capability of both the traditional PCA and hybrid PCA is tested by applying them both on the fuel cell and its system. In all cases, the initial data

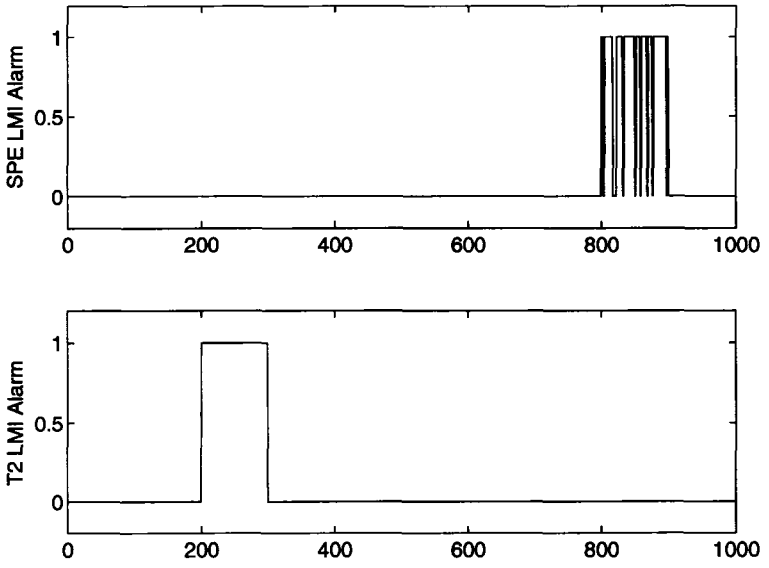

Figure 7.6: SPE and T^2 alarms from HFD

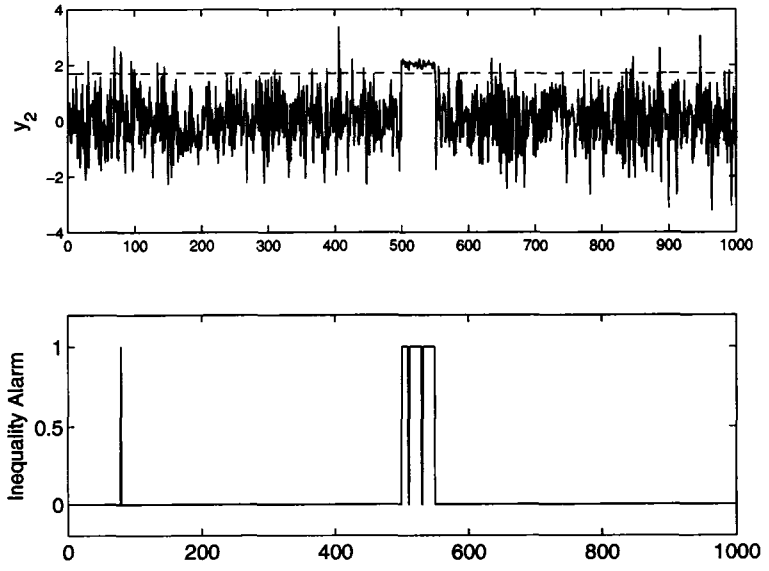

Figure 7.7: Constraint violation alarm from HFD

matrices have been built from steady state process data of key variables. The cleaned and normalized data matrices are then used to calculate statistical limits and principal components such that 90% variability of the process data is captured.

As discussed earlier, the hybrid PCA is presented as a linear matrix inequality problem so that physical and operating constraints such as fuel utilization, pressure, temperature and stack voltage can also be included in the proposed fault detection scheme. The constraints on the operating conditions are converted to LMI by employing methods described in section 7.3.1 and section 7.3.2. The inequalities are solved by using optimization packages SeDuMi and YALMIP. In this work, SeDuMi has been used as a background solver and YALMIP as a front interface. Both the packages are written in MATLAB and are freely available under GNU license.

Different combinations of unsafe operating conditions and instrument faults are applied on the fuel cell system for comparing the performance of PCA and HPCA for both controlled and uncontrolled systems. Fault detection based on moving horizon update has also been considered. The simulation results are provided in the section below followed by a summary of result in table 7.1.

7.8.1 Stand-alone SOFC without Moving Horizon Update

Both fault detection schemes have first been applied on the stand-alone fuel cell without any moving horizon update of the models. The key variables that have been used for building PCA model data matrix include voltage, fuel utilization, current load and key flow and temperature variables. The initial model is selected such that the operating data covers current load of 300 to 500 amp. A pulse of 300 amp in the current has then been applied between time step 400 to 700. The deviation from normal operation is captured by both schemes as shown in fig. 7.8.

Same model has also been used for fault detection during a step down of load to 200 amp with an associated change in fuel utilization to 0.75. Additional constraints of $V_{max} = 250$ and $U_{f,min} = 0.80$ have also been included in the proposed LMI scheme. This addition of process constraint can capture unsafe process operation as shown in

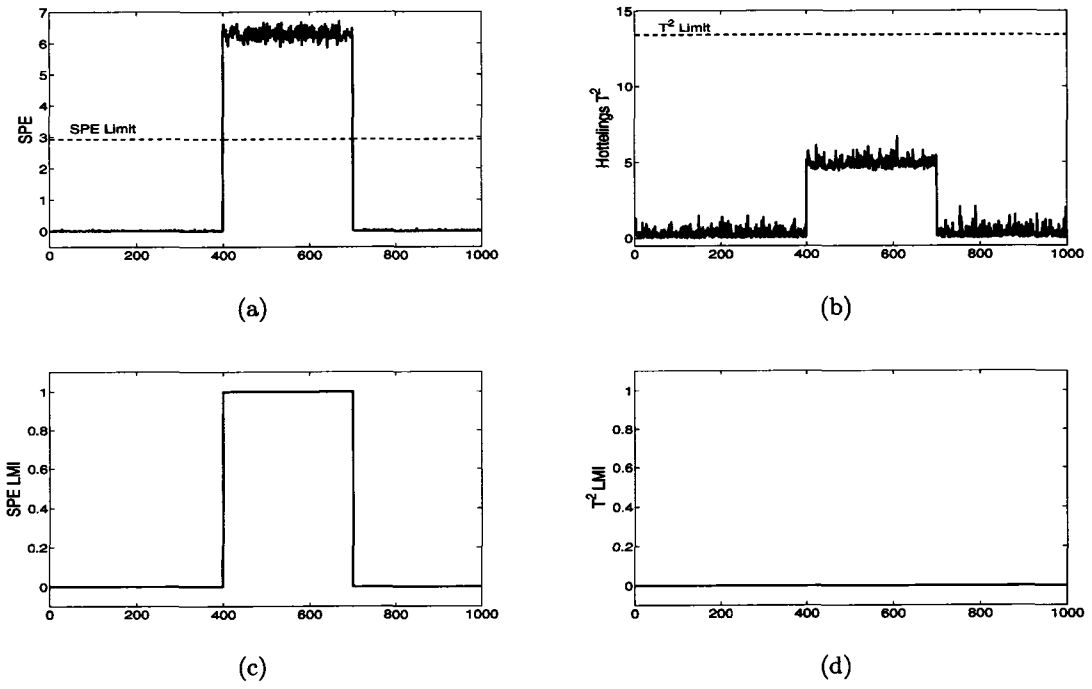

Figure 7.8: Process fault in stand-alone fuel cell is captured by both traditional and proposed scheme

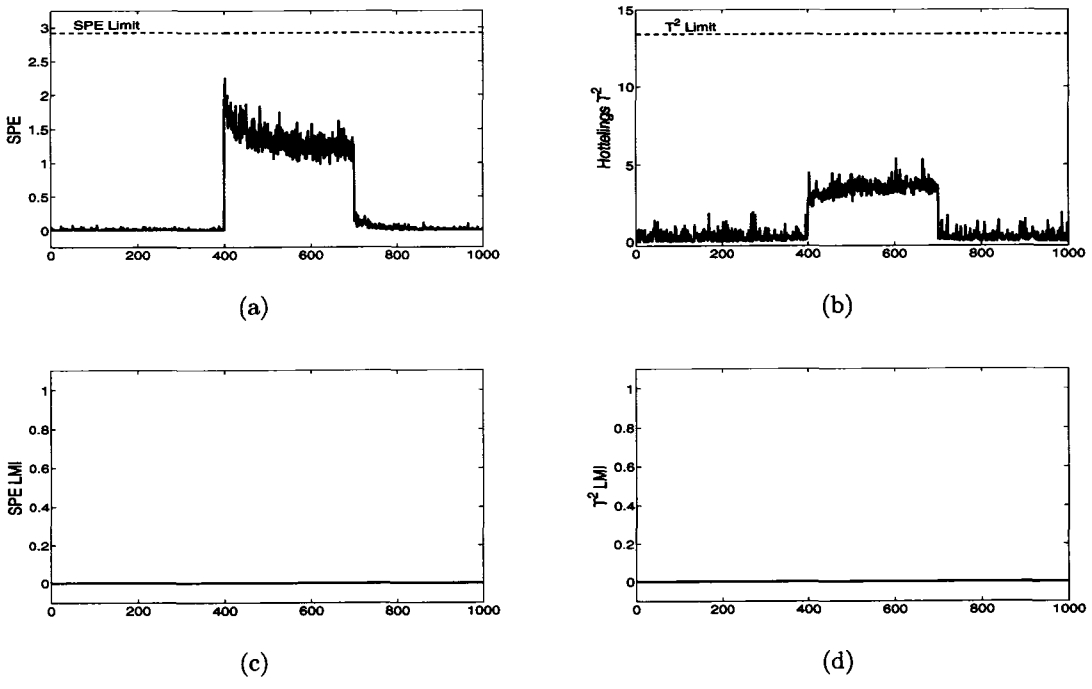

Figure 7.9: Change in stand-alone fuel cell operating region is not captured by none of the traditional PCA

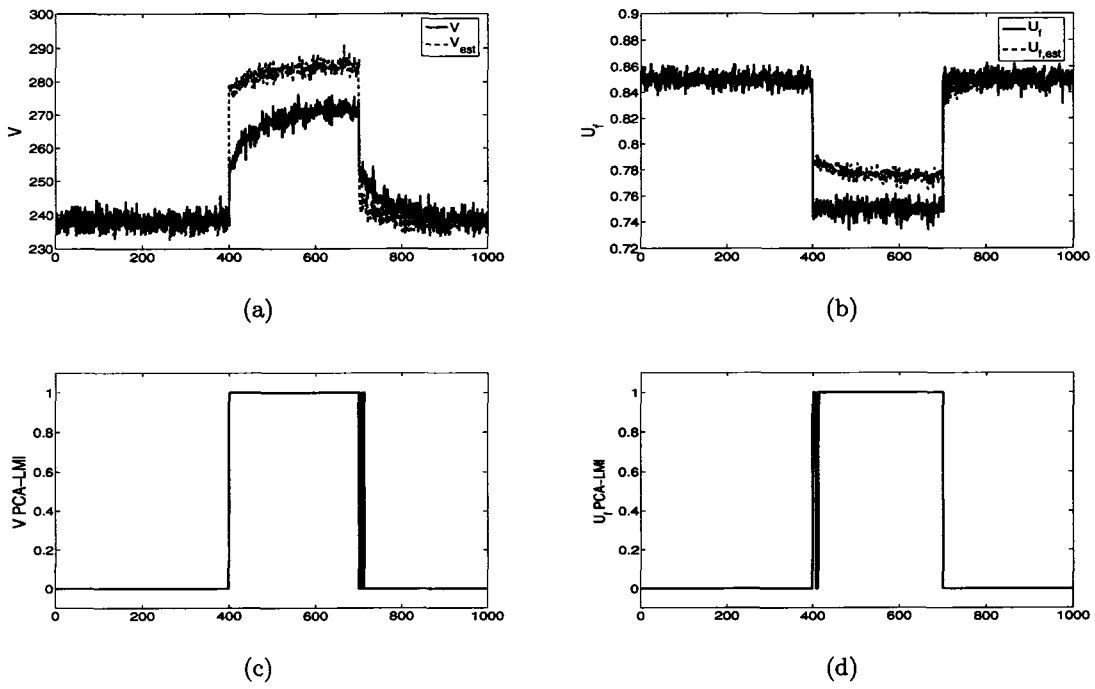

Figure 7.10: Inclusion of constraints in the proposed HPCA captures the fault in stand-alone fuel cell;

fig. 7.10 when traditional PCA does not detect any fault (fig. 7.9).

7.8.2 SOFC System without Moving Horizon Update

The proposed hybrid PCA and the traditional one is applied on the fuel cell system for fault detection. The key variables in the PCA model data matrix are voltage, fuel utilization, load, and key flow measurements. The fuel utilization, not being directly measurable, has been calculated from the estimated states using unscented Kalman filter.

In the first simulation [fig. 7.11], the system is operated in such a way that the relationship among different key variables almost hold true, but the operation is outside the boundary of the initial model between 400 to 700 second time frame. In this case, Hottellings' T^2 from traditional PCA exceeds its limit [fig. 7.11(b)]. The proposed scheme also detects the fault [fig. 7.11(d)]. Since the operating data follows the initial model structure for the entire period of operation, SPE is not violated for both schemes [fig. 7.11(a), fig. 7.11(c)].

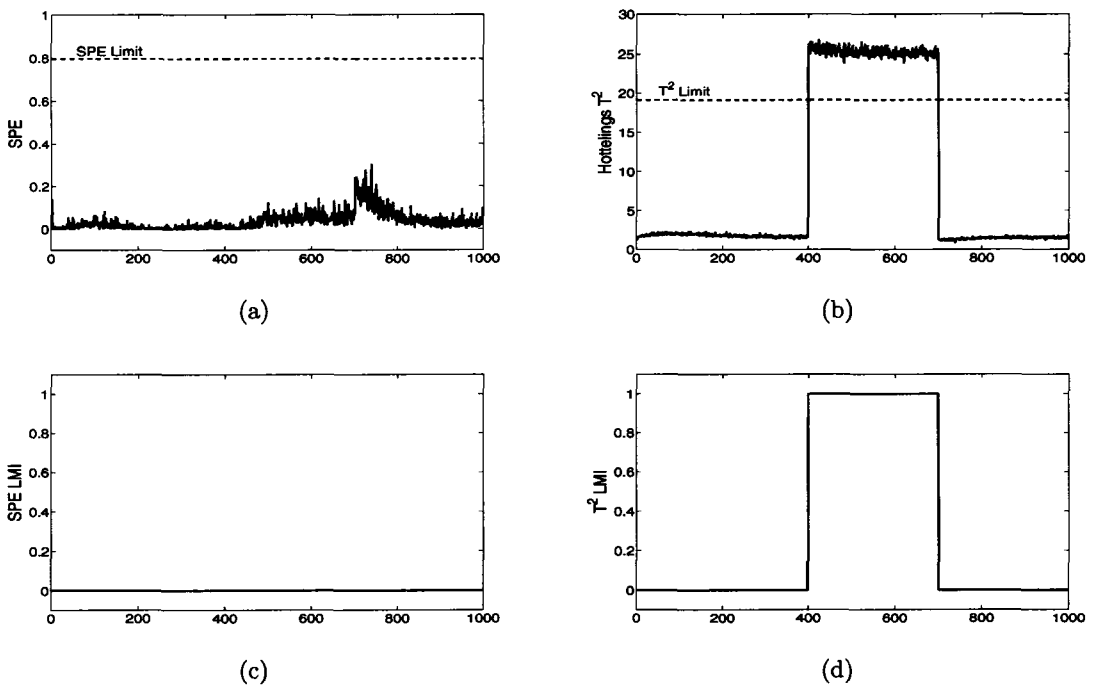

Figure 7.11: Operating fault detection for SOFC system without any moving horizon update

Next only flow rate of methane has been changed to 50% of its model data value. This results in the breaking of model structure between time sample 400 to 700 second. This is supported by the estimated voltage and fuel utilization which deviates from their true values [fig. 7.12(e), fig. 7.12(f)]. The fault is picked up by both the traditional PCA and the HPCA. In this case, the fuel cell system is operated in a region where fuel utilization is not optimal. Thus, the violation in fuel utilization is picked up by HPCA [fig. 7.12(h)]

7.8.3 SOFC System with Moving Horizon Update

The proposed scheme is then tested on the same fuel cell system, but by applying moving horizon update of the models. The inputs to the fuel cell system are the optimal inputs from table 6.1. This results in optimal operation of the fuel cell system even when no controller acts on the system. A demand current load change of 500 to 600 amp is applied on the open loop system at time step 500 second. Moving horizon model update based on Hottelling's T^2 has been applied in this case [fig. 7.13]. The transition is detected by spikes in T^2 [fig. 7.13(b)], and in T^2-LMI [fig. 7.13(d)]. Unlike

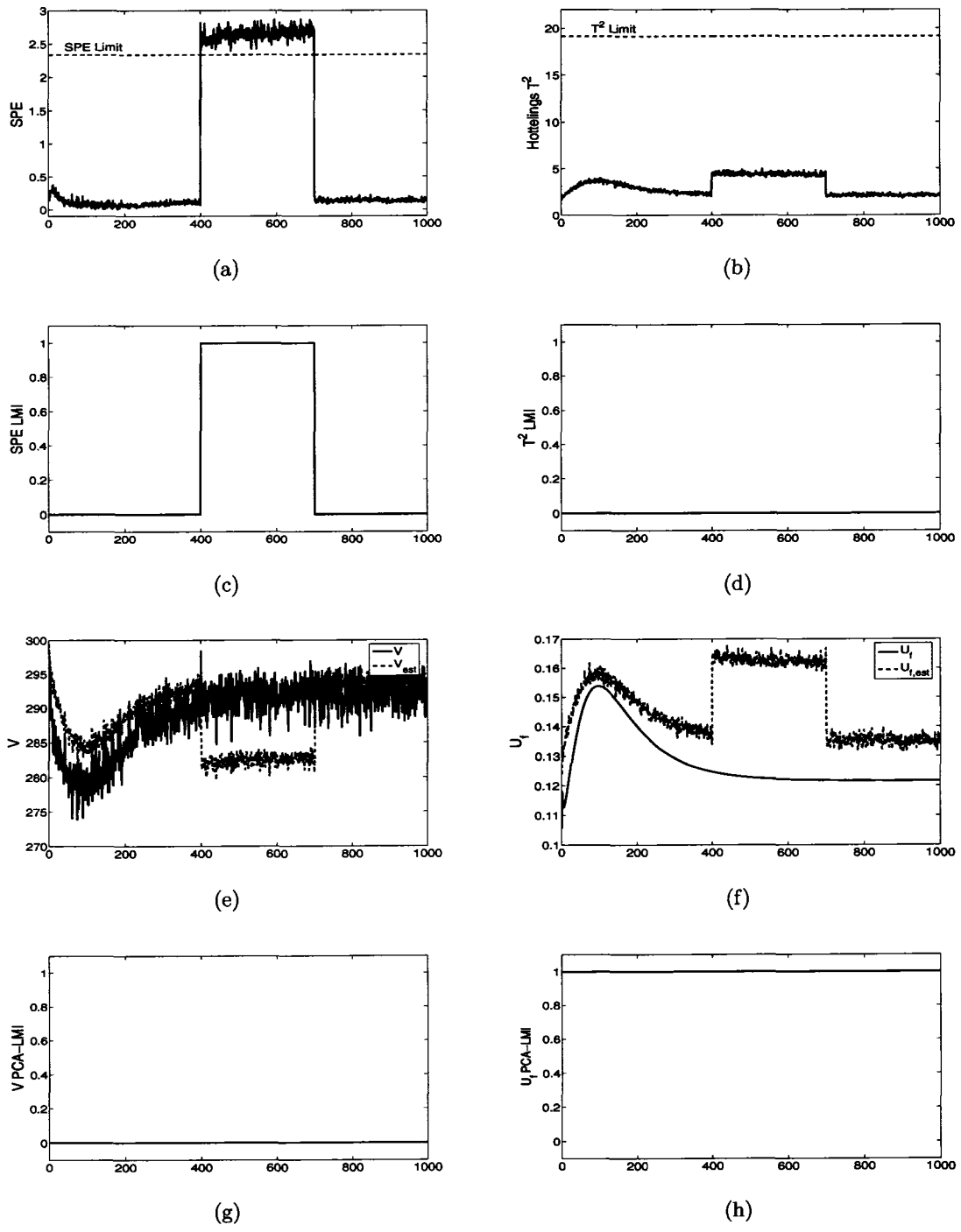

Figure 7.12: Fault detection of SOFC system without any model update

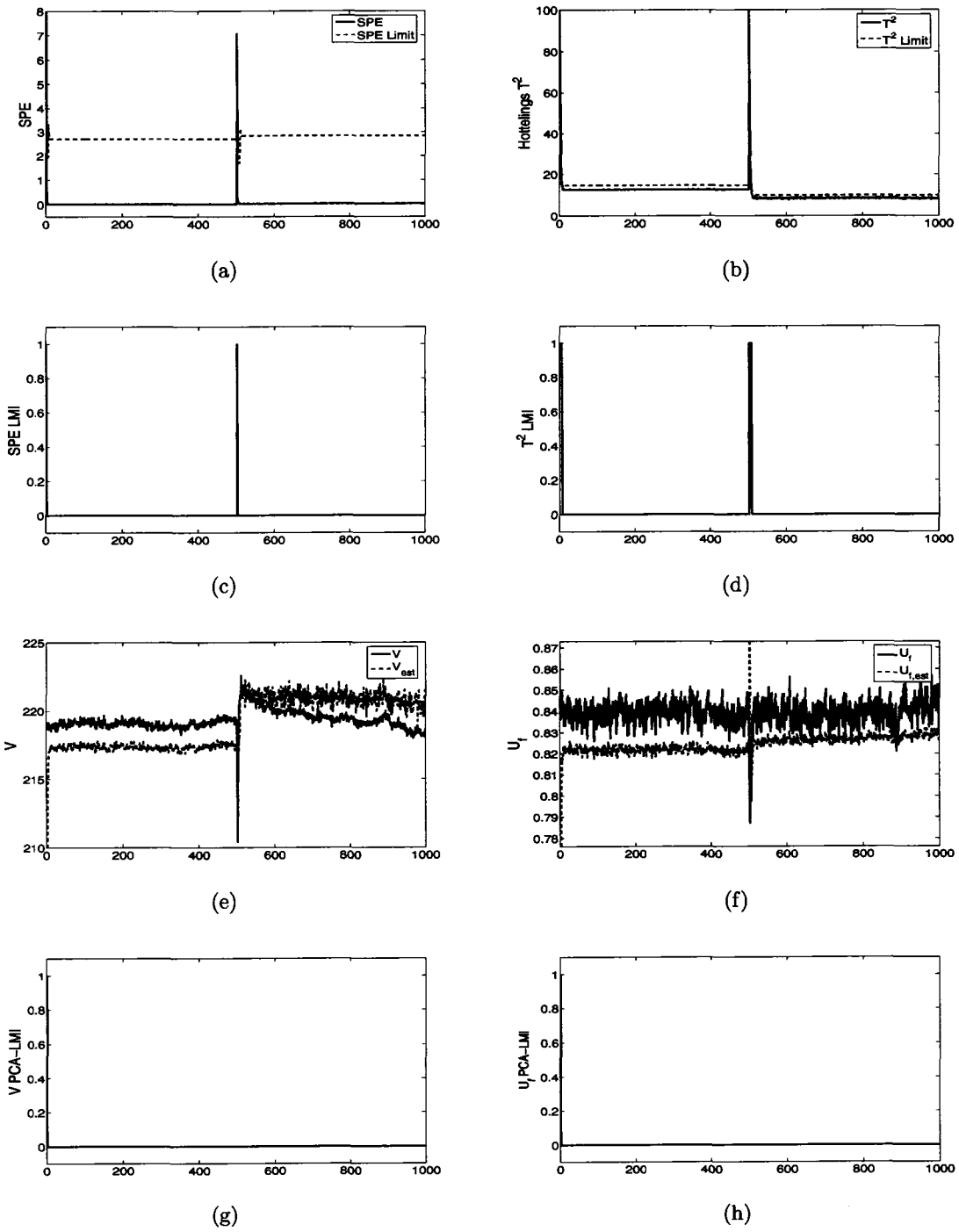

Figure 7.13: Fault detection of uncontrolled SOFC system; Model is updated based on T^2 criterion

previous case [fig. 7.12], the model is quickly updated and the estimated voltage and fuel utilization match their true responses.

A step increase in demand current has been applied on the fuel cell system at time 100. Unlike previous case, the system is controlled by nonlinear model predictive control with optimal inputs from table 6.1 as reference input in the optimization scheme. The PCA model has also been updated continuously by employing moving horizon technique. Similar to previous cases, the transition from 500 amp to 600 amp, is detected by both traditional PCA and the HPCA. In HPCA, additional constraints on fuel utilization (0.75 to 0.95) and voltage (200 to 250) have also been applied. From fig. 7.14(f) and fig. 7.14(h), it is evident that even though the nonlinear model predictive controller can quickly stabilize the system to its target voltage and fuel utilization, during transition it violates the optimal constraint. In this particular scenario *i.e.*, lower fuel utilization during transition, may not cause critical problem in the operation. But violation of fuel utilization upper limit can be detrimental to the integrity of the fuel cell stack. Unlike traditional PCA, this type of important constraints violation can be captured by HPCA.

To check the performance of HPCA, a fault in the flow rate of methane has been introduced at time 120 for the same operation described in the previous result. The fault introduces a 10% increase in the flow rate of methane. The nonlinear model predictive control still controls the system to its desired setpoint [fig. 7.15, fig. 7.16]. Since the system is back on control, it is very easy to overlook the fault which later on may actually lead to unsafe or uneconomic operation of the process. Thus, the proposed method has been applied on the system to monitor faulty situation. In this case, the HPCA model is updated based on moving horizon update according to T^2 criterion. Continuous update has not been applied since, as stated earlier, it adapts to the fault and gives a poor performance.

A look of the simulation of both the PCA and HPCA reveals that an unusual event has started to take place from time 120 [fig. 7.16]. The spike in T^2 LMI plot at time 100 [fig. 7.16(d)] confirms the transition from one operating point to another. At this time step, HPCA updates its model bringing both alarms of SPE and T^2

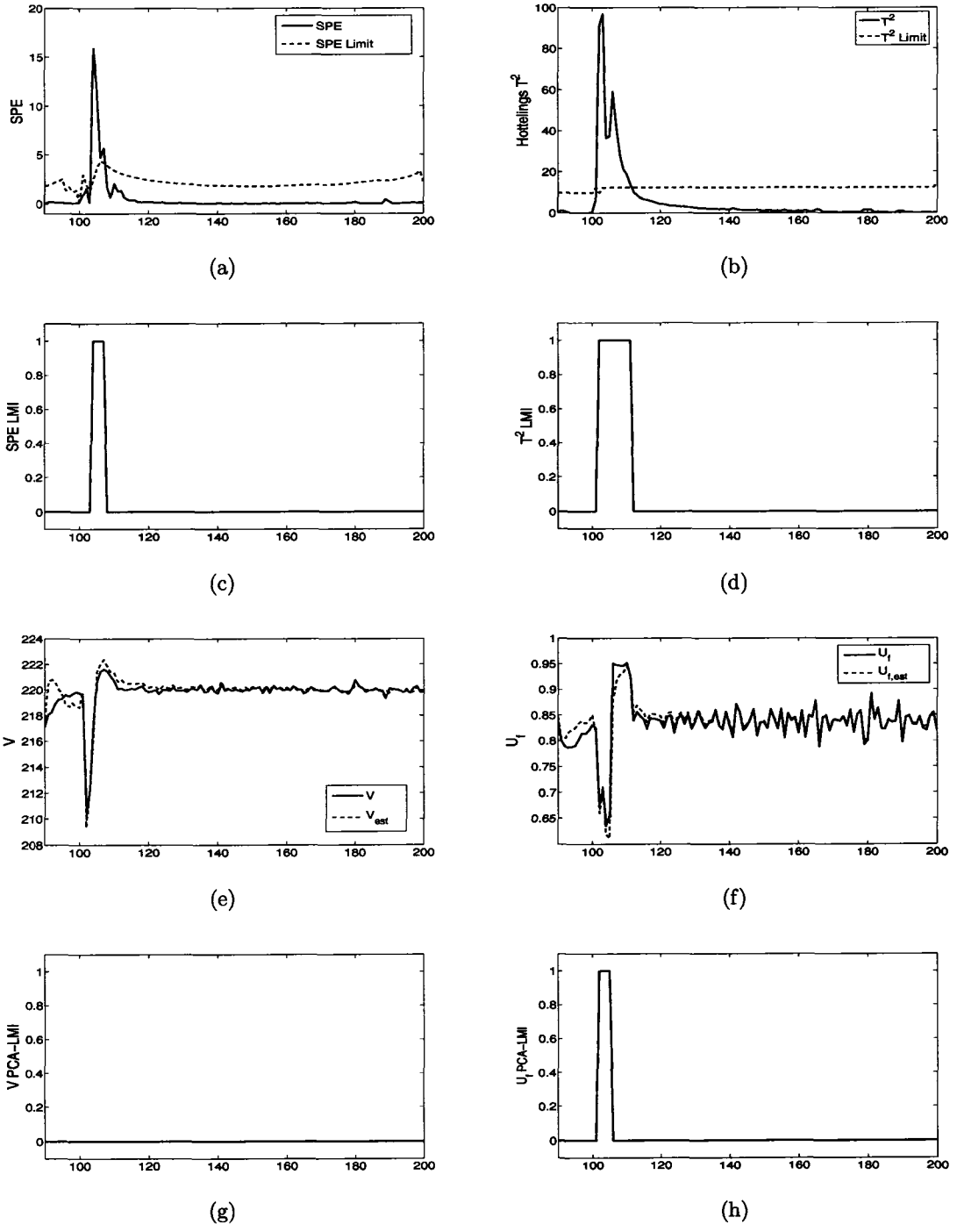

Figure 7.14: Fault detection of SOFC system with continuous update of the model; The system is controlled by applying nonlinear MPC with optimal inputs as reference inputs.

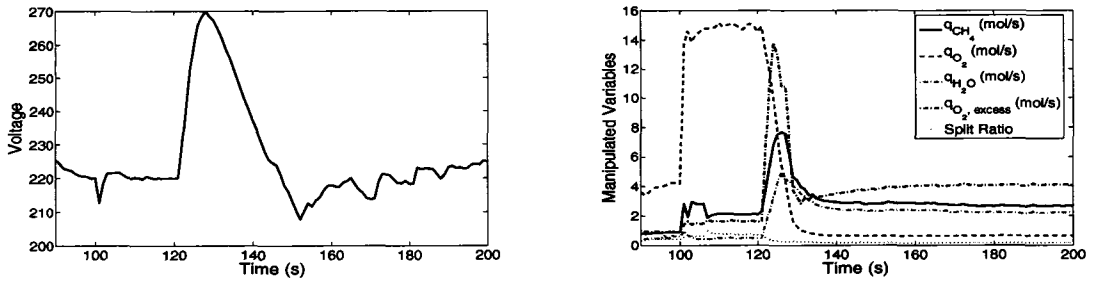

(a) (b)

Figure 7.15: Faulty system is controlled by nonlinear MPC with optimal inputs as reference inputs.

to zero. But after time 120, SPE alarm stays on even though T^2 alarm goes away with the update of the model. This gives hint about an unusual event taking place from this time instance that leads to the break of the model structure. The deviation of estimated voltage from the actual one also confirms the faulty situation. Fuel utilization, which is an important economic pointer for the operation of the fuel cell, has also been monitored for optimal operation of the system. Since fuel utilization can be expressed as a ratio of current load and hydrogen input to the fuel cell, the fault in fuel utilization [fig. 7.16(h)] can be traced back to either a fault in the load, or in the hydrogen system. Flow rate of hydrogen in the fuel cell, in turn, depends on the net flow rate of methane in the system. Thus, an expert eye can trace the origin of the fault to a few key variables and take appropriate actions.

In summary, both the traditional PCA and the proposed hybrid PCA can detect faults ranging from unsafe operation to instrument fault. In addition, hybrid PCA can detect violation of important process variables constraints which the traditional PCA can not. This can help safe operation of process. A summary of the results are given in table 7.1.

7.9 Discussions

Event though the proposed hybrid framework introduces constraints in the fault detection scheme of PCA, it also brings in some disadvantages. These are discussed below:

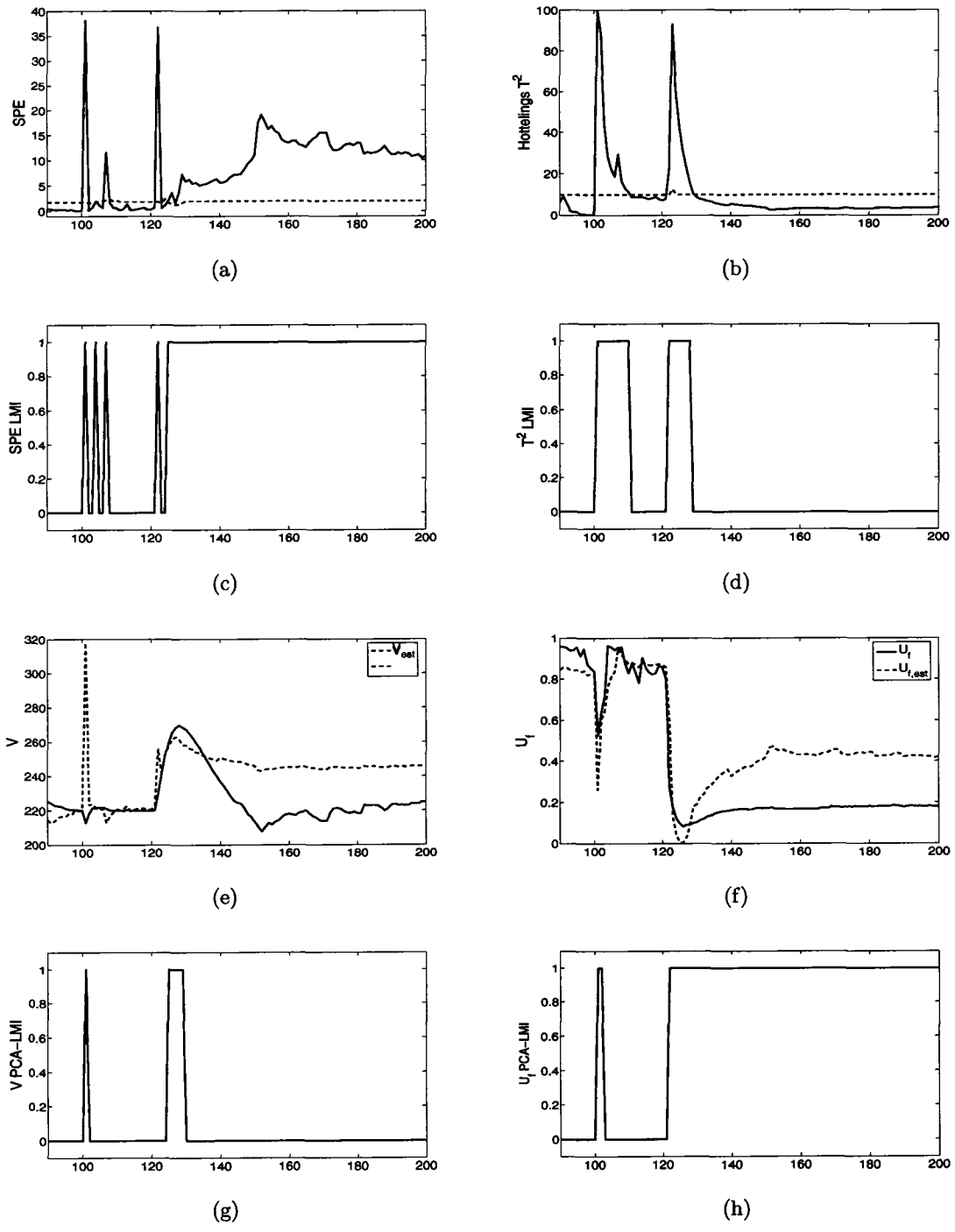

Figure 7.16: Fault detection of SOFC system with T^2 update of the model.

Table 7.1: Summary of fault detection result

Process Condition	Updated the model?	Fault	PCA	HPCA
Uncontrolled stand-alone fuel cell [fig. 7.9, fig. 7.10]	No	Process Fault	Fault undetected	Constraint violation detected
Uncontrolled System [fig. 7.11]	No	Unsafe Operation	Fault detected	Fault detected
Uncontrolled system [fig. 7.12]	No	Instrument	Fault detected; Constraint violation not detected	Fault detected; Constraint violation detected
Uncontrolled System [fig. 7.13]	Yes	Unsafe Operation	Transition detected	Transition detected
Controlled System [fig. 7.14]	Yes	Unsafe Operation	Transition detected	Transition Detected; Constraint violation detected
Controlled System [fig. 7.15, fig. 7.16	Yes	Instrument	Fault detected	Fault detected; Constraint violation detected

- **Optimization:** In the proposed method, traditional fault detection techniques such as PCA is presented as a linear matrix inequality. It introduces additional requirement of computational power for solving the LMI problem. In some cases, if the constraints are too tight, it might not be able to solve the optimization problem due to the unavailability of a suitable solver, or infeasible initial solution.

- **Orthogonality Test:** When Hottllings' T^2 and process constraints are converted to the proposed LMI framework, they cannot be solved individually. Thus orthogonality test [eqn. (7.34), eqn. (7.49)] has to be performed on the LMI variables which introduces an additional parameter ϵ. Ideally ϵ should be zero [eqn. (7.33)], but in practical scenario, ϵ should be a very small number. In this work, it has been found that taking ϵ equal to the 99% threshold of SPE (eqn. (7.46)) suffices the need in most cases. Taking ϵ greater than the SPE threshold may result in the failure of detection of constraint violation.

- **Plotting Trends:** In traditional PCA, trends of SPE and Hottellings' T^2 can be generated. These trends can provide a good premonition of faulty situations to expert eyes. Understanding the trends however requires training and knowledge of PCA to some extent. HPCA on the other hand, generates alarm only, which does not need any expert to explain the situation.

- **Contribution to Fault:** In traditional PCA, the contribution to the process fault by each variable can be calculated and ranked. Based on this contribution, the source to the fault can be traced to some extent. The proposed linear matrix inequality framework, however does not calculate the SPE and thus does not rank the key variables accordingly. Monitoring of key variables for constraint violation however outweighs this disadvantage.

- **Noise Free Estimation:** Since HPCA checks constraint violation based on noise-free estimation, it reduces frequent alarms for process variables operating near their constraints.

7.10 Conclusion

In this work, a hybrid principal component analysis method is proposed. Method of introducing additional constraints derived from process knowledge in the existing traditional PCA framework has been shown. The proposed method is tested through extensive validation of simulated and industrial data. The framework can identify constraint violations which traditional FDI techniques like PCA can not.

Chapter 8

Findings and Recommendations

In this work, control relevant modeling of planar solid oxide fuel cell is done followed by designing nonlinear model predictive control. Performance of different linear and nonlinear controllers are compared by taking convective loop reactor as an example. As a part of this work, a process monitoring application based on conventional PCA is also developed which followed development of hybrid PCA and can incorporate physical constraints into the model. During the course of the work, several things arose which can be used to fine tune models as well as controllers and fault detection application. These are discussed below.

8.1 Modeling

8.1.1 Flow Dynamics

The developed models of SOFC and balance of plant are lumped in nature. These models are fairly easy to use for designing controller as opposed to the distributed models which are more suitable for performance analysis and optimal design of the fuel cell system. However the developed models can be further improved by incorporating lumped flow models for the balance of plant as well as piping system.

8.1.2 Optimal System Parameters

System parameters are estimated depending on the design capacity of the system under consideration. These parameters have been calculated by trial-and-error and thus may not be optimal for running the system for other operating conditions. It is however possible to estimate these parameters such that the system can operate with minimal energy in the exhaust. This can be easily done by augmenting the parameters into the input vector and solving the optimization algorithm described in section 6.4. For example, finding reformer area to meet the target H_2 for fuel cell proved difficult. Later on when operating conditions were increased, the number of unreacted methane from the reformer for the same reformer area became higher which in turn increased the exhaust temperature. On the other hand, the reformer area can be calculated using the optimization algorithm for better performance of the entire fuel cell system.

8.1.3 Efficient System Architecture

During the design of the controller for the fuel cell system, it is found that the system architecture affects the ability of the controller to regulate the system. For example, during previous trial of designing controller for the fuel cell system described in fig. 3.3, there was no extra oxygen stream in the burner. Rather the required oxygen for the fuel cell reactions and the combustion in the burner was fed into the upstream of air heat exchanger which increased the pressure on the cathode side of the fuel cell. Thus it was difficult to maintain the fuel cell pressure differential between cathode and anode. Moreover all of the exhaust gas passed through fuel and air heat exchangers which made it difficult to control the fuel cell temperature. Thus an extra stream of air is fed into the burner directly and one small stream is split from the exhaust to pass through the exchangers for better control of differential pressure and temperature in the fuel cell.

The performance could further be enhanced by including bypass stream around each heat exchangers and including another extra heat exchanger after the reformer for

balancing the decrease of temperature due to reformer endothermic reaction. The system can further be extended by adding dynamic models of turbine and compressor and see the effect of running the system optimally for producing maximum direct energy. A DC-AC converter can also be incorporated into the system for AC voltage production instead of DC voltage.

8.2 Designing Controllers

8.2.1 Discretization of the models

Nonlinear MPC works fairly well for both SOFC system and convective loop reactor. However, since the developed models are continuous in nature, they need to be discretized, which is done by employing the orthogonal collocation method. In this method, the continuous time nonlinear dynamic model is expressed by a set of nonlinear algebraic equations. With the increase of the number of nodal points between each sampling interval, the number of states is also increased. This in turn increases the computational load for nonlinear MPC. The computational load due to orthogonal collocation method can be compared with other discretization methods such as Galerkin method.

8.2.2 State Estimation

In our work, unmeasured states are estimated using unscented Kalman filter (UKF) which, unlike extended Kalman filter (EKF), does not require jacobean of the model and gives better accuracy over EKF. Thus EKF is not recommended for state estimation of systems with complex dynamic models. Rather the performance of UKF can be compared with particle filter in terms of implementation and accuracy of state estimation.

8.3 Fault Detection

Hybrid PCA is developed by extending traditional PCA so that it can handle constraints. This scheme works for linear systems operating at steady state. It is not suitable for transition period or for system showing nonlinear behavior. In the case of nonlinearity, moving horizon PCA (which has in fact been employed in the process monitoring application) can be used. On the other hand, the feasibility of extending hybrid PCA for nonlinear system may be worth studying.

Bibliography

[1] E. H. Abed and J. H. Fu. Local feedback stabilization and bifurcation control; I. Hopf bifurcation. *Systems and Control Letters*, 7(1):11–17, 1986.

[2] E. H. Abed and J. H. Fu. Local feedback stabilization and bifurcation control; II. Stationary bifurcation. *Systems and Control Letters*, 8(5):467–473, 1987.

[3] B.E. Abulnaga. *Slurry Systems Handbook.* McGraw Hill, 2002.

[4] Elmar Achenbach. Response of a solid oxide fuel cell to load change. *Journal of Power Sources*, 57:105–109, 1995.

[5] F. Allgower and R. Findeisen. An introduction to nonlinear model predictive control. In *21st Benelux meeting on Systems and Control*, Veldhoven, 2002.

[6] F. Allgower, T.A. Badgwell, J.S. Qin, J.B. Rawlings, and S.J. Wright. Nonlinear predictive control and moving horizoon estimation - an introductory overview. In P.M. Frank, editor, *Advances in Control, Highlights of ECC' 99*, pages 391–449. Springer, 1999.

[7] F. Allgower, R. Findeisen, and Z.K. Nagy. Nonlinear model predictive control: from theory to application. *J. Chin. Inst. Chem. Engrs.*, 35(3):299–315, 2004.

[8] B Anderson and J. Moore. *Optimal Filtering.* Englewood Cliffs, Prentice Hall, New Jersy, 1979.

[9] B.R. Bakshi. Multiscale PCA with application to multivariate statistical process monitoring. *AIChE J.*, 44(7):1596–1610, 1998.

[10] M. Basseville. Detecting changes in signals and systems–a survey. *Automatica*, 24(3):309–326, 1988.

[11] H. H. Bau and J. Singer. Controlling a chaotic system. *Physical Review Letter*, 66:1123–1125, 1991.

[12] N.F. Besset, W.J. Wepfer, and J. Winnick. A mathematical model of a solid oxide fuel cell. *Journal of Electrochem Soc*, 142(11):3792–3800, 1995.

[13] S. Bian and M.A. Henson. Nonlinear state estimation and model predictive control of nitrogen purificaiton columns. *Ind. Eng. Chem. Res.*, 44:153–167, 2005.

[14] Atilla Bıyıkoğlu. Reviewof proton exchange membrane fuel cell models. *International Journal of Hydrogen Energy*, 30:1181–1212, 2005.

[15] Roberto Bove, Piero Lunghi, and Nigel M. Sammes. SOFC mathematic model for systems simulations - Part 1: from a micro-detailed to macro-black-box model. *International Journal of Hydrogen Energy*, 30:181–187, 2005.

[16] Roberto Bove, Piero Lunghi, and Nigel M. Sammes. SOFC mathematic model for systems simulations - Part 2: definition of an analytical model. *International Journal of Hydrogen Energy*, 30:189–200, 2005.

[17] Dejan M. Bošković and Miroslav Krstić. Nonlinear stabilization of a thermal convective loop by state feedback. *Automatica*, 37(12):2033–2040, 2001.

[18] S. Boyd, L.E. Ghaoui, E. Feron, and V. Balakrishnan. *Linear Matrix Inequalities in System and Control Theory.* SIAM Studies in Applied Mathematics, 1994.

[19] Robert J. Braun. *Optimal design and operation of solid oxide fuel cell systems for small-scale stationary applications.* Phd thesis, University of Wisconsin-Madison, 2002.

[20] J. A. Burns. Optimal sensor location for robust control of distributed parameter systems. In *Proceedings of 33rd IEEE conference on Decision and Control*, pages 3967–3972, Lake Buena Vista, Florida, USA, December 1992.

[21] E.F. Camacho and C. Bordons. *Model Predictive Control in the Process Industry - Advances in Industrial Control.* Springer-Verlag, London, 1995.

[22] S. Campanari and P. Iora. Comparison of finite volume SOFC models for the simulation of a planar cell geometry. *Fuel Cells*, 5(1):34–51, 2005.

[23] M. Cannon, B. Kouvaritakis, M. Grimble, and B. Bulut. Nonlinear predictive control of hot strip rolling mill. *Int. J. Robust Nonlinear Control*, 13:365–380, 2003.

[24] S.H. Chan and O.L. Ding. Simulation of a solid oxide fuel cell power system fed by methane. *International Journal of Hydrogen Energy*, 30(1):167–179, 2005.

[25] S.H. Chan, H.K. Ho, and O.L. Ding. Analysis of a simple solid oxide fuel cell system with gas dynamic in afterburner and connecting pipes. *Fuel Cells*, 5(1): 25–33, 2005.

[26] Denver Cheddie and Norman Munroe. Review and comparison of approaches to proton exchange membrane fuel cell modeling. *Journal of Power Sources*, 147:72–84, 2005.

[27] Wen-Hua Chen and Donald J. Ballance. Model predictive control of nonlinear systems: Computational burden and stability. CSC report: CSC-99007, Center for Systems and Control and Department of Mechanical Engineering, University of Glasgow, UK, September 1999.

[28] D.W. Clarke. *Advances in Model Based Predictive Control.* Oxford University Press, New York, 1994.

[29] D.W. Clarke and R. Scattolini. Constrained receding horizon predictive control. *Proc. IEEE*, 138(4):347, 1991.

[30] F.A. Cuzzola, J.C. Geromel, and M. Morari. An improved approach for constrained robust model predictive control. *Automatica*, 38:1183–1189, 2002.

[31] David L. Damm and Andrei G. Fedorov. Radiation heat transfer in SOFC materials and components. *Journal of Power Sources*, 143:158–165, 2005.

[32] Fred Daum. Nonlinear filters: beyond the Kalman filter. IEEE A&E *Systems Magazine*, 20(8):57–69, 2005.

[33] Nicholas W. Deluca and Yossef A. Elabd. Polymer electrolyte membranes for the direct methanol fuel cell: A review. *Journal of Polymer Science: Part B: Polymer Physics*, 44:22012225, 2006.

[34] M. Diehl, I. Uslu, R. Findeisen, S. Schwarzkopf, F. Allgower, H.G. Bock, T. Bürner, E. Gilles, A. Kienle, J. Schlöder, and E. Stein. Real-time optimization of large scale process models: Nonlinear model predictive control of a high purity distillation column. In M. Groetschel, S. Krumke, and J. Rambau, editors, *Online optimization of large scale systems: State of the art.* Springer, 2001.

[35] D. Dong and T.J. McAvoy. Batch tracking via nonlinear principal component analysis, 1996.

[36] M. S. Donne, A. W. Pike, and R. Savry. Application of modern methods in power plant simulation and control. *IEE Computing and Control Journal*, 12 (2):7584, 2001.

[37] R. Dunia and S.J. Qin. Subspace approach to multidimensional fault identification and reconstruction. *AIChE Journal*, 44(8):1813–1831, 1998.

[38] R. Dunia, S.J. Qin, T.F. Edgar, and T.J. McAvoy. Identification of faulty sensors using principal component analysis, 1996.

[39] Peter Ehrhard and Ulrich Müller. Dynamical behaviour of natural convection in a single-phase loop. *J. Fluid Mech.*, 217:487–518, 1990.

[40] M.Y. El-Sarkh, A. Rahman, and M.S. Alam. Neural networks-based control of active and reactive power of a stand-alone PEM fuel cell power plant. *Journal of Power Sources*, 135:88–94, 2004.

[41] Richard M. Felder and Ronald W. Rousseau. *Elementary Principles of Chemical Processes.* John Wiley & Sons, Inc, 2nd edition, 1986.

[42] R. Findeisen, L. Imsland, F. Allgower, and G.A. Foss. Output feedback stabilization for constrained systems with nonlinear model predictive control. *Int. J. Rob. Non. Control*, 2003.

[43] Bruce A. Finlayson. *Nonlinear Analysis in Chemical Engineering.* McGraw-Hill Chemical Engineering Series. McGraw-Hill International Book Co., 1980.

[44] P.M. Frank. Fault diagnosis in dynamic-systems using analytical and knowledge-based redundancy–a survey and some new results. *Automatica*, 26 (3):459–474, 1990.

[45] C.E. Garcia, D.M. Pratt, and M. Morari. Model predictive control: Theory and practice - a survey. *Automatica*, 25(3):335, 1989.

[46] J. Gertler. Survey of model-based failure detection and isolation in complex plants. *IEEE Control Systems Magazine*, pages 3–11, 1988.

[47] Joshua Golbert and Daniel R. Lewin. Model-based control of fuel cells: (1) regulatory control. *Journal of Power Sources*, 135:135–151, 2004.

[48] N. Gordon, D. Salmond, and A. Smith. Novel approach to nonlinear/non-gaussian bayesian state estimation. *IEEE Trans. Radar, Signal Processing*, 140:711–732, 1993.

[49] R. Greif. Natural circulation loops. *Trans. ASME C: J. Heat Transfer*, 110: 1243–1258, 1988.

[50] A. Hagen, M. Menon, R. Barfod, P.V. Hendriksen, S. Ramousse, and P.H. Larsen. Properties and performance of SOFCs produced on a pre-pilot plant scale. *Fuel Cells*, 6(2):146–150, 2006.

[51] David J. Hall and R. Gerald Colclaser. Transient modeling and simulation of a tubular solid oxide fuel cell. *IEEE Transactions on Energy Conversion*, 14(3): 749–753, 1999.

[52] R. Hanke, M. Mangold, and K. Sundmacher. Application of hierarchical process modeling strategies to fuel cell systems - towards a virtual fuel cell laboratory. *Fuel Cells*, 5(1):133–147, 2005.

[53] V. Havlena and J. Findejs. Application of model predictive control to advanced combustion control. *Control Engineering Practice*, 13:671–680, 2005.

[54] S. Haykin, editor. *Kalman Filtering and Neural Networks*, chapter 7: The unscented Kalman filter for nonlinear state estimation - Wan, Eric A. and Rudolph van der Merwe. Wiley, 2001.

[55] Michael A. Henson and Dale E. Seborg, editors. *Nonlinear Process Controls*, chapter 5: Model Predictive Control - E.S. Meadows and J.B. Rawlings, pages 233–310. Prentice Hall, 1997.

[56] Michael A. Henson and Dale E. Seborg, editors. *Nonlinear Process Controls*, chapter 7: Nonlinear state estimation - Kenneth R. Muske and Thomas F. Edgar, pages 311–369. Prentice Hall, 1997.

[57] Allen Hermann, Tapas Chaudhuri, and Priscila Spagnol. Bipolar plates for PEM fuel cells: A review. *International Journal of Hydrogen Energy*, 30:1297–1302, 2005.

[58] Eduardo Hernandez-Pacheco, Michael D. Mann, Phillip N. Hutton, Devinder Singh, and Kyle E. Martin. A cell-level model for a solid oxide fuel cell operated with syngas from a gasification process. *International Journal of Hydrogen Energy*, 30:1221–1233, 2005.

[59] D.M. Himmelblau. *Fault detection and diagnosis in chemical and petrochemical processes.* Elsivier Press, Amsterdam, 1978.

[60] H. Hotelling. Multivariate quality control illustrated by the testing of sample bombsights. In *O. Eisenhart (Ed.), Selected techniques of statistical analysis*, pages 113–184, NY, 1947. McGraw Hill.

[61] Y. Inui, N. Ito, T. Nakajima, and A. Urata. Analytical investigation on cell temperature control method of planer solid oxide fuel cell. *Energy Conversion and Management*, 47:2319–2328, 2006.

[62] P. Iora, P. Aguiar, C.S. Adjiman, and N.P. Brandon. Comparision of two IT DIR-SOFC models: Impact of variable thermodynamic, physical, and flow properties. Steady-state and dynamic analysis. *Chemical Engineering Science*, 60(3):2963–2975, 2005.

[63] R. Isermann. Process fault detection based on modeling and estimation methods–a survey. *Automatica*, 20:387–404, 1984.

[64] J.E. Jackson. *A User's Guide to Principal Components.* John Wiley & Sons, Inc, USA, 1991.

[65] J.E. Jackson and G.S. Mudhokar. Control procedures for residuals associated with principal component analysis. *Technometrics*, 21:341–349, 1979.

[66] H.-J. Jahn and W. Schroer. Mathematical model of a residential fuel cell power plant and its application to start-up optimization. *Fuel Cells*, 4(4):276–282, 2004.

[67] A.H. Jazwinski. *Stochastic Processes and Filtering Theory.* Academic Press, New York, 1970.

[68] R.A. Johnson and D.W. Wichern. *Applied Multivariate Statistical Analysis.* Prentice Hall, 4th edition, 1998.

[69] I.T. Joliffe. *Principal Component Analysis.* Berlin, 1986.

[70] S.J. Julier. The scaled unscented transformation. In *Proceedings of the American Control Conference*, volume 6, pages 4555–4559, 2002.

[71] S.J. Julier, J.K. Uhlmann, and H.G. Durrant-Whyte. A new approach for filtering nonlinear systems. In *Proceedings of the American Control Conference*, pages 1628–1632, 1997.

[72] H.K. Khalil. *Nonlinear Systems.* Prentice Hall, 2 edition, 1996.

[73] Taihyun Kim and Eyad H. Abed. Stationary bifurcation control of systems with uncontrollable linearization. *Int. J. Control*, 74(5):445–452, 2001.

[74] S. Koch, P.V. Hendriksen, M. Mogensen, Y.-L. Liu, N. Dekker, B. Rietveld, B. de Haart, and F. Tietz. Solid oxide fuel cell performance under severe operating conditions. *Fuel Cells*, 6(2):130–136, 2004.

[75] B. Kouvaritakis, J. A. Rossiter, and J. Schuurmans. Efficient robust predictive control. *IEEE Transactions on Automatic Control*, 45(8):15451549, 2000.

[76] J. Kresta, J.F. McGregor, and T.E. Marlin. Multivariate statistical monitoring of process performance. *Can. J. Chem. Eng.*, 69, 1991.

[77] Leon Lapidus and John H. Seinfeld. *Numerical Solution of Ordinary Differential Equations*, volume 74 of *Mathematics in Science and Engineering.* Academic Press, 1971.

[78] James Larminie and Andrew Dicks. *Fuel Cell Systems Explained.* John Wiley & Sons, Ltd, 2 edition, 2003.

[79] R.T. Leah, N.P. Brandon, and P. Aguiar. Modelling of cells, stacks and systems based around metal supported planer IT-SOFC cells with CGO electrolytes operating at 500-600 C. *Journal of Power Sources*, 45:336–352, 2005.

[80] Deok-Jin Lee. *Nonlinear Bayesian filtering with applications to estimation and navigation.* PhD thesis, Texas A& M University, 2005.

[81] H. C. Lee and E. H. Abed. Washout filters in the bifurcation control of high alpha flight dynamics. *Proc. American Control Conf.*, pages 206–211, 1991.

[82] J.H. Lee and Z.H. Yu. Tuning of model predictive controllers for robust perfomance. *Comp. Chem. Eng.*, 18(1):15, 1994.

[83] F.L. Lewis. *Optimal Estimation.* John Wiley and sons, New York, 1986.

[84] W. Li, H.H. Yue, S. Valle-Cervantes, and S.J. Qin. Recursive PCA for adaptive process monitoring. *J. of Process Control*, 10:471–486, 2000.

[85] Y.H. Li, S.S. Choi, and S. Rajakaruna. An analysis of the control and operation of a solid oxide fuel-cell power plant is an isolated system. IEEE *Transactions on Energy Conversion*, 20(2):381–387, 2005.

[86] John H. Lienhard IV and John H. Lienhard V. *A Heat Transfer Textbook.* Phlogiston Press, Cambridge, Massachusetts, 3 edition, 2005.

[87] Hansan Liu, Chaojie Song, Lei Zhang, Jiujun Zhang, Haijiang Wang, and David P. Wilkinson. A review of anode catalysis in the direct methanol fuel cell. *Journal of Power Sources*, 155:95–110, 2006.

[88] J. Liu and R. Chen. Sequential monte carlo methods for dynamic systems. *Journal of Amer. Stat. Assoc.*, 93:1031–1041, 1998.

[89] Y. Lu and Y. Arkun. A scheduling quasi-minmax mpc for lpvsystems. In *American Control Conference*, page 22722276, San Diego, CA, 1999.

[90] L. Ma, D.B. Ingham, M. Pourkashanian, and E. Carcadea. Review of the computational fluid dynamics modeling of fuel cells. *Journal of Fuel Cell Science and Technology*, 2:246–257, 2005.

[91] J.F. MacGregor and T. Kourti. Statistical process control of multivariate processes. *Control Engineering Practice*, 3(3):403–414, 1995.

[92] L. Magistri, A. Traverso, F. Cerutti, M. Bozzolo, and P. Costamagna. Modelling of pressurized hybrid systems based on integrated planer solid oxide fuel cell (IP-SOFC) technology. *Fuel Cells*, 5(1):80–96, 2005.

[93] P. Mandin, C. Bernay, S. Tran-Dac, A. Broto, D. Abes, and M. Cassir. SOFC modeling and numerical simulation of performances. *Fuel Cells*, 6(1):71–78, 2006.

[94] H.D. Marquez. *Nonlinear Control Systems: Analysis and Design.* John Wiley & Sons, Inc., 2003.

[95] David Q. Maune. Nonlinear model predictive control: An assessment. *Fifth International Conference on Chemical Process Control-V*, 93(316):217–231, 1997.

[96] Viral Mehta and Joyce Smith Cooper. Review and analysis of PEM fuel cell design and manufacturing. *Physics of Fluids*, 114:32–53, 2003.

[97] A. Metrol and R. Greif. A review of natural circulation loops. *NATO Advanced Study Inst. of Natural Convection: Fundam. and Applic.*, pages 1033–1081, 1984.

[98] M. Morari and J.H. Lee. Model predictive control: Past, present and future. *comp. and Chem. Eng.*, 23(4/5):667–682, 1999.

[99] AKM M. Murshed, B. Huang, and K. Nandakumar. Control of chaos in a convective loop system. *Nonlinear dynamics and systems theory*, 3(2):203–226, 2003.

[100] AKM M. Murshed, B. Huang, and K. Nandakumar. Control relevant modeling of planer solid oxide fuel cell system. *Journal of Power Sources*, 163:830–845, 2007.

[101] Nam-Trung Nguyen and Siew Hwa Chan. Micromachined polymer electrolyte membrane and direct methanol fuel cellsa review. *Journal of Micromechanics and microengineering*, 16:R1–R12, 2006.

[102] G. De Nicolao, L. Magni, and R. Scattolini. Stability and robustness of nonlinear receding horizon control. *Progress in Systems and Control Theory*, 26:3–22, 2000.

[103] P. Nomikos and J.F. MacGregor. Monitoring of batch processes using multi-way principal component analysis. *AIChE J.*, 40(8):1361–1375, 1992.

[104] G. A. Oluwande. Exploitation of advanced control techniques in power generation. *IEE Computing and Control Journal*, 12(2):63–67, 2001.

[105] M. Oshima, I. Hashimoto, T. Takamatsu, and H. Ohno. Robust stability of model predictive control. *Ind. Chem. Eng.*, 31(1):119, 1991.

[106] Edward Ott, Celso Grebogi, and James A. Yorke. Controlling chaos. *Physical Review Letters*, 64(11):1196–1199, March 1990.

[107] Aguiar P., C.S. Adjiman, and N.P. Brandon. Anode-supported intermediate-temperature direct internal reforming solid oxide fuel cell II. model-based dynamic performance and control. *Journal of Power Sources*, 147:136–147, 2005.

[108] J. Padulles, G.W. Ault, and J.R. McDonanld. An integrated SOFC plant dynamic model for power systems simulation. *Journal of power sources*, 86: 495–500, 2000.

[109] R.J. Patton, P.M. Frank, and R.N. Clark. *Fault Diagnosis in Dynamic Systems: Theory and Application.* Prentice Hall, NY, 1989.

[110] K. Pearson. On lines and planes of closest fit to systems of points in space. *Philosophical Magazine Series B*, 2:559–572, 1901.

[111] Robert H. Perry, Don W. Green, and James O. Maloney, editors. *Perry's Chemical Engineers' Handbook.* McGraw Hill, USA, 7 edition, 1997.

[112] S. Joe Qin and Thomas A. Badgwell. An overview of industrial model predictive control technology. *Fifth International Conference on Chemical Process Control-V*, 93(316):232–256, 1997.

[113] S.J. Qin. Recursive PLS algorithms for adaptive data modeling. *Comp. Chem. Eng.*, 22:503–514, 1998.

[114] S.J. Qin and T.A. Badgwell. A survey of industrial model predictive control technology. *Control Engineering Practice*, 11:733–764, 2003.

[115] R. Rajamoni and A. Ganguli. Sensor fault diagnosis for a class of non-linear systems using linear matrix inequalities. *Int. J. Control*, 77(10):920–930, 2004.

[116] Christopher V. Rao and James B. Rawlings. Nonlinear moving horizon state estimation. *Progress in Systems and Control Theory*, 26:45–69, 2000.

[117] J.B. Rawlings. Tutorial overview of model predictive control. *IEEE Control Systems Magazine*, 20:38–52, 2000.

[118] J.B. Rawlings and Bhavik R. Bakshi. Particle filtering and moving horizon state estimation. *Computers and Chemical Engineering*, 30:1529–1541, 2006.

[119] K. Ro and S. Rahman. Control of grid-connected fuel cell plants for enhancement of power system stability. *Renewable Energy*, 28:397–407, 2003.

[120] Yong Rui and Yunqiang Chen. Better proposal distributions: object tracking using unscented particle filter. Report, Collaboration and Multimedia Systems Group, Microsoft Research, One Microsoft Way, Redmond, WA 98052-6399, 2005.

[121] Shankar Sastry. *Nonlinear Systems: Analysis, Stability and Control.* Springer-Verlag New York, Inc., 1999.

[122] Kourosh Sedghisigarchi and Ali Feliachi. Dynamic and transient analysis of power distribution systems with fuel cells–part I: fuel-cell dynamic model. *IEEE transactions on energy conversion*, 19(2):423–428, 2004.

[123] Azra Selimovic, Miriam Kemm, Tord Torisson, and Mohsen Assadi. Steady state and transient thermal stress analysis in planer solid oxide fuel cells. *Journal of Power Sources*, 145:463–469, 2005.

[124] R. Shridhar and D.J. Cooper. A tuning strategy for siso unconstrained model predictive control. *Ind. Eng. Chem. Res.*, 36:729, 1997.

[125] R. Shridhar and D.J. Cooper. A tuning strategy for unconstrained multivariable model predictive control. *Ind. Eng. Chem. Res.*, 37:4003–4016, 1998.

[126] J. Singer, Y-Z. Wang, and Haim H. Bau. Controlling a chaotic system. *Physical Review Letters*, 66(9):1123–1125, March 1991.

[127] B. Smitha, S. Sridhar, and A.A. Khan. Solid polymer electrolyte membranes for fuel cell applications a review. *Journal of Membrane Science*, 259:10–26, 2005.

[128] A. Boudghene Stambouli and E. Traversa. Solid oxide fuel cells (SOFCs): a review of an environmentally clean and efficient source of energy. *Renewable and Sustainable Energy Reviews*, 6:433–455, 2002.

[129] A. B. Stephens. A finite difference galerkin formulation for the incompressible navier-stokes equation. *Journal of Computational Physics*, 53:152–172, 1984.

[130] Christopher Stiller, Bjorn Thorud, Olav Bolland, Rambabu Kandepu, and Lars Imsland. Control strategy for a solid oxide fuel cell and gas turbine hybrid system. *Journal of Power Sources*, 2005.

[131] H. Tawfik, Y. Hung, and D. Mahajan. Metal bipolar plates for PEM fuel cell a review. *Journal of Power Sources*, 163:755–767, 2007.

[132] J. O. Trierweiler and A. R. Secchi. Exploring the potentiality of using multiple model approach in nonlinear model predictive control. *Progress in Systems and Control Theory*, 26:191–203, 2000.

[133] Fuel Cell Handbook, Edition 6. US Department of Energy, 2002.

[134] Fuel Cell Handbook, Edition 7. US Department of Energy, 2004.

[135] H. Vedam, V. Venkatasubramanian, and M. Bhalodia. A B-spline based method for data compression, process monitoring and diagnosis. *Comp. Chem. Eng.*, 22:S827–S830, 1998.

[136] V. Venkatasubramanian and S.H. Rich. An object-oriented two-tier architecture for integrating compiled and deep-level knowledge for process diagnosis. *Comp. Chem. Eng.*, 14(9-10):903–921, 1990.

[137] V. Venkatasubramanian, R. Rengaswamy, K. Yin, and S.N. Kavuri. A review of process fault detection and diagnosis, part I: Quantitative model-based methods. *Comp. Chem. Eng.*, 27:293–311, 2003.

[138] V. Venkatasubramanian, R. Rengaswamy, K. Yin, and S.N. Kavuri. A review of process fault detection and diagnosis, part II: Qualitative models and search strategies. *Comp. Chem. Eng.*, 27:313–326, 2003.

[139] V. Venkatasubramanian, R. Rengaswamy, K. Yin, and S.N. Kavuri. A review of process fault detection and diagnosis, part III: Process history based methods. *Comp. Chem. Eng.*, 27:327–346, 2003.

[140] John Villadsen and Michael L. Michelsen. *Solution of Differential Equation Models by Polynomial Approximation.* Prentice Hall Inc., USA, 1978.

[141] Eric A. Wan and Rudoplh van der Merwe. The unscented Kalman filter for nonlinear estimation. In *IEEE Symposium*, Lake Louise, Alberta, Canada, Oct 2000.

[142] Eric A. Wan and Rudoplh van der Merwe. The unscented Kalman filter for nonlinear estimation. report, Oregon Graduate Institute of Science & Technology, 20000 NW Walker Rd, Beaverton, Oregon 97006, 2001.

[143] Hua O. Wang and Eyad H. Abed. Bifurcation control of a chaotic system. *Automatica*, 31(9):1213–1226, 1995.

[144] A.S. Willsky. A survey of design methods for failure detection systems. *Automatica*, 12:601–611, 1976.

[145] S. Wold. Exponentially weighted moving principal component analysis and projection to latent structures. *Chem. and Intel. Lab. Sys.*, 23:149–161, 1994.

[146] K.Z. Yao, K. Karan, K.B. McAuley, P. Oosthuizen, and T. Xie. A review of mathematical models hydrogen and direct methanol polymer electrolyte membrane fuel cells. *Fuel Cells*, 4(1-2):3–29, 2004.

[147] Alex Zheng. Some practical issues and possible solutions for nonlinear model predictive control. *Progress in Systems and Control Theory*, 26:129–143, 2000.

[148] Y. Zhu and K. Tomsovic. Development of models for analyzing the load-following pwerformance of microturbines and fuel cells. *Electric Power Systems Research*, 62:1–11, 2002.

[149] Y. Zvirin. A review of natural circulation loops in pressurized water ractors and other systems. *Nuclear Engineering Design*, 67:203–225, 1981.

Appendix A

Fault Detection Application

A.1 Description

A process monitoring application has been built based on traditional PCA. The purpose of the application is to detect possible clogging of pipelines carrying slurry. The development of the application consisted of three parts: 1) development and validation PCA model from historical data; 2) building of the process monitoring application interface using MATLAB, Visual Basic and OPC; 3) Installing and running the application in real time. A brief description of the process and the application interfaces are given in the followings.

In process industries, it is often necessary to transport slurry from one point to another. In normal operating conditions, the slurry, which is a mixture of solid particles and a carrier fluid, is carried through the pipeline in a homogeneous state. If, however, the flow rate reduces below a certain critical value, settling of the solid particles may occur and a bed is formed in the bottom of the pipeline. This in turn reduces the effective cross-sectional flow area leading to increasing pump pressure and low flow rate. Increasing the pump speed and slurry flow rate or, flushing carrier liquid is used to break the formation of the deposition at this stage. In extreme situation, the settling of the solid particles can block the pipe leading to shut down of the transport process. So it is very important to monitor such situations and take appropriate preventive actions before the blockage of the pipeline which led us to

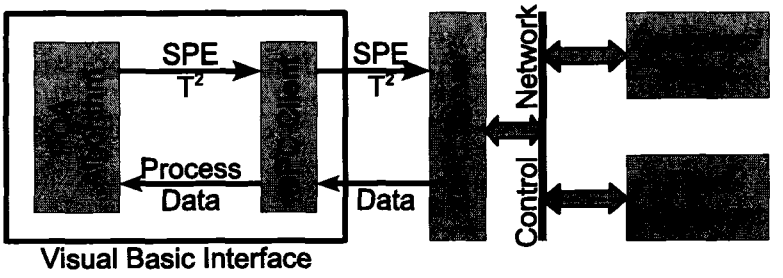

Figure A.1: Communication between the server and process monitoring application

build the process monitoring application based on the traditional PCA.

A.2 Architecture of PCA Application

The application collects current data from the server, calculates SPE, T^2, and their threshold values using traditional PCA and then plots the trends in a child window of the application interface. This application has three parts, which are described below:

- **OPC Client:** The data are collected by a client built inside the application. The client is written in *OPC* which can transmit data to and from any server supporting OPC[1] standard. The communication between the client application and server is depicted in fig. A.1.
- **PCA Algorithm:** A PCA model is then built based on the collected data. Data cleaning and PCA model building which includes calculation of SPE, Hottellings' T^2 and their limits, are performed by MATLAB. The algorithm also finds key variables based on their contribution to SPE and T^2, and generates alarm for probable unusual events. In addition, the PCA model data matrix can be updated automatically based on Hottellings' T^2 criterion or, by the intervention of the user, by employing a moving horizon scheme.
- **Interface:** The user interface is built using Visual Basic 6.0. A brief description of the process monitoring application and its functionality are given in appendix A.

[1]OPC stands for OLE for Process Control

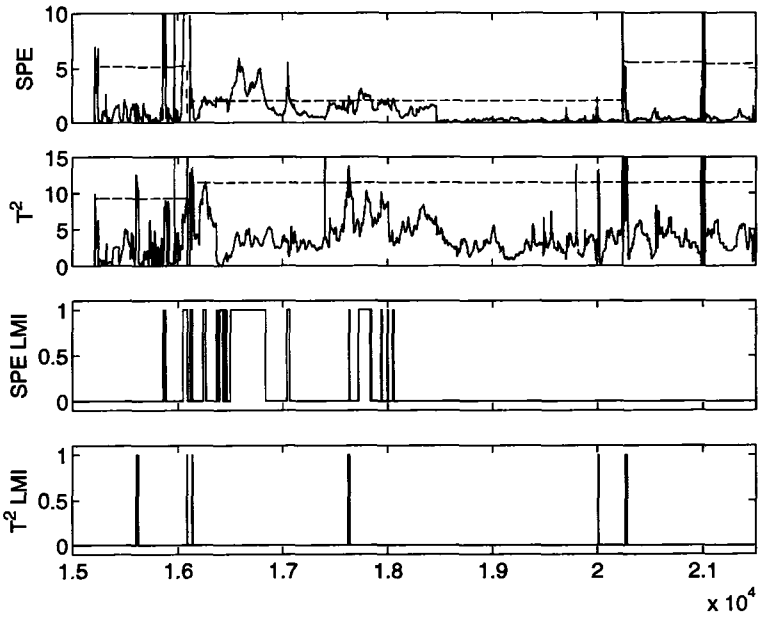

Figure A.2: SPE and T^2 from industrial data set

A.3 Result from PCA Application

The key variables used in the model are flow rate, pump discharge pressure, pump speed, density of the slurry, and percentage of other key components (Abulnaga [3]). The underlying PCA model used in the process monitoring application has been updated based on SPE and T^2 outputs along with process knowledge. Moving window type of model updating criterion has been used to keep the model up-to-date with the then current data set whenever necessary. In this criterion, the model data size has been kept fixed and whenever a new data sample has been included in the model data set, the oldest data point has been removed. The application can detect possible clogging situations in advance giving the user enough time to respond to the situation.

The proposed method has been applied on normalized industrial data set to compare it with the traditional PCA as described in the previous section. The traditional PCA could detect the clogging in advance. However process operators often designate situations such as pressure and pump speed greater than certain limits as possible faulty situations. It has been found that even though the pressure and pump speed are

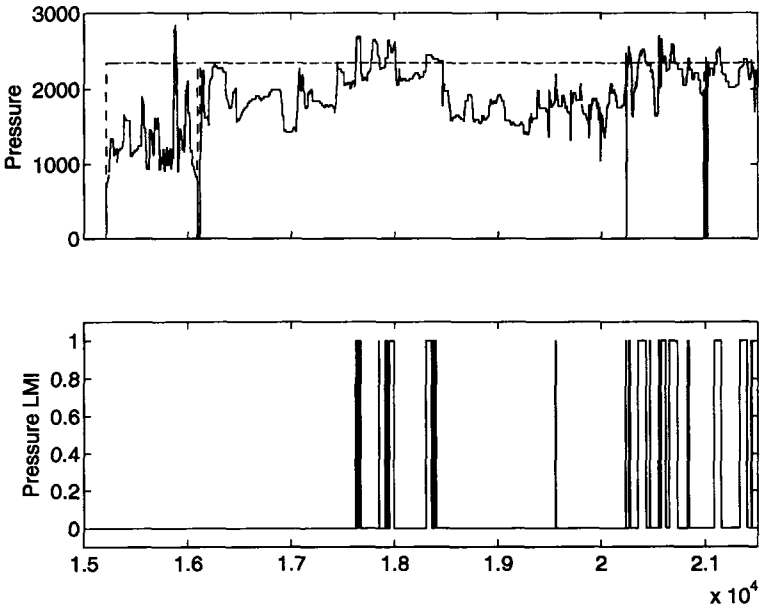

Figure A.3: Violation of the pressure constraint

larger than their critical values, the traditional PCA could not detect the violations in the observed variables' critical limits. On the other hand, the proposed framework can detect violation of limits in the key variables. The results are shown in fig. A.2 and fig. A.3.

From fig. A.2, it is clear that both PCA and HPCA can detect unusual situations. But unlike PCA, HPCA is able to incorporate constraints on key variables and report alarms if these constraints are violated as shown in fig. A.3.

A.4 Description of the Application

When the Tailings Line Monitoring application starts, a Splash window appears containing information about the application and then disappears again followed by the appearance of a main window of the application (Figure A.4). The main window captioned *Pipeline Monitor* can have several *monitoring windows* (child window). At the beginning, a monitoring window titled *Process 1* is automatically generated and is empty, waiting for the user to configure it for a particular tailings line in the plant. The main window is composed of the system bar, the main menu, the toolbar, the

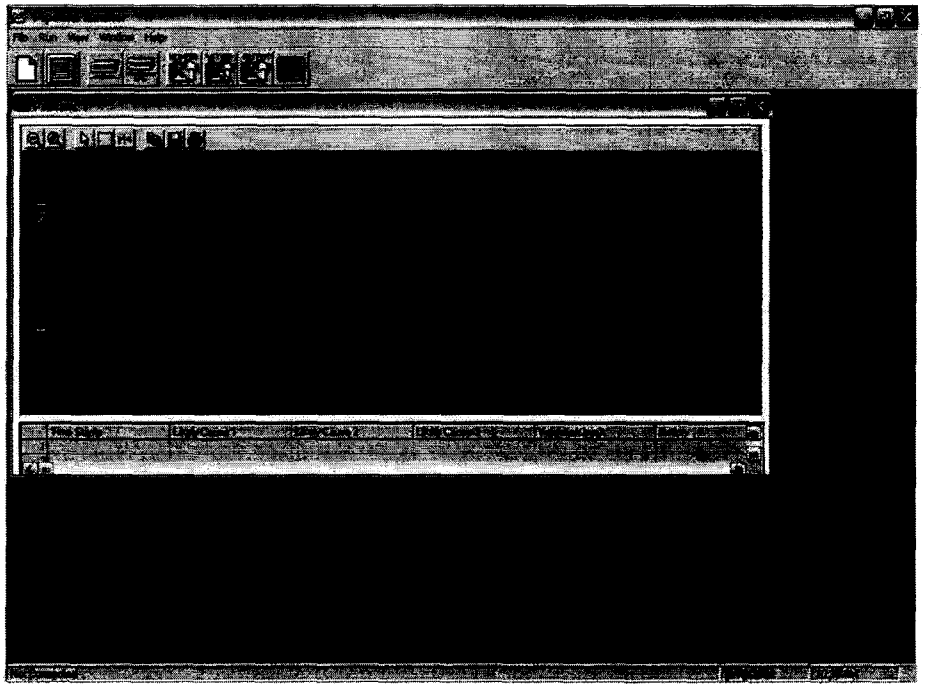

Figure A.4: Main window of the Tailings Line Monitoring Application

monitoring window and the status bar. Each monitoring window has its own toolbar for doing jobs specific to it. The components are described in the following sections.

A.4.1 Main Window Components

The main window has the following components:

A.4.1.1 Menu Bar

File menu has the following submenus

New: Opens a new monitoring window

Close: Closes the selected (highlighted) monitoring window

Exit: Disconnects from the Server and exits from the program

Run menu has the following submenus

Connect to Server: Opens the connection wizard with the options for connecting to or disconnecting from the server (section A.5.1)

Select Process: Opens a new window with the available Tailings Line name for sanding detection (section A.5.2.1)

Load TAGs and Run: Opens a new window to load TAGs and start monitoring the selected Tailings Line for sanding detection (section A.5.2.2)

Update Model: Updates the model of the highlighted *monitoring window*

Stop Updating: Stops updating the model of the highlighted *monitoring window*

Auto Update: When checked (✓) all the monitoring window updates automatically

Refresh Model: Recalculates the model for the highlighted monitoring window

View menu has the following submenus

Data Viewer: Shows a table containing the TAGs and their current values for the selected monitoring window

Window menu has the following submenus

New Window: Opens a new monitoring window (same as **File** ⇒ **New**)

Cascade: Arranges all the monitoring window in cascade

Tile Horizontal: Tiles all the monitoring windows in the horizontal direction

Tile Vertical: Tiles all the monitoring windows in the vertical direction

Arrange Icons: Arranges the window with the default mode

Help menu has the following submenus

Contents:

About: Opens an window containing information about the Sanding Detection application

A.4.1.2 Tool Bar

Tool Bar has the following redundant buttons

Figure A.5: Main Window Toolbar

New: Opens a new monitoring window

Data Viewer: Same as **View ⇒ Data Viewer)**

Connect: Same as **Run ⇒ Connect to Server**

Disconnect: Disconnects from the Server

Update: Same as **Run ⇒ Update Model**

Stop Updating: Same as **Run ⇒ Stop Update**

Auto Update: Same as **Run ⇒ Auto Update**

Refresh Model: Same as **Run ⇒ Refresh Model**

A.4.1.3 Status Bar

Status bar has three panels. The First Panel gives the status of the connection. If the application is connected to the server then it displays the Node and the Server name. The other two panels merely displays current date and time.

A.4.2 Monitoring Window

The monitoring window has the following components in its toolbar:

Zoom Out All Axes: Zooms out the trend lines in the monitoring window

Zoom In All Axes: Zooms in the trend lines

Copy to Clipboard: Copies the trend lines of the monitoring window in the clipboard which can be placed later on in any document (*e.g.*, Microsoft Word) by pressing **Ctrl+V** in the keyboard

Save to File: Saves the trend lines in *.jpg, *.png or, *.bmp formats

Print: Prints the trend lines

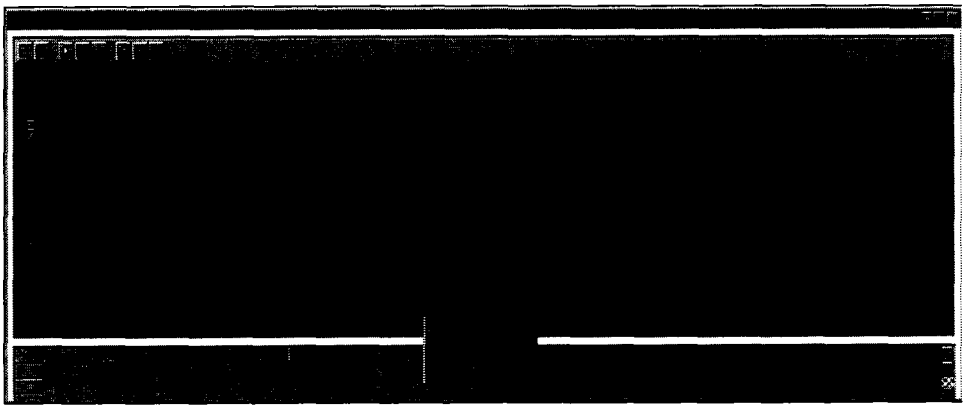

Figure A.6: Monitoring Window

The outlook of the monitoring window can also be changed by selecting options from the popup menu opened by *Right Clicking* on any of the axis or the figure body (figure A.7). The **Edit** option opens a new window (figure A.8) with different options

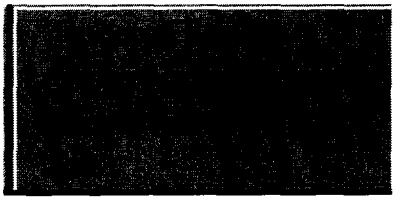

Figure A.7: Monitor Window Popup Menu

for changing the outlooks of the trend lines in the monitoring window.
The table (Figure A.6) on the bottom of the monitor window prints the possible causes of sanding incident if there is any.

A.5 Running the Application

Once the application has been started, it needs to be configured for monitoring sanding. The steps are followings:

Step 1: Connect to Server

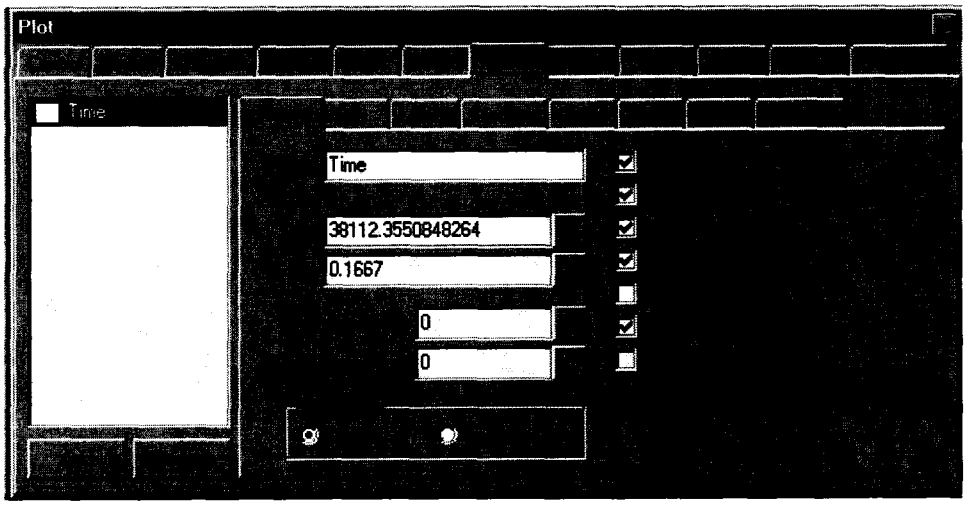

Figure A.8: Monitor Window Options for changing display

Step 2: Select Process

Step 3: Load TAGs and Run

A.5.1 Step 1: Connect to Server

For connecting to Server, go to **Run Menu** ⇒ **Connect to Server**. A new window entitled Connection Wizard appears with Server options and Data Sampling Rate option. Click on **Connect** to connect to the selected server. Close the window to return to the main window. The connection status will be displayed in the status bar of the main window.

A.5.2 Steps 2-3: Monitoring a Process

Starting monitoring a process involves two steps, if there is a blank monitoring window opened already. If a blank monitoring window is not opened, then do so by either of the following steps:

- going to **File Menu** ⇒ **New**
- clicking on the **New Button** in the main window toolbar

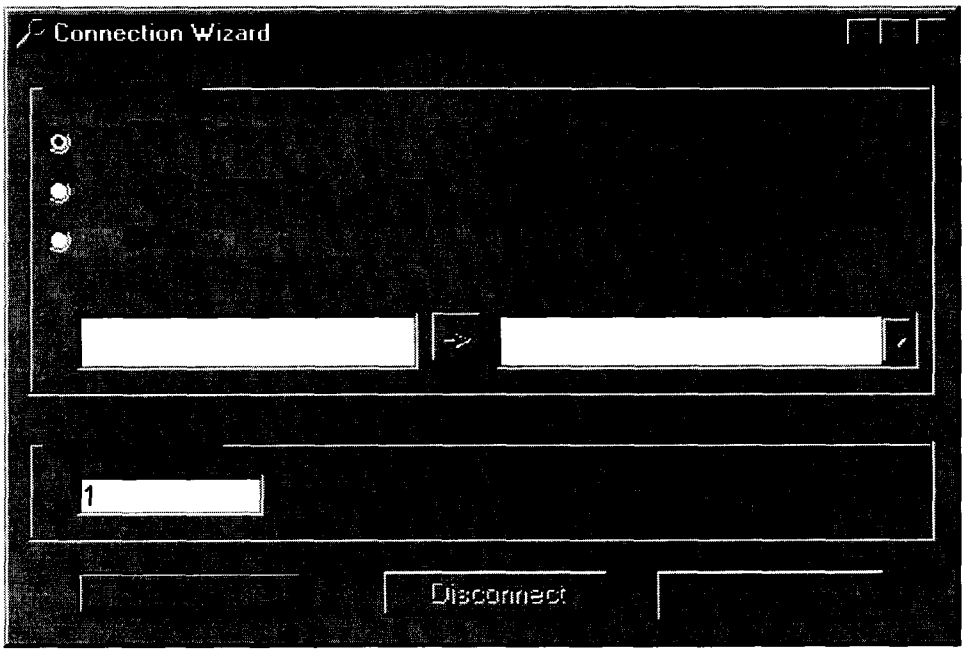

Figure A.9: Connection Wizard

- going to **Window Menu ⇒ New Window**

Once a new blank monitoring window has been opened follow the steps described in sections (A.5.2.1, A.5.2.2) to start monitoring the process.

A.5.2.1 Step 2: Select a Process

For selecting a process for monitoring, go to **Run Menu ⇒ Select Process**. A new window with the names of the available process names appear (figure A.10). Select the process name to be monitored and click **Select Process Button**. The name of the process now appears in the title bar of the sanding monitoring window.

A.5.2.2 Step 3: Load TAGs and Run

With the process been selected for monitoring, the next thing to do is to load the TAGs and then start running the monitoring. For loading the TAGs and starting monitoring the process, go to **Run Menu ⇒ Load TAGs and Run**. A new window opens (figure A.11). Click on **Load TAGs** to load the TAGs for the selected process

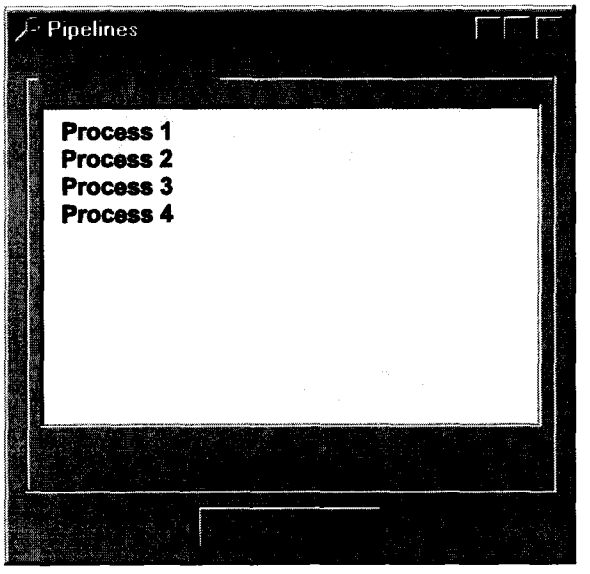

Figure A.10: Process Selection Window

and then click on **Run Process** to start monitoring the process.

A.6 Learning Capability: Updating the Model

This application uses PCA which is data based monitoring *i.e.*, it does not use an explicit model. Rather it uses a historical data matrix obtained from selected key transformed variables and builds an internal implicit model to monitor the process. The algorithm generates two sets of plots based on which it can learn and update the model itself or the user can update the model manually based upon a significant change of process operating condition.

A.6.1 Saving Model Data: Initial and Updating

The model data matrix for each process used by the algorithm is stored in a text file in the directory *Application_Directory/Data/TailingLineName.txt* where the *Application_Directory* is the directory where the application has either been installed or stored (*e.g.*, *D:/PipeMonitor*).

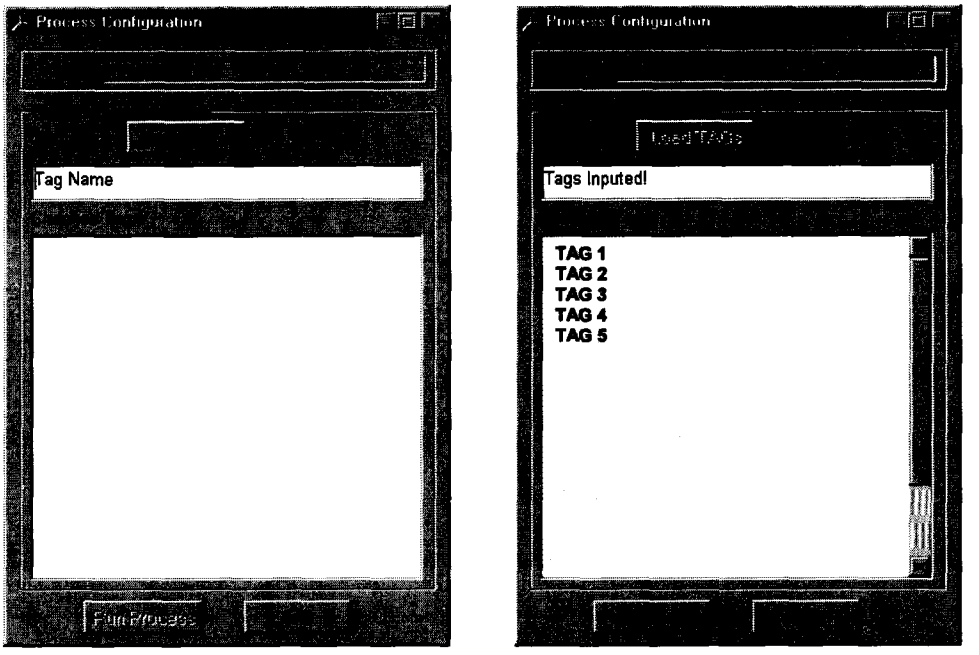

Figure A.11: Window for loading TAGs

A.6.2 How to Update the Model

The model can be updated manually based on the experience or automatically by the application on any current instance. The historical data can also be included in the data matrix and then update the model if needed. The following are the options for starting and stopping updating of the model:

A.6.2.1 Update the Model

Select the process to be updated and then go to **Run Menu ⇒ Update Model** or click on the **Update Button** in the main window toolbar. An input dialog box (figure A.12) appears asking how long (in minutes) the model for the selected process should be updated. The default is 100 (min). Change it to your desired length for updating the process say, 200 (min) and press **OK**. The process monitor window title bar will show that it is updating (*e.g., Process 1 (Updating)*). The process will continue to update for 200 min (*i.e.*, your desired limit). After updating period is over the process monitor window title will come back to normal (*e.g., Process 1*) showing that it is not being updated anymore. However you can stop updating the process

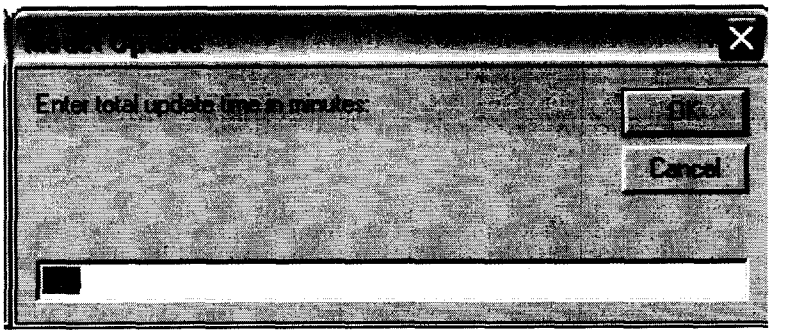

Figure A.12: Updating a process

anytime by going to the **Run Menu** item **Stop Updating** (see section A.6.2.2)

A.6.2.2 Stop Updating:

Select the process which needs to be stopped updating and then go to **Run Menu** ⇒ **Stop Updating** or click on the **Stop Update Button** in the main window toolbar. A confirmation dialog box appears asking whether you really want to stop updating the selected process. Click **Yes** if you want to stop updating the model.

A.6.2.3 Auto Update:

The model can be automatically updated based on the value of T^2. To do so go to **Run Menu** ⇒ **Auto Update** or click on the **Auto Update Button** to toggle between Auto Update on and off state. When Auto Update is checked (✓) or the Auto Update Button in the toolbar is pressed down, the model of a process is updated automatically whenever T^2 exceeds it's 99% Confidence Limit. The title bar of that process changes to show that it is automatically updating (*e.g.*, *Process 1 (Auto Updating)*) during that instant.

A.7 Acknowledgements

Special thanks to Dr. Lisheng Hu and Dr. Xin Huang for building the framework for the software development, and Dr. Bo Li for his continued help on updating the

functionality of the application.